

NUCLEAR SPIN SPECIES CONVERSION  
IN THE SOLID METHANES

NEUTRON SCATTERING AND NUCLEAR SPIN  
SPECIES CONVERSION IN THE SOLID METHANES

By

KENNETH JAMES LUSHINGTON, B.Sc., M.Sc.

A Thesis

Submitted to the School of Graduate Studies  
in Partial Fulfilment of the Requirements

for the Degree  
Doctor of Philosophy

McMaster University

(September) 1977

DOCTOR OF PHILOSOPHY (1977)  
(Chemistry)

McMASTER UNIVERSITY  
Hamilton, Ontario

TITLE: NEUTRON SCATTERING AND NUCLEAR SPIN SPECIES  
CONVERSION IN THE SOLID METHANES.

AUTHOR: Kenneth James Lushington, B.Sc. (U. of Victoria)  
M.Sc. (U. of Victoria)

SUPERVISOR: Professor J. A. Morrison

NUMBER OF PAGES: xii, 160

## ABSTRACT

An understanding of the interconversion between the nuclear spin symmetry species in the solid methanes is essential for characterising the unusual low temperature behaviour of these solids. In this thesis, the measurement of the total neutron scattering cross-sections of the methanes is used to study quantitatively the extent and kinetics of the spin conversion process.

A method of accurately measuring total cross-sections of molecular solids, at low temperatures ( $0.75 \text{ K} < T < 100 \text{ K}$ ) and at long neutron wavelengths ( $4.7 \text{ \AA}$ ), has been developed by modifying an existing neutron spectrometer at the McMaster Nuclear Reactor. The precision and probable accuracy of the method prove to have advantages over some other techniques for following spin species conversion.

Three of the solid isotopic methanes were studied ( $\text{CH}_4$ ,  $\text{CH}_3\text{D}$  and  $\text{CH}_2\text{D}_2$ ). In  $\text{CH}_4$ , extensive measurements were made on solid in phase II, in which spin conversion occurs at different rates on the two different kinds of sublattice. The conversion lifetime of the molecules on the ordered sublattice sites was found to be 75 hours. On the disordered sublattices, the lifetimes were much shorter and strongly temperature dependent. The equilibrium cross-section data

were used to critically test a theoretical description of solid  $\text{CH}_4$ . It was found to be satisfactory.

Spin conversion in  $\text{CH}_3\text{D}$  was studied quantitatively and found to occur primarily below  $T = 4$  K. In contrast to  $\text{CH}_4$ , the spin conversion process in  $\text{CH}_3\text{D}$  was very fast. The cross-section data were also used to guide the analysis of some existing thermodynamic data for  $\text{CH}_3\text{D}$ , and to derive the characteristics of the low-lying tunnelling levels. Some inferences about the nature of the lowest temperature phase (phase III) are made.

Little is known about  $\text{CH}_2\text{D}_2$ , and the cross-section measurements were made to determine if spin conversion occurs, especially below  $T = 4$  K. A change in cross-section was found in this temperature region and an argument is presented which could ascribe such a change to spin conversion.

## ACKNOWLEDGEMENTS

I wish to thank Professor J. A. Morrison for suggesting this problem, for allowing me the freedom to develop the topic and for his continued helpful advice and criticism during the course of this research. I especially wish to thank him for allowing me to benefit greatly from his insight and experience in physical chemistry.

During this research, discussions with Professor R. F. Code, J. Higinbotham, A. Hüller, W. Press and A. J. Nijman have been of great help. In addition, I would like to thank Professor T. Yamamoto for sending a preprint of his immensely useful paper. The friendship and advice of my colleagues at McMaster, especially Marc Leger, Troy Lassau, and Mary Anne Millar, are deeply appreciated. I am also very grateful to J. D. Couper who contributed a great deal of common sense and ingenuity in the modification of the neutron spectrometer.

The patience, encouragement and support of my wife, Dolly, has made the work much easier.

I would like to thank Murlis Pope for her rapid, accurate typing of this thesis, and for having to cope with my handwriting.

Finally, I wish to acknowledge the financial support of the National Research Council of Canada. Acknowledgement is made to the Donors of the Petroleum Research Fund, administered by the American Chemical Society, ~~for partial~~ support of this research.

## TABLE OF CONTENTS

		<u>Page</u>
CHAPTER I.	Introduction	1
CHAPTER II	The Methane "Problem"	8
II.1	Historical Introduction	8
II.2	The Nature of the Solid Phases	11
II.3	Nuclear Spin Species Conversion	26
CHAPTER III	Neutron Scattering - A Nuclear Spin Probe	38
III.1	Introduction	38
III.2	General Theory	38
III.3	Scattering from Hydrogenous Molecules	44
III.4	Neutron Scattering from Molecular Spin States.	46
CHAPTER IV	Experimental	51
IV.1	Sample Preparation	51
1.1	Handling and Storage	51
1.2	The Samples	52
IV.2	Cryogenics	54
2.1	Production and Maintenance of Low Temperatures	54
2.2	The Sample Cell	61
2.3	Measurement and Control of Temperature	63



		<u>Page</u>
IV.3	The Neutron Scattering Experiment	67
	3.1 The Neutron Spectrometer	67
	3.2 Operating Conditions and Calibration	74
	3.3 The Experimental Configuration and Counting Methods	75
CHAPTER V	Results	78
V.1	The Samples	78
V.2	Calculation of Neutron Total Cross- sections	79
V.3	Error Analysis	84
V.4	CH <sub>4</sub>	87
V.5	CH <sub>3</sub> D	95
V.6	CH <sub>2</sub> D <sub>2</sub>	97
CHAPTER VI	Discussion	102
VI.1	Crystal Form and Impurity Content	103
VI.2	Phase I	104
VI.3	CH <sub>4</sub>	108
	3.1 Confirmation of Code and Higinbotham's deductions	108
	3.2 The Direct Proportionality between $\sigma$ and $\langle I(I+1) \rangle$ - A Test of the Theory	109
	3.3 Spin Conversion on the Disordered Sublattices of Phase II	113

	<u>Page</u>
3.4 Anomalous Cross-section Results near the Phase I to II Transition	116
3.5 Kinetics of Conversion	118
VI.4 CH <sub>3</sub> D	125
4.1 The Cross-section and Spin Conversion	126
4.2 Kinetics of Spin Conversion	128
4.3 The Entropy of CH <sub>3</sub> D	131
4.4 A Model for Phase III of CH <sub>3</sub> D	133
VI.5 CH <sub>2</sub> D <sub>2</sub>	139
CHAPTER VII Conclusions	142
APPENDIX 1	145
APPENDIX 2	148
BIBLIOGRAPHY	151

## LIST OF FIGURES

<u>Figure</u>		<u>Page</u>
1.	The P-T phase diagram for solid CH <sub>4</sub> and CD <sub>4</sub>	10
2.	The isotopic interatomic potential	13
3.	The phase II structure of the methanes	18
4.	The energy level scheme for phase II of CH <sub>4</sub>	22
5.	The temperature dependence of $\langle I(I+1) \rangle$	32
6.	The low temperature entropy of CH <sub>3</sub> D	36
7.	The total cross-section of ortho- and para-hydrogen	49
8.	The cryostat	55
9.	The helium-3 refrigerator	60
10.	The sample cell	62
11.	The resistance temperature curve for the carbon thermometer	65
12.	The neutron wavelength distribution from a thermal neutron reactor.	68
13.	Twin-axis spectrometer	70
14.	Cross-sectional view of the neutron beam	72
15.	The molar volumes of the methanes	81
16.	The total cross-section of CH <sub>4</sub>	89
17.	The low temperature total cross-section of CH <sub>4</sub>	91

<u>Figure</u>		<u>Page</u>
18.	The total neutron cross-section of $\text{CH}_3\text{D}$	96
19.	The low temperature total neutron cross-section of $\text{CH}_3\text{D}$	98
20.	The total neutron cross-section of $\text{CH}_2\text{D}_2$	100
21.	The low temperature total neutron cross-section of $\text{CH}_2\text{D}_2$	101
22.	The cross-section per proton, for the three methanes studied, in phase I	105
23.	The anomalous cross-section results in $\text{CH}_4$	117
24.	The conversion lifetimes in $\text{CH}_4$	121
25.	A truncated portion of the disordered sublattice energy level scheme in $\text{CH}_4$	123
26.	The population of the degenerate A-T level plotted with the conversion lifetimes in $\text{CH}_4$	124
27.	Thermal relaxation data in $\text{CH}_3\text{D}$	129
28.	The entropy of $\text{CH}_3\text{D}$ below $T = 4$ K	132
29.	An hypothetical energy level scheme and the corresponding values of $\langle I(I+1) \rangle$ for $\text{CH}_2\text{D}_2$	140

LIST OF TABLES

<u>Table</u>		<u>Page</u>
I	Transition Temperatures in the Methanes	9
II	Spin Species in the Methanes	27
III	Isotopic Composition of the Deuterated Methane Samples	54
IV	Thermocouples	66
V	Conversion kinetics in ${}^1\text{CH}_4$ - oxygen-doped	93
VI	Conversion kinetics in $\text{CH}_4$ - pure sample	94
VII	Conversion kinetics in $\text{CH}_3\text{D}$	99
VIII	Comparison of observed equilibrium neutron cross-sections with cross-sections calculated from theory	112
IX	Conversion on the disordered sublattices of $\text{CH}_4$	114
X	The energy level scheme derived from the equivalent molecule model	135
XI	Comparison between observed and calculated cross-sections in $\text{CH}_3\text{D}$	137
Al.I	Krieger-Nelkin parameters	147
Al.II	Calculated cross-sections	147

CHAPTER I  
INTRODUCTION

The terms quantum solid, quantum fluid and quantum behaviour have come primarily from the low temperature investigation of a few solids and liquids. They are, in many respects, reflections of a historical development; if the attempt to understand a system in terms of classical ideas failed, either totally or in part, the aberrations were ascribed to quantum effects. In this context, quantum solids are solids for which few aspects of their behaviour can be fully understood in terms of the classical precepts.

The label "quantum solid" is one of convenience because all solids are indeed quantum solids. It is only the limits of our perception, the range of current experimental technology and thought, that create the division between quantum and classical solids. The division is at best indistinct, and can at times be misleading.

Solid hydrogen is a prime example of a quantum solid. It is a molecular crystal where the quantum restrictions on the occupation of distinct quantum states completely dominate its behaviour. The intermolecular interactions in a crystal of solid hydrogen can be conveniently broken into two components: a weak isotropic dispersion force, which

provides most of the lattice binding energy, and an orientationally dependent quadrupole-quadrupole electrostatic force which, although weak, is intimately associated with the bulk of the low temperature properties of solid hydrogen. These intermolecular interactions are, however, so weak, and the rotational energy level spacings so large, due to the very low moment of inertia, that, even in the solid, the energy states of the molecules are little different from the free molecule in the gas<sup>1</sup> and  $J$  remains a good quantum number.

In hydrogen, the Pauli Principle affirms that the total wave function must be antisymmetric with respect to proton exchange. This has a profound effect. If the usual separation of the wave function into a product wave function is attempted, it is readily seen that the electronic, vibrational and translational portions are all symmetric at low temperatures, implying that the rotational-nuclear spin wave function must at all times be antisymmetric. The antisymmetric restriction couples specific rotational and nuclear spin states, which results in states with  $J$  odd being associated with a total nuclear spin,  $I$ , of unity, while states with  $J$  even have a total nuclear spin of zero. The two distinct combinations are referred to as ortho- and para-hydrogen respectively.

Proton exchange in hydrogen is equivalent to the parity operation and, as a consequence, no intramolecular interactions can mix the ortho and para states to allow

interconversion - a factor which gives ortho- and para-hydrogen all the characteristics of distinct chemical species. In the solid at low temperatures, the large rotational energy spacings are such that the ortho-hydrogen is almost entirely in the  $J=1$  level, and the para-hydrogen, in the  $J=0$  level.

Conversion between the two species in the solid state is possible because intermolecular nuclear spin dipole-dipole interactions mix the ortho and para states. The conversion process is, however, very slow<sup>2</sup>. Acceleration of the conversion process can be accomplished by catalysts which either absorb the hydrogen atomically or place the hydrogen in a large magnetic field gradient<sup>3</sup>. It is possible experimentally to prepare hydrogen samples with any arbitrary ortho-para concentration<sup>4</sup>.

Solid hydrogen and the complementary solid deuterium have been intensely studied, both experimentally and theoretically. Many of the unusual properties at low temperature originate from the orientational interaction between the molecules<sup>5</sup>. Para-hydrogen in the  $J=0$  state is essentially spherical, and the orientational part of the potential does not affect these molecules<sup>6</sup>. Pure para-hydrogen and mixtures containing less than 63 per cent ortho-hydrogen crystallize in a h.c.p. lattice which is stable down to the very low temperatures, but if the orthohydrogen concentration is greater than 63 per cent, the solid undergoes a phase transition to a f.c.c. structure at lower temperatures. The



phase transition is associated with the orientational ordering of the ortho molecules. In the high temperature h.c.p. phase, the three components,  $M_J = -1, 0, +1$ , of the angular momentum in the  $J=1$  level are degenerate, but in the f.c.c. structure, the degeneracy is lifted and excitations from the ground state  $M_J=0$ , to the excited state,  $M_J = \pm 1$ , involve collective angular momentum excitations (librons) along specific crystal axes<sup>7</sup>. Libron excitations, analogous to magnetic spin waves, have been observed experimentally<sup>8,9</sup> and extensively examined theoretically<sup>6,10,11,12</sup>.

Dilute solutions of ortho-hydrogen in para-hydrogen also exhibit an interesting orientational behaviour. At low temperatures, the molecular reorientation occurs by mutual reorientation of pairs of ortho molecules, coupled by the intermolecular quadrupole-quadrupole interaction. The process has been called adiabatic molecular reorientation because no phonons are required to aid the reorientation<sup>13</sup>. The a.m.p. process causes the molecular reorientation time,  $\tau_c$ , to be temperature independent, and a sensitive function of the ortho hydrogen concentration. This system of a pair of ortho molecules imbedded in an essentially inert matrix of para molecules has provided a unique opportunity to examine the quadrupole-quadrupole interaction potential between two ortho-hydrogens<sup>14,15</sup>.

The solid methane system has many similarities to solid hydrogen, the major one being that, in all five of the

isotopic modifications of methane formed by selective deuteration of  $\text{CH}_4$ , the Pauli Principle must be obeyed and each isotopic modification has two or more nuclear spin symmetry\* species. Moreover, the moments of inertia are low, and quantum effects are observable at easily accessible low temperatures. Solid methane has, however, some additional complications not present for solid hydrogen.

The methanes form molecular crystals with the isotropic dispersion forces providing the bulk of the lattice binding energy and, as in hydrogen, the electrostatic forces provide the orientational part of the potential. The dominant electrostatic term for the methanes is, however, the octupole-octupole interaction. In the methanes, the intermolecular interactions are of comparable energy to the energy separation of the free rotor levels, and  $J$  is no longer a good quantum number<sup>18</sup>. The moments of inertia of  $\text{CH}_4$  through  $\text{CD}_4$  are such that the low temperature properties of  $\text{CH}_4$  are characteristic of a quantum crystal, while the majority of the properties of  $\text{CD}_4$  can be described classically. Hence the methane system bridges the region between quantum and classical solids.

Conversion between the spin species is also more complex in the methanes. Intramolecular as well as intermolecular interactions can mix the various spin states, thus

---

\* abbreviated to spin species in all of the following text.

allowing conversion to occur through different pathways. The role of the spin species and conversion between them, especially for the partially deuterated methanes, is a problem of great importance if the methane system is ever to be understood as well as is hydrogen. The lack of experimental information is so extreme that, for the partially deuterated methanes, it has not been clear if spin species conversion even occurs and, if it does, on what time scale. Even for  $\text{CH}_4$ , the most extensively studied methane, the mechanism and extent of the conversion process has not been well defined until very recently<sup>17,18</sup>.

An experiment which could accurately detect spin conversion or, better still, an experiment which could quantitatively reveal the extent of spin conversion in the methane system would be of great value in unravelling the complexities of the methane 'problem'. In this thesis, the incoherent neutron total scattering cross-section for protons is used to study spin conversion in three of the isotopic methanes, -  $\text{CH}_4$ ,  $\text{CH}_3\text{D}$  and  $\text{CH}_2\text{D}_2$ . Not only is spin conversion detected, but quantitative measurements of its extent and kinetics have been made. The results show that, for  $\text{CH}_4$ , spin conversion is rapid if an oxygen catalyst is present, and that almost complete conversion to the ground state A spin species is achieved by  $T = 0.75 \text{ K}$ . For a pure  $\text{CH}_4$  sample, spin conversion is much slower, and distinct differences in conversion rates on the two sublattices,

of which the solid is composed, ordered and disordered, are found. Conversion in  $\text{CH}_3\text{D}$  is, however, found to be rapid, both for the pure and oxygen-doped samples, and to occur at lower temperatures than for  $\text{CH}_4$ . The analysis of the conversion in  $\text{CH}_3\text{D}$  has allowed a more complete interpretation of existing heat capacity and entropy data to be made, and some inferences about the structure of the lowest stable orientationally ordered phase are made. Possible spin conversion in  $\text{CH}_2\text{D}_2$  is also found, but the effect on the cross-section is small and, in the absence of additional data from other methods, no extensive deductions can be made.

## CHAPTER II

### THE METHANE "PROBLEM"

#### II.1 Historical Introduction

An interest in the Third Law of Thermodynamics led to the first investigation of solid methane. In 1929, Klaus Clusius, as part of his laboratory's extensive examination of molecular solids, measured the heat capacity of  $\text{CH}_4$ <sup>19</sup>. A  $\lambda$ -type anomaly was found at  $T = 20.4$  K which indicated that methane existed in two solid phases (now normally labelled I and II, in order of decreasing temperature). In the following years, the other isotopic modifications were prepared and their heat capacities measured<sup>20,21,22,23</sup>. The deuterated methanes were found to have three solid phases, with the new low temperature phase designated as III. The "missing" phase of  $\text{CH}_4$  was therefore, a mystery, and extensive work was performed to try to resolve it. The transition temperatures for the various methanes are given in Table I.

An analysis of the entropy of  $\text{CH}_4$  based on an extrapolation of the heat capacity data from about  $T = 15$  K<sup>20,21</sup> indicated no residual entropy at  $T = 0$  K, from which it was deduced that a third phase probably did not occur. Heat capacity measurements on mixtures of  $\text{CD}_4$  and  $\text{CH}_4$ <sup>23</sup> showed that a wide range of concentrations did exhibit all three

TABLE I

Transition Temperatures (K)

	I → II	II → III
CH <sub>4</sub>	20.4	-
CH <sub>3</sub> D	23.1	16.1
CH <sub>2</sub> D <sub>2</sub>	24.9	19.1
CD <sub>3</sub> H	26.0	20.9
CD <sub>4</sub>	27.2	22.4

phases and, only as the mixture approached pure CH<sub>4</sub>, did the third phase disappear. In 1938, an additional piece of the puzzle was provided by a high pressure investigation (1 kbar to 2 kbar) of solid CH<sub>4</sub><sup>24</sup>, which showed that CH<sub>4</sub> did transform to phase III at higher pressures. Following this early work on the methanes motivated by the Third Law studies, the focus of interest shifted by the 1950's to the nature of the three solid phases, and the reasons behind the polymorphic behaviour of the methanes.

More complete high pressure studies of solid CH<sub>4</sub> were completed<sup>25,26</sup> which confirmed the existence of phase III at pressures as low as 1 kbar, but at still lower pressures, the phase did not appear to be stable. Similar measurements were also made on CD<sub>4</sub><sup>26</sup>, where all three phases were stable down to zero pressure. The phase diagrams for CH<sub>4</sub> and CD<sub>4</sub> were qualitatively similar and are shown in Figure 1., where the course of the II to III transition

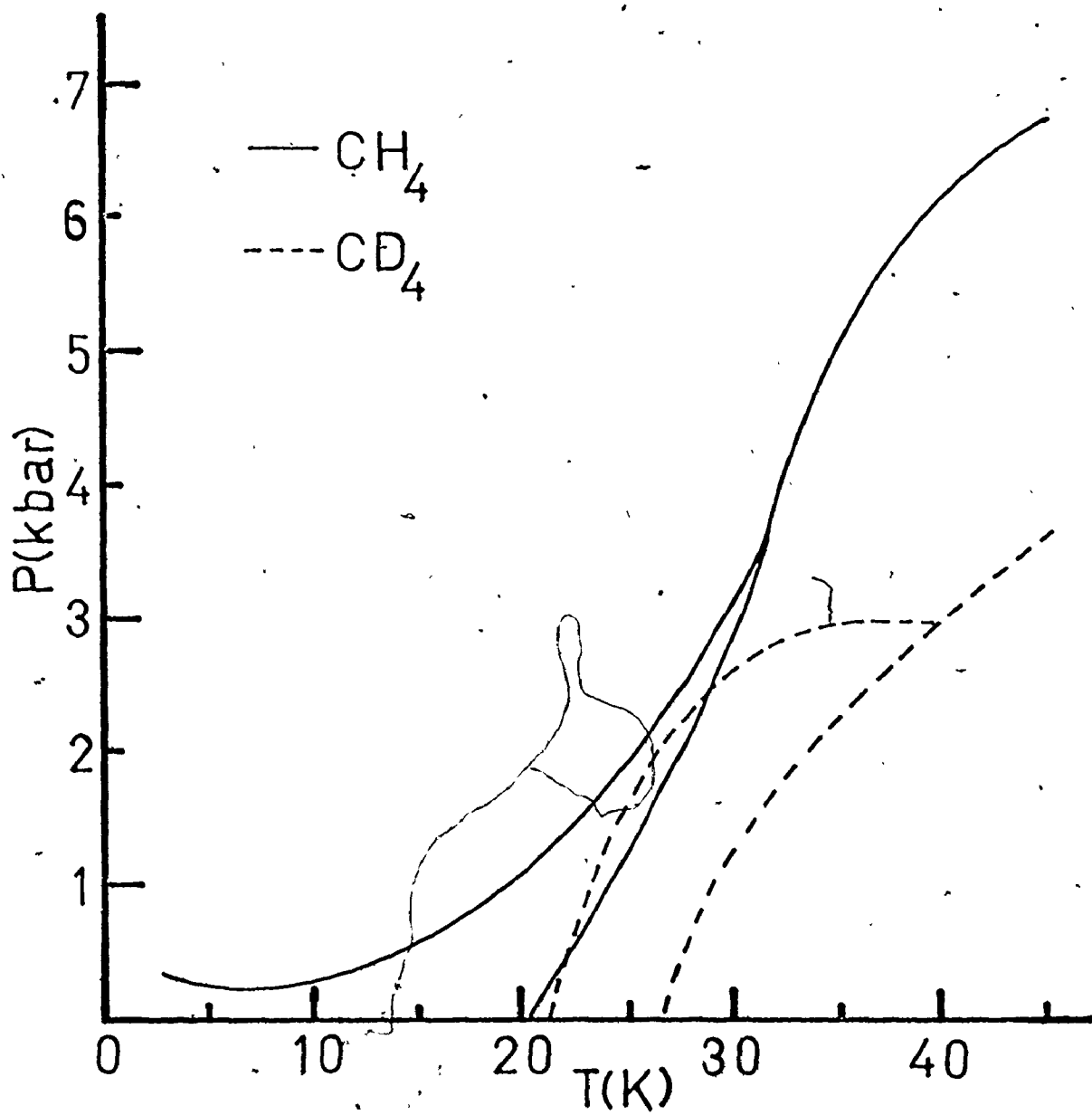


Figure 1. The P-T phase diagram for solid  $\text{CH}_4$  and  $\text{CD}_4$

line in  $\text{CH}_4$  at low pressures has been determined by recent n.m.r. measurements<sup>27</sup>.

Early X-ray diffraction studies on  $\text{CH}_4$  showed that both solid phases had an f.c.c. structure<sup>28</sup>. More recent X-ray studies have confirmed the f.c.c. structure<sup>29,30,31,32</sup>. Heavy methane ( $\text{CD}_4$ ) was later studied by both X-ray<sup>33</sup> and neutron diffraction<sup>34,35</sup> techniques which showed that the two upper phases also had an f.c.c. structure, while phase III appeared to have undergone a slight tetragonal distortion. The  $\lambda$ -type anomalies seen in the heat capacities, the entropies of fusion and the two transition regions, and the retention of the f.c.c. structure, or something very close to f.c.c., all suggested that the three solid phases were associated with increasing orientational ordering as the temperature decreased. On this basis, the transformations from one polymorph to another indicated abrupt changes in the orientational order of the molecules.

## II.2 The Nature of the Solid Phases

Solid methane is a member of a much larger class of solids, molecular solids. As the name suggests, the most distinct feature of these solids is that the molecules retain their identity within the solid. The molecules are also electrostatically neutral, and the intermolecular bonding is very weak compared to the chemical bonds within the molecular framework.



The origins of the intermolecular potential are complex because contributions can come from many sources<sup>36,37</sup>. The rare gas solids are the simplest "molecular" solids. The intermolecular potential is isotropic, and has both a short range repulsive interaction and a long range attractive interaction. The short range repulsive interaction is due to exchange forces as the atomic wave functions overlap. The long range, attractive interaction is due to dispersion and induction forces. The resulting potential has the general form shown in Figure 2, and has been extensively modeled by simple functions, such as the Lennard-Jones 6-12 potential, or by more sophisticated forms<sup>38</sup>.

The repulsive exchange and the attractive dispersion forces are also the major contributors to the more complex interactions between molecules. In most molecular solids, the dispersion terms account for most of the crystal binding energy, but an additional interaction is possible; the electrostatic permanent multipole interaction which is not present in atomic solids. Molecules may possess permanent electric moments which can interact to give either an attractive or a repulsive contribution to the intermolecular potential.

The high symmetry of the methane molecule causes the dispersion interaction between two methane molecules to be isotropic with respect to the relative molecular orientations. Thus, in solid methane, the dispersion forces will be the

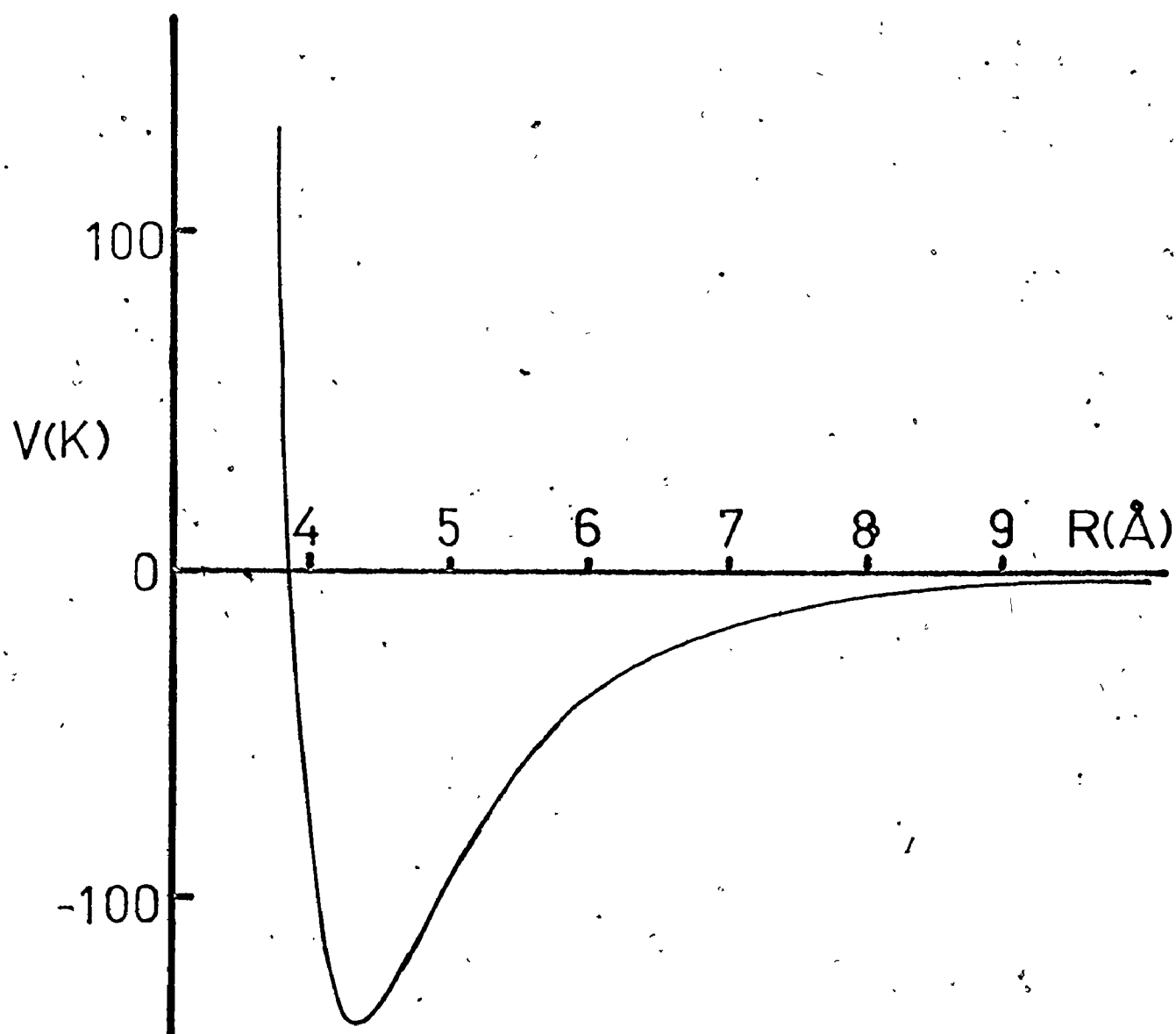


Figure 2. The isotropic interatomic potential

determining factor for the magnitude of the lattice parameter and the stable f.c.c. structure, but it is the electrostatic forces which influence the molecular orientations. For methane, the first non-zero permanent electric moment is the octupolar one, and the orientationally-dependent electrostatic interaction is correspondingly weak.

The fundamental differences between the relatively strong, isotropic dispersion forces and the weak, orientationally-dependent octupole-octupole interaction in methane were the basis for the first, highly successful attempt to describe theoretically the nature of the polymorphism in solid methane, - the now classic James and Keenan model<sup>39</sup>. Solid methane was modeled by placing spherical rotors with tetrahedral point charge distributions on an f.c.c. lattice. The model was kept as simple as possible by neglecting both molecular and lattice vibrations, and by considering only the electrostatic octupole-octupole interactions between molecules. The octupole moment was treated as the one disposable parameter in the theory. The model was analysed within the framework of classical statistical mechanics, thus neglecting rotational quantisation and the presence of nuclear spin species. It was hoped that the use of the octupole moment as an adjustable parameter would partially compensate for these deficiencies. The classical restrictions of the theory did, however, suggest that the results would best apply to  $CD_4$ , and care would have to be taken in extending them to  $CH_4$  where

quantum effects could seriously interfere.

A classical Hamiltonian,  $H$ , was constructed from two terms; the rotational kinetic energy,  $T_i$ , and the orientationally dependent pair interaction potential,  $V_{ij}$ .

$$H = \sum_i T_i + \sum_{i>j} V_{ij}(\omega_i, \omega_j) \quad [1]$$

The orientations of the molecules were specified by their Euler angles,  $\omega_i$ . If the Helmholtz free energy of the system was minimised, statistical mechanics provided the means to define a system distribution function in phase space,  $\Phi(p, q)$ , which was separable into kinetic and potential energy terms

$$\begin{aligned} \Phi(p, q) &= \exp(-H/kT) / \int dt \exp(-H/kT) \quad [2] \\ &= \prod_i f_i(\omega_i) \exp(-T_i/kT) / \int d^3p \exp(-T_i/kT). \end{aligned}$$

The orientational portion of [2],  $f_i(\omega_i)$ , was the independent probability distribution function for the  $i^{\text{th}}$  molecule within the mean field approximation,

$$f_i(\omega_i) = \exp(-V_i(\omega_i)/kT) / \int d^3q \exp(-V_i(\omega_i)/kT), \quad [3]$$

where

$$V_i(\omega_i) = \sum_{\substack{\text{nearest} \\ \text{neighbours}}} \int d\omega_j V_{ij}(\omega_i, \omega_j) f_j(\omega_j). \quad [4]$$

Equations [3] and [4] comprised a set of consistency equations which were solved iteratively to obtain a self-consistent

set of independent distribution functions,  $f_i(\omega_i)$ . Each possible self-consistent set was associated with a possible phase of the system and, once found, allowed the internal energy, entropy and free energy to be calculated easily. James and Keenan solved these equations with the explicit form of the octupole-octupole interaction and searched for solutions at various temperatures. The disordered solution, where

$$f_i(\omega_i) = 1/8\Omega^3 \quad [5]$$

for all molecules in the system, was always found to be a solution at any temperature. At lower temperatures, two additional solutions of lower free energy were discovered. The octupole moment was then adjusted to move the phase transition between the disordered to first ordered solution to correspond to the observed transition temperature in  $CD_4$ .

The James and Keenan model successfully predicted three solid, orientationally different, phases and managed to reproduce the lower transition temperature (II  $\rightarrow$  III) quite well once the upper transition temperature had been fixed. The orders of the phase transitions, within the framework of the model, were also determined. The upper transition was found to be second order, and the lower one first order. The most interesting aspect of the solutions was, however, the structures of the three phases. The high temperature phase (I) was orientationally disordered with all molecules equivalent. The structure for phase II was

more unusual. The crystal had eight distinct sublattices and, on six of them, the molecules were constrained to librational motion with the orientations arranged in an "antiferromagnetic" fashion. On the remaining two sublattices, the molecules were essentially free rotors. This rather bizarre structure, shown in figure 3, occurred because the ordered molecules, on what are now known as the antiferro-rotational sublattices, form a cage about the central disordered molecules. The symmetry of the cage cancels the electrostatic field exactly, thus allowing the molecule to rotate freely. This structure, while derived for  $CD_4$ , should be the same for phase II of  $CH_4$  because the heat capacities of mixtures of  $CH_4$  and  $CD_4$  showed that the I to II transition existed at all concentrations of the two components<sup>23</sup>. The lowest temperature phase (III) was deduced to be of uniform order, called ferrorotational, with all the molecules having identical orientations and constrained to librational movement. James and Keenan also suggested that a tetragonal distortion, a compression along the z-axis, should occur for this ordered phase.

The distinctive structure predicted for phase II was not widely accepted in the discussion of the properties of solid methane until a neutron diffraction study of  $CD_4$ , made thirteen years after the work of James and Keenan, confirmed both the high temperature disordered structure and the complex sublattice structure of phase II<sup>34</sup>. The neutron

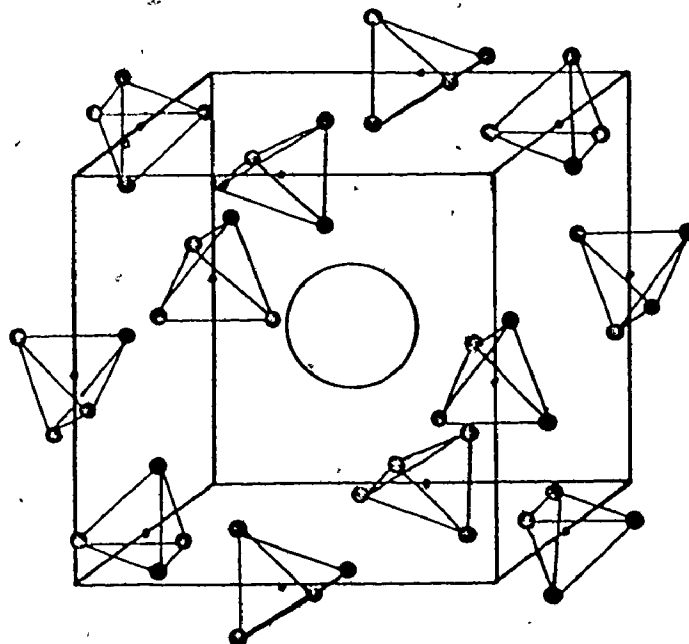


Figure 3. The phase II structure of the methanes, where the tetrahedra represent the ordered molecules and the sphere, the disordered.

diffraction data were not, however, consistent with the proposed structure for phase III. Unfortunately, the refinement of the diffraction data proved difficult, and while James and Keenan's structure could be rejected, no unique space group for the phase III structure could be found<sup>35</sup>. Neutron and X-ray diffraction data<sup>33,35</sup> and optical birefringence studies<sup>40</sup> show, however, that the II to III transition is first order, accompanied by a tetragonal distortion of the lattice.

The classical James and Keenan model, while highly successful, could not give any information on isotope effects, the energy levels for the various structures, nor could it deal with the effects of nuclear spin species. A quantum mechanical extension of the classical model was made by Yamamoto et al, in a series of papers in which the objective was to see if the behaviour of CH<sub>4</sub> could be explained by such a model. This long and detailed theoretical effort culminated in a paper in which many of the observable properties of solid CH<sub>4</sub> were calculated<sup>16</sup>. The extended James and Keenan (EJK) model made the fundamental, but reasonable, assumption that the phase II structure did indeed apply to CH<sub>4</sub>.

To describe adequately the behaviour of solid CH<sub>4</sub>, the EJK calculations had to employ a more comprehensive potential which included a one-body, orientationally dependent crystal field term ( $V_i$ ), similar to the potential experienced by a methane molecule in a rare gas matrix<sup>41</sup>, as well as the two-body orientational molecular field ( $W_{ij}$ ).



The two portions of the potential were expanded, using a multipolar expansion, and then approximated by non-bonded atom-atom potentials. The general form of the Hamiltonian was

$$H = \sum_i \hat{T}_i + f_c \sum_i \hat{V}_i(\omega_i) + f_w \sum_{i>j} \hat{W}_{ij}(\omega_i, \omega_j), \quad [6]$$

which contains two disposable parameters,  $f_c$  and  $f_w$ . These two parameters allowed the relative strengths of the crystal and molecular fields to be adjusted. The fully expanded potential,  $W_{ij}$ , contained terms of the form of the octupole-octupole interaction, as well as higher order terms. By analogy with the classical calculation, a set of consistency equations was established within the mean field approximation and then solved to find the stable structures at various temperatures. The methane wave functions used in the calculations were constructed from a large basis set of symmetry adapted, spherical top, free rotor functions, up to  $J = 8$ , from which the correct symmetry-allowed combinations of the rotational and nuclear spin wave functions were made. The resulting wave functions kept track of the nuclear spin species throughout the calculations. In all the calculations, the various spin species were assumed to be in thermal equilibrium, and randomly distributed among the lattice sites. The disordered high temperature phase, where the molecules have a site symmetry  $O_h$ , and the eight sublattice antiferrorotational phase II, where the ordered molecules

have a site symmetry  $D_{2d}$ , and the disordered,  $O_h$ , were confirmed as the stable structures. Once the structures were firmly established, the potentials for the molecules with different site symmetries were evaluated, often drastically simplified from the full potential, and the site Hamiltonians were defined with the new symmetry-reduced potentials. The site Hamiltonians were then used to evaluate the energy eigenvalues of the molecules on the various sites. The basis set was sufficiently large to permit accurate eigenvalues to be calculated.

The two disposable parameters,  $f_c$  and  $f_w$ , were fixed by calibration with experimental results. The molecular field was found by symmetry to be zero for all molecules in phase I, and for the equivalent disordered molecules in phase II, thus leaving only the crystal field terms in the potential. The crystal field parameter,  $f_c$ , was adjusted to give an energy spacing between the two lowest energy levels, for a disordered molecule, comparable to the spacing obtained from neutron inelastic scattering data<sup>42</sup>. The molecular field parameter,  $f_w$ , was then set to duplicate the correct transition temperature between phase I and II. Once these parameters were fixed, the energy eigenvalues for the molecules on both the  $D_{2d}$  and the  $O_h$  sites were established. The result is shown in Figure 4.

The success of the EJK model applied to  $CH_4$  was assessed in two ways: by its ability to reproduce known

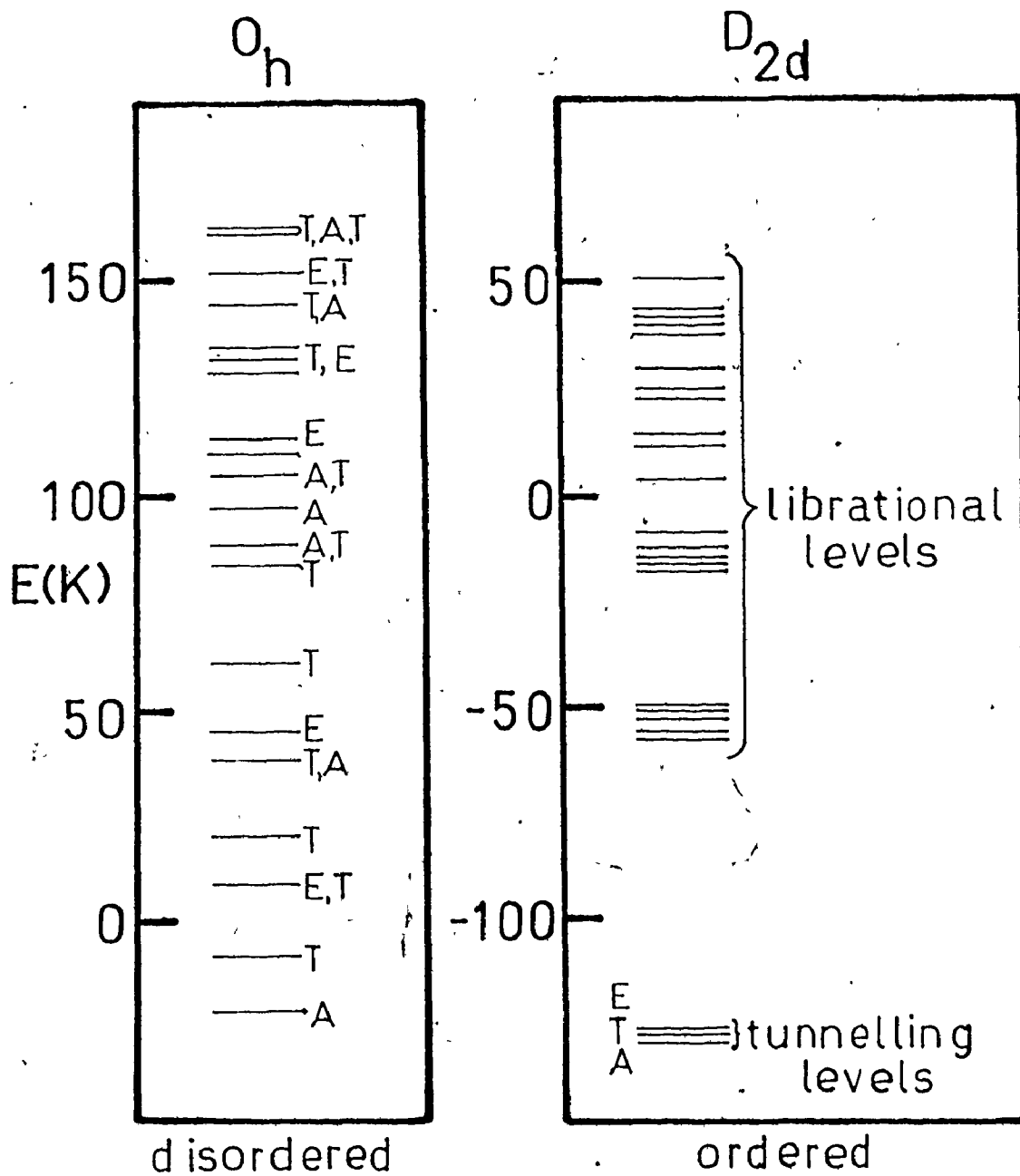


Figure 4. The energy level scheme for phase II of CH<sub>4</sub> from the calculations of Yamamoto et al.<sup>16</sup>

experimental behaviour, and by the aid it rendered in the interpretation of unexpected experimental results. The most stringent test was the comparison of the calculated energy eigenvalues with those determined from neutron inelastic scattering experiments. Early neutron experiments on phase II of  $\text{CH}_4$  had detected excitations that appeared characteristic of a free rotor<sup>43,44</sup> a result which, if not interpreted in terms of the now established structure of phase II, was hard to reconcile with the heat capacities and other data. The theoretical treatment of phase II did, of course, provide the answer. These excitations were associated with the molecules on the two orientationally disordered sublattices. The comparison of the neutron scattering data,<sup>42,43,44</sup> including those used to set the parameter  $f_c$ , with the theoretical eigenvalues for the  $\text{O}_h$  molecules showed excellent agreement. The energy eigenvalues for the ordered  $\text{D}_{2d}$  molecules, first published in a preliminary report by Yamamoto et al.<sup>45</sup>, provided both the means to analyse an ingenious n.m.r. experiment and the incentive for further inelastic neutron studies. The eigenvalues for the  $\text{D}_{2d}$  molecules were shown to be grouped into a low lying set of tunnelling levels and a series of much higher energy groups which corresponded to librational excitations. The excitations within the tunnelling levels were first detected by a paramagnetic impurity n.m.r. level-crossing experiment<sup>46</sup>, but the most conclusive proof of the tunnelling levels' existence came from

a very accurate neutron inelastic scattering experiment which determined both the separation of the energy levels and their symmetry classifications<sup>47</sup>. Again, agreement between theory and experiment was good, although the calculated energy level spacings for the tunnelling levels were slightly larger than those determined from experiment.

An unexpected feature of the calculated energy levels for the ordered molecules was their temperature dependence below about  $T = 4$  K. The increase in level spacing with decreasing temperature resulted from conversion between the nuclear spin species.

The agreement of the theory with some other recent experimental results was also found to be good. Contrary to the classical calculations, the inclusion of the crystal field term resulted in a first order phase transition between phases I and II, in agreement with experimental lattice parameter<sup>32</sup> and heat capacity results<sup>48</sup> which have found discontinuities and hysteresis effects in the transition region. Two further experimental properties of solid methane were readily interpreted in terms of the theoretical model; the low temperature heat capacities and the thermal expansion. Both of these quantities depend, however, on the extent of spin conversion. The heat capacity of  $\text{CH}_4$  has a large Schottky-type anomaly<sup>49</sup>, centred near  $T = 1$  K, which could only be observed if spin conversion was catalysed and thermal equilibrium between the three spin species achieved. The

anomaly associated with the depopulation of the low lying tunnelling levels of the ordered molecules and the calculated heat capacity, including the contribution from the temperature dependence of the levels, gave an adequate fit to the experimental data<sup>16</sup>. Early thermal expansion studies of CH<sub>4</sub> discovered a weak negative thermal expansion below T = 8 K<sup>50</sup>, while more recent work has shown the effect to be much more pronounced<sup>32,51</sup>. The discrepancy between the two groups of data was attributable to different extents of spin species conversion. The earlier work was performed on a sample not in complete thermal equilibrium.

The nature of phase I and II for both CD<sub>4</sub> and CH<sub>4</sub> is now well established, and any subsequent experiments must be interpreted with these structures in mind. The extension of the use of these structures to the intermediate isotopic methanes, CH<sub>3</sub>D, CH<sub>2</sub>D<sub>2</sub> and CD<sub>3</sub>H, is almost certainly valid. The situation with respect to phase III is not quite so unambiguous, but again the methanes, excluding CH<sub>4</sub>, probably have the same low temperature structure. Phase III is undoubtedly more ordered than phase II, but a complex sublattice structure is entirely possible. The energy eigenvalues for the molecules in phase III probably closely resemble those for the ordered molecules in phase II. This is given some support by the appearance of Schottky-type anomalies, similar to that observed in CH<sub>4</sub>, for three of the four deuterated methanes<sup>52,53</sup>. No anomaly has been observed for

CD<sub>4</sub>, but the measurements may not have been extended to low enough temperatures.

### II.3 Nuclear Spin Species Conversion

A group theoretical treatment of the symmetry allowed combinations of the rotational-nuclear spin wavefunctions of CH<sub>4</sub> showed that three spin species existed<sup>54</sup>. For convenience, the species are labelled by the symmetry of the rotational portion of the wavefunction. Similar analyses have also been made for the other isotopic methanes<sup>5</sup>, and a summary is given in Table 2. Also shown in the table are the values of the proton nuclear spin,  $I_H$ , the deuteron nuclear spin,  $I_D$ , which correspond to the various spin species, and the value of the mean squared proton nuclear spin angular momentum,  $\langle I(I+1) \rangle$  at zero temperature and at high temperature limit. Much of the literature prior to 1972 on spin conversion and the orientational behaviour of the solid methanes has been reviewed by Bloom and Morrison<sup>5</sup>.

In the absence of a perturbation which can mix the nuclear spin states, spin species interconversion is strictly forbidden, but, unlike hydrogen, intramolecular interactions such as nuclear spin-spin and spin-rotation terms can lead to mixing, and allow conversion to occur<sup>55</sup>. These intramolecular interactions gain in importance if the energy spacing between two levels is small. Intermolecular interactions can also be important. The nuclear spin-spin interaction between neighbouring molecules can mix the spin states,

TABLE 2

	Spin Species	$\langle I(I+1) \rangle_{T=0}$	$\langle I(I+1) \rangle_{T \rightarrow \infty}$
CH <sub>4</sub>	A, I <sub>H</sub> = 2		
	T, I <sub>H</sub> = 1	6.00	3.00
	E, I <sub>H</sub> = 0		
CH <sub>3</sub> D	A, I <sub>H</sub> = 3/2	3.75	2.25
	E, I <sub>H</sub> = 1/2		
CH <sub>2</sub> D <sub>2</sub>	A, $\left\{ \begin{array}{ll} I_D = 2, 0 & I_H = 1 \\ I_D = 1 & I_H = 0 \end{array} \right\}$	4.57 (deuterons)	4.0
	B, $\left\{ \begin{array}{ll} I_D = 1 & I_H = 1 \\ I_D = 2, 0 & I_H = 0 \end{array} \right\}$	1.71 (protons)	1.5
CHD <sub>3</sub>	A, I <sub>D</sub> = 3, 1, 0	8.18	6.0
	E, I <sub>D</sub> = 2, 1		
CD <sub>4</sub>	A, I <sub>D</sub> = 4, 2, 0		
	T, I <sub>D</sub> = 3, 2, 1, 1	14.	8.0
	E, I <sub>D</sub> = 2, 0		



which is the mechanism for conversion in hydrogen, but perhaps a more important intermolecular interaction is that with a paramagnetic impurity. The magnetic field gradient associated with such an impurity can induce a spin flip, thus allowing conversion<sup>3</sup>. For gas samples, a convenient, and often unintentional paramagnetic impurity, is oxygen. The catalytic effect of oxygen on spin conversion in solid hydrogen has been well demonstrated<sup>2,3</sup>.

Spin conversion in solid  $\text{CH}_4$  has been studied primarily through the use of infrared absorption and n.m.r. techniques. The i.r. absorption method followed the progress of spin conversion through careful monitoring of the intensity of absorption of the rotational fine structure on vibrational bands<sup>56</sup>. The measurements were made on  $\text{CH}_4$  matrix-isolated in argon. Changes in the optical absorption intensities with time were caused by the spin conversion process. Methane in an argon matrix is nearly equivalent to the methane molecules in phase I<sup>16</sup>, or the methane molecules on the disordered sublattices of phase II, where only crystal field terms contribute to the potential. The results of the optical measurements indicated that conversion in pure methane followed first order kinetics and had a lifetime of about 130 minutes. The addition of 0.2 mol per cent oxygen shortened the lifetime to about four minutes. Many n.m.r. measurements have been performed on  $\text{CH}_4$  to examine spin conversion, through the use of the known

dependence of the n.m.r. signal intensity, and hence the sample's magnetic susceptibility on the mean squared nuclear spin angular momentum,  $\langle I(I+1) \rangle$ <sup>57</sup>. The value of  $\langle I(I+1) \rangle$  does, of course, reflect the progress of spin conversion. The first n.m.r. observation of the kinetics of spin conversion in solid  $\text{CH}_4$  was made by Wolf and Whitney<sup>58</sup>, who noted that, after the sample was cooled to  $T = 4.2 \text{ K}$ , the intensity of the n.m.r. signal approached an equilibrium value at a rate best characterised by a lifetime of about 130 minutes. Confirmation of the effect of oxygen on the conversion rate was soon made using a similar n.m.r. technique<sup>59</sup>. This later experiment also indicated that conversion in pure  $\text{CH}_4$  took significantly longer than the time of the experiment (24 hours), while a heavily oxygen-doped sample converted in less than ten minutes. At intermediate oxygen concentrations, the conversion process went to about 60 per cent completion in twenty-four hours. Another careful n.m.r. experiment studied the conversion rate for a large number of samples in which the oxygen concentration was varied from 30 ppm. up to 4.1 mol per cent<sup>60</sup>, and a change in the rate of conversion by a factor of fifty was observed between the lowest and highest oxygen concentration samples.

A careful examination of the results for oxygen-doped samples from the various experiments indicated that, while accurate oxygen-methane gas mixtures could be prepared, there was no guarantee that the composition of the solid was

the same as the initial gas mixture. Thus, many of the differences between different experiments could be ascribed to sample history.

The kinetics experiments were complemented by other n.m.r. experiments designed to follow the extent of conversion at equilibrium. The n.m.r. signal intensity was calibrated so that accurate values of  $\langle I(I+1) \rangle$  could be obtained<sup>57</sup>. At  $T = 4.2$  K, the value of  $\langle I(I+1) \rangle$  was found to be 3.73, considerably above the high temperature limiting value of 3.00. This experiment conclusively proved the existence of spin conversion in solid  $\text{CH}_4$ . There were, however, some apparently conflicting results. A single experiment at  $T = 1.06$  K on an oxygen-doped  $\text{CH}_4$  sample determined  $\langle I(I+1) \rangle$  to be  $5.88 \pm 0.3$ <sup>61</sup>, far above the previous value at  $T = 4.2$  K. In another n.m.r. experiment in which both the equilibrium values of  $\langle I(I+1) \rangle$  and the approach to equilibrium were studied<sup>62</sup>,  $\langle I(I+1) \rangle$  at  $T = 4.2$  K was found to be 4.1, and the value had risen to 4.6 at  $T = 1.6$  K. The kinetics experiments were performed by cooling the samples rapidly from  $T = 19$  K to a series of lower temperatures while the magnetic susceptibility was monitored. The results indicated that the conversion process was temperature dependent, with its rate decreasing at lower temperatures.

The obvious discrepancies between the low temperature values of  $\langle I(I+1) \rangle$  for the different n.m.r. experiments were resolved by a detailed study of a pure  $\text{CH}_4$  sample<sup>17</sup>,

which showed that  $\langle I(I+1) \rangle$  approached a limit of 3.75 if the time of the experiment was only a few hours. It was suggested<sup>17</sup> that this limit corresponded to complete conversion on only the disordered sublattices in phase II of solid  $\text{CH}_4$ . Moreover, it was argued that higher values of  $\langle I(I+1) \rangle$  must include conversion on the ordered as well as the disordered sublattices, and that oxygen catalysis was probably involved. The behaviour of  $\langle I(I+1) \rangle$  as a function of temperature, for the two proposed mechanisms, is shown in Figure 5.

Neutron scattering can also be used to monitor changes in  $\langle I(I+1) \rangle$ . A neutron total cross-section experiment on pure  $\text{CH}_4$  was performed<sup>63</sup> to see if spin conversion was detectable by this method. A small apparent increase in  $\langle I(I+1) \rangle$  was found at  $T = 4.2$  K, but the size of the effect was much smaller than that expected from the n.m.r. data. It is also probable that the sample was not at equilibrium during these experiments.

The large amount of data on spin conversion in  $\text{CH}_4$ , which once appeared bewilderingly complex, can now be interpreted in terms of the two different sublattice types present in phase II of  $\text{CH}_4$ , coupled with the possibility of oxygen catalysis. Recently, theoretical studies of conversion in pure  $\text{CH}_4$ <sup>64</sup> and in oxygen catalysed  $\text{CH}_4$ <sup>65</sup> have been made. The calculations on pure  $\text{CH}_4$  show that the intramolecular nuclear spin dipole-dipole interaction is the dominant term mixing the various spin states, but it is the intermolecular

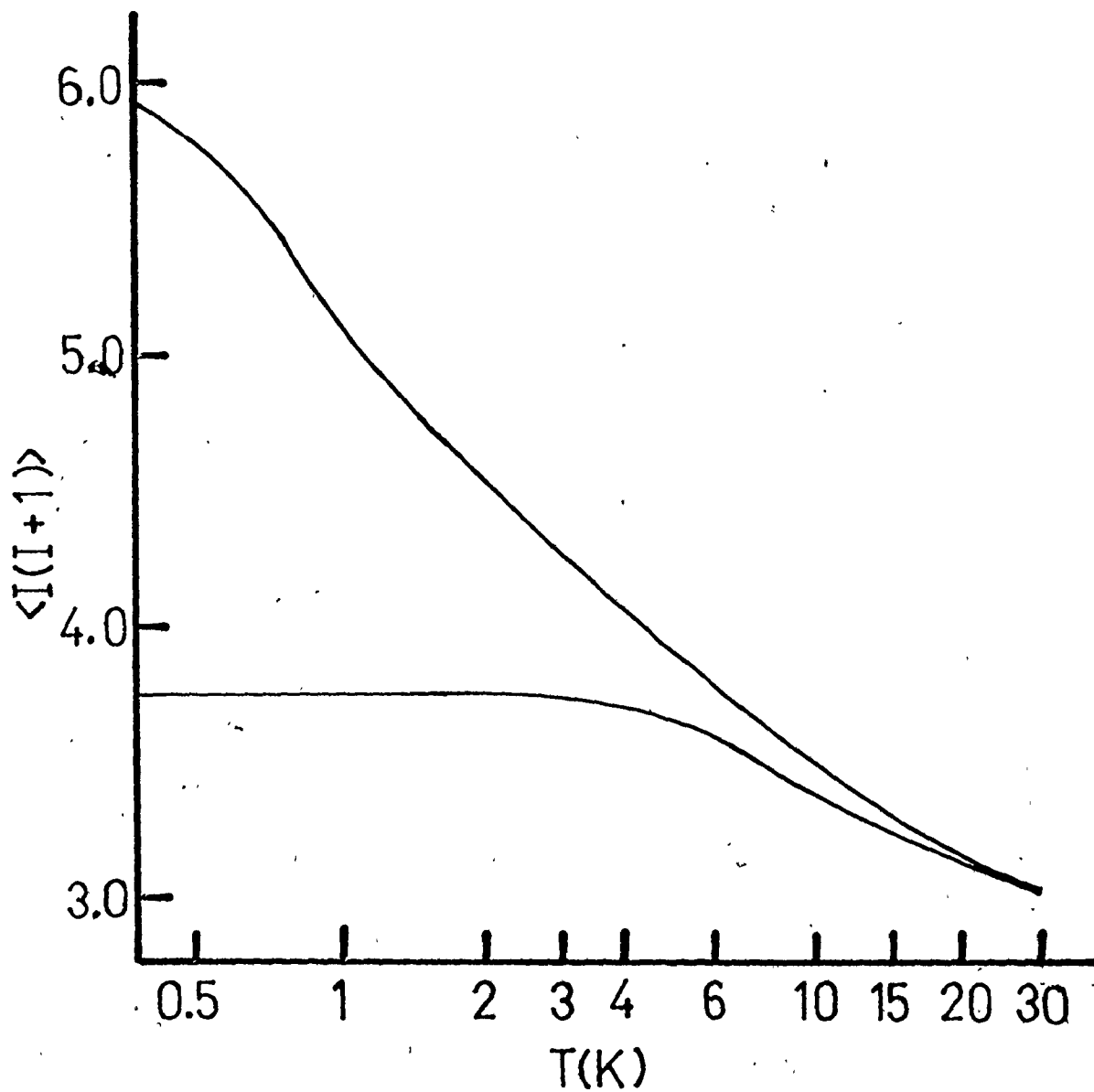


Figure 5. The temperature dependence of  $\langle I(I+1) \rangle$ , where the upper curve is for conversion on all sublattices in the phase II structure, and the lower curve for the disordered sublattices only.

octupole-octupole interaction, modulated by the necessary phonon emission, which induces the transition between the rotational-spin states. This mechanism leads to a calculated conversion time of two hours for the disordered sublattices, and a conversion time in excess of 2000 hours for the ordered sublattices. These results are in qualitative agreement with the most recent n.m.r. study<sup>66</sup>.

The calculations for the oxygen-doped  $\text{CH}_4$  were aimed primarily at obtaining a qualitative understanding of the catalysed conversion process. The calculation followed the method used for oxygen catalysed conversion in solid hydrogen<sup>3</sup>. The two spin states, A and T, are mixed by the fluctuating magnetic field which arises from the rotation of the  $\text{CH}_4$  in the field of the paramagnetic oxygen molecule. The calculation was restricted to the ordered molecules in phase II, and the results indicated that oxygen did provide a good pathway for the conversion process, but that, below  $T = 0.3 \text{ K}$ , the efficiency of oxygen as a spin conversion catalyst would be severely diminished.

Spin conversion also has a large effect on the measured heat capacities of methane. Early measurements of the heat capacity of  $\text{CH}_4$  in phase II down to  $T \sim 5 \text{ K}$  revealed a broad anomaly centred near  $T = 8 \text{ K}$ <sup>48,67</sup>, which was interpreted as evidence of a transition from phase II to phase III. Subsequent optical birefringence measurements in this region<sup>68</sup> gave some partial support for this interpretation, since a

weak birefringence was observed. Conversion between spin species was thought not to be the cause, because the entropy change in the anomaly was rather small ( $2.4 \text{ J mole}^{-1}\text{K}^{-1}$ ), even though it had been proposed that oxygen catalysed spin conversion might be occurring<sup>59</sup>. As will be shown in this thesis, kinetic results from neutron cross-section measurements correspond very well with results from the early thermal measurements, thus firmly establishing that the heat capacity anomaly around  $T = 8 \text{ K}$  is a consequence of spin conversion on the disordered sublattices. The counterpart for the ordered sublattices is found in the anomaly in the heat capacity centred near  $T = 1 \text{ K}$ , of oxygen catalysed  $\text{CH}_4$ , reported recently by Vogt and Pitzer<sup>49</sup>.

Spin conversion in the other four isotopic methanes is not so well documented, and limited data are only available for  $\text{CH}_3\text{D}$ <sup>69</sup>. Like the other deuterated methanes,  $\text{CH}_3\text{D}$  has three solid phases, and the molecules in phase III are probably in environments similar to the ordered molecules of phase II. Hence, the energy level spacings for the tunnelling levels should be small, and spin conversion could be expected to occur at very low temperatures. In  $\text{CH}_4$ , there are three levels in the low lying tunnelling states, each of different spin symmetry, and thus the existence of the Schottky-type anomaly confirms that conversion is occurring. In  $\text{CH}_3\text{D}$ , however, there are at least four levels and only two spin symmetry species. The existence of a Schottky-type

anomaly, therefore, cannot be taken as proof of spin conversion. The existence of spin conversion has now been established from deductions based on the entropy of  $\text{CH}_3\text{D}$ <sup>53,70</sup>. Figure 6 shows the entropy,  $S$ , as a function of  $T$  based upon the entropy of gaseous  $\text{CH}_3\text{D}$ , with the inclusion of the nuclear spin entropy for the protons and the deuterons, and thermodynamic data extending down to  $T = 0.15$  K. If the entropy at  $T = 0$  K is estimated by extrapolation from the region near  $T = 10$  K, then it is found to be  $R\ln 96$ . This indicates that, at  $T = 10$  K, no nuclear spin conversion or ordering of the deuterium position has occurred. The further reduction of the entropy below  $T = 4$  K corresponds to a large Schottky-type anomaly in the heat capacity<sup>52,53</sup>. If the data to the lowest experimental temperature are used, the entropy at  $T = 0$  K is estimated to be near  $R\ln 14$ . The full significance of this result will be discussed later in the thesis. Here, it is only necessary to note that the reduction in entropy is greater than  $R\ln 6$ , which exceeds the amount ( $R\ln 4$ ) that would be caused by preferential alignment of the C-D bond in the crystal structure. The excess change in entropy can only be caused by spin conversion.

An early, but inconclusive, n.m.r. susceptibility measurement on  $\text{CH}_3\text{D}$ <sup>71</sup> showed a slight increase in  $\langle I(I+1) \rangle$  below  $T = 2$  K. Recently, the n.m.r. susceptibility measurement has been repeated with a much improved technique<sup>69</sup> and the results definitely indicate that spin conversion occurs



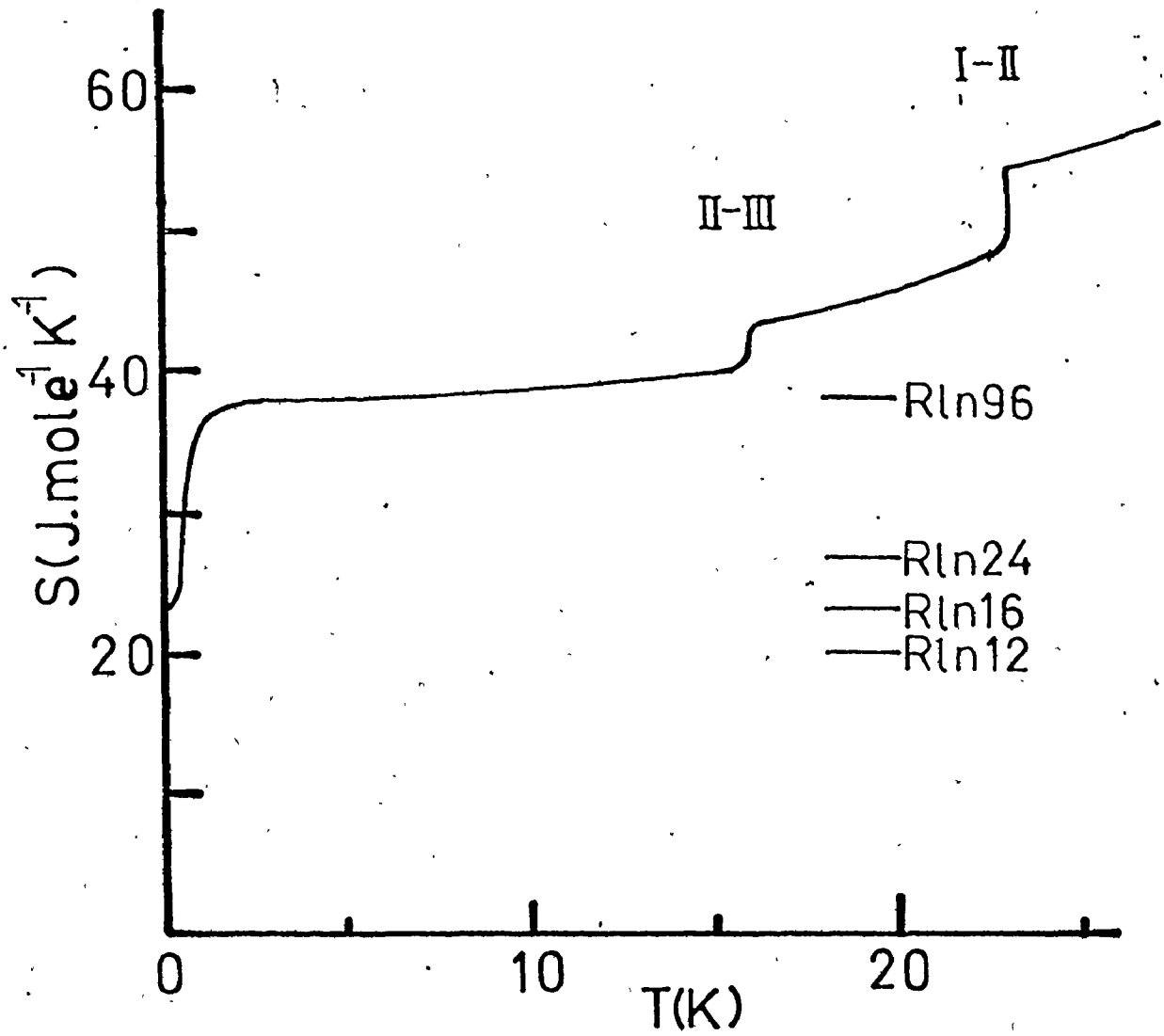


Figure 6. The low temperature entropy of  $\text{CH}_3\text{D}$

below  $T = 4$  K. No estimate of the rate of conversion or of the temperature dependence of  $\langle I(I+1) \rangle$  could be made. The neutron cross-section experiments to be described give more quantitative information about conversion, and the results can be correlated well with the available thermodynamic data.

There has been a suggestion<sup>52</sup> that conversion might also occur in solid  $\text{CH}_2\text{D}_2$  at low temperatures. Some evidence for this has been obtained from the neutron cross-section results.

## CHAPTER III

### NEUTRON SCATTERING - A NUCLEAR SPIN PROBE

#### III.1 Introduction

The sensitivity of neutron scattering to the nuclear spin state of a molecule has been well established for the ortho-, para-hydrogen<sup>4</sup> example<sup>72,73</sup>. For solid hydrogen, however, neutron scattering was never used to follow the conversion process. L.B. Borst made the first attempts to use the technique to detect conversion in methane, water and acetylene<sup>74,75</sup>. Unfortunately, the experiments yielded ambiguous results. Much later, Johnston and Collins<sup>63</sup> obtained clear, but qualitative evidence of spin conversion in CH<sub>4</sub>. No quantitative data of a quality comparable to that from n.m.r. experiments were obtained. The neutron scattering results reported in this thesis represent a further refinement of the technique used by Johnston and Collins, to the point where quantitative information about the spin conversion process has been obtained.

#### III.2 Neutron Scattering - General Theory

The interaction of slow neutrons, that is neutrons with thermal energy or less, with matter is strongly dependent on several factors. It depends on the thermal motion

of the scatterer, the interference between the scattered waves, the chemical bonds present in the scatterer, and, finally, on the nuclear spin state of the scatterer<sup>76</sup>.

Thermal neutrons have wavelengths comparable to interatomic spacings (1 to 5 Å), and therefore, neutron scattering provides an alternate diffraction method for the examination of the structure of solids, liquids and gases. Thermal neutrons have the further advantage that their energies are of similar magnitude to the energies of lattice vibrations, molecular vibrations and many other basic excitation processes in solids, liquids and gases. Inelastic processes in which the neutron loses or gains a significant fraction of its initial energy are easily detected, and make neutron scattering a powerful probe of the possible excitations and dynamics of a crystal<sup>77</sup>.

The range of the neutron-nucleus interaction is much shorter than the neutron wavelength ( $10^{-14}$  m), and the scattering potential can be approximated by a delta function centred on the nucleus. The scattering amplitude of the neutron wave from such a potential,  $f(k)$ , is spherically, symmetric for scattering from a single fixed nucleus, quite unlike the behaviour of  $f(k)$  for X-rays. Because  $f(k)$  is a constant, it is normally called the scattering length of the nucleus. If the values of the scattering lengths,  $b$ , are examined for the various elements<sup>78</sup>, it is immediately obvious that the values differ from one element to the next,

and they even differ from one isotope to another. In addition, the variation of the scattering length through the periodic table appears, at first glance, to be totally random. In fact, the scattering length contains contributions from two sources. The obvious source is that  $b$  is proportional to the size of the nucleus which should lead to a gradual increase of the scattering length with nuclear mass. Superimposed on this rather predictable trend is the more complex phenomenon of resonance scattering. In any nucleus, there are many energy levels, and a resonance interaction of the incoming neutron with the scattering nucleus can lead to radical changes in the scattering length<sup>78</sup>. The scattering length, which is always complex, can even become negative. These radical changes in the scattering length due to resonance interactions do not follow any trend with respect to mass number as do the scattering amplitudes for X-rays. Thus, neutron scattering provides a method of analysing structures not amenable to X-ray diffraction techniques.

To return to the simple case of a single nucleus fixed at an origin, the total cross-section,  $\sigma$ , of the nucleus is defined as

$$\sigma = 4\pi b^2. \quad [7]$$

The normal unit of neutron cross-sections is the barn ( $10^{-24}$  cm<sup>2</sup>). If the nucleus is free to move, however, the scattering takes place in a centre of mass frame of reference, and a correction must be made to the cross-section. If a

nucleus of mass  $M$  is bound in an otherwise inert free molecule of mass  $M$ , the total cross-section for scattering the neutron of mass  $m$  is reduced from the bound value shown in [7] to<sup>77</sup>

$$\sigma_{\text{mol}} = 4\pi \left( \frac{M}{m+M} \right)^2 b^2 \quad [8]$$

If the scattering occurs from a number of nuclei which are fixed in position, for example, in a molecule or a solid, the neutron scattering is characterised not only by the elastic and inelastic processes, but also by the phase relationship of the scattered neutron waves; whether the scattering is coherent or incoherent. Unlike X-rays, where incoherent (diffuse) scattering can only arise through disorder of chemically different species (for example an AB alloy), incoherent neutron scattering can arise from two additional sources: the random distribution of isotopes of the same element throughout the system, and the existence of non zero nuclear spins on the scattering nuclei. The first is simpler to illustrate.

Nickel has five commonly occurring isotopes, all with quite different scattering lengths<sup>79</sup> but, in the solid, an effective scattering length,  $\bar{b}$ , can be defined as the weighted average of the isotopic scattering lengths

$$\bar{b} = \sum_i w_i b_i \quad [9]$$

The effective scattering length determines the intensity of

the observed coherent scattering, which is, of course, responsible for diffraction. If equation [7] is recast for solid nickel, it becomes

$$\sigma = 4\pi \sum_i \omega_i b_i^2, \quad [10]$$

and a coherent cross-section can be similarly defined, except that  $\bar{b}$  is used:

$$\sigma_{\text{coh}} = 4\pi \bar{b}^2. \quad [11]$$

The incoherent cross-section is defined as the difference between the total cross-section and the coherent cross-section and is equal to

$$\sigma_{\text{inc}} = 4\pi (\overline{b^2} - \bar{b}^2). \quad [12]$$

Equation [12] shows that the incoherent scattering, due to the isotope distribution, is caused by the random fluctuations throughout the sample of the scattering length from its mean value. The formal result shown in [12] also applies to the case of nuclear spin incoherence, although the cause is perhaps more complex.

The resonance scattering term does not depend directly on the scattering nucleus, but rather on the compound nucleus formed by the neutron-nucleus system. If the scattering nucleus has a nuclear spin,  $I$ , the compound nucleus can have a spin of either  $I+\frac{1}{2}$  or  $I-\frac{1}{2}$ , and the resonance energy states for the two compound nuclei are completely different, as are

the scattering lengths<sup>79</sup>. The two possible scattering lengths are usually designated as  $b_+$  and  $b_-$  respectively. The expressions for the coherent and incoherent cross-sections, for elastic processes, are as follows<sup>80</sup>

$$\sigma_{\text{coh}} = 4\pi \left( \left( \frac{I+1}{2I+1} \right) b_+ + \left( \frac{I}{2I+1} \right) b_- \right)^2 \quad [13]$$

$$\sigma_{\text{inc}} = 4\pi \frac{[I(I+1)]}{(2I+1)^2} (b_+ - b_-)^2 \quad [14]$$

The incoherent cross-section is dependent upon the square of the difference between the two scattering lengths, and, for most nuclei with non zero spin, the difference is small as is the incoherent cross-section. Hydrogen is an exception in which the two scattering lengths are of opposite sign and roughly equal magnitude, which causes the incoherent cross-section to be very large (79.8b), - much larger than the coherent cross-section (1.8b). As the name implies, the incoherently scattered neutrons, whether from spin or isotope effects, cannot interfere with other scattered neutrons, or with the incident beam, because all of the phase relationships have been lost.

Neutrons scattered from a crystal can be divided into four groups. The collective properties of the scatterers are reflected in the coherent elastic and inelastic scattering processes<sup>76</sup>, while the incoherent elastic and inelastic scattering are associated with the scatterer



only, and no collective information is incorporated into the scattering<sup>81</sup>.

### III.3 Scattering from Hydrogenous Molecules

For scatterers containing hydrogen, such as methane, the cross-section is dominated by the incoherent scattering and, for such samples, the orientation of the crystal relative to the incident and scattered neutron beam is irrelevant. Polycrystalline samples are usually used, and the inelastic scattering can only yield information on the energy of excitations and the density of states for such excitation processes<sup>81</sup>. The elastic incoherent scattering normally contains very little information about the environment of the scatterer, except that it is affected by nuclear spin correlation within a molecule.

If spin correlation is, for the present, neglected then some useful generalizations about the behaviour of the cross-section of hydrogenous molecules can be made from both a theoretical and an experimental viewpoint. Most hydrogenous molecules are organic molecular crystals where the weak intermolecular interactions, coupled with the non-collective nature of the incoherent cross-section, have made common, the almost essential, assumption that the molecules can be effectively treated as free molecules. Almost all theoretical treatments to date have considered only the scattering from free gas molecules, neglecting the possible effects of a solid or liquid environment.

The complete theoretical expression for the total cross-section is deceptively simple. For an array of  $N$ , not necessarily identical, nuclei the total cross-section is given by,

$$\sigma = \int d\Omega \frac{k}{k_0} \sum_{i,f} g_i |\langle f | \sum_{j=1}^N \hat{b}_j \exp(i\vec{Q} \cdot \vec{r}_j) | i \rangle|^2, \quad [15]$$

where  $g_i$  is the thermal population factor of the initial state  $|i\rangle$ ,  $\vec{r}_j$  is the position vector of the  $j^{\text{th}}$  nucleus,  $\vec{Q}$  is the neutron momentum transfer,  $\vec{Q} = \vec{k} - \vec{k}_0$  and  $\hat{b}_j$  is the scattering length operator.

The sum in equation [15] is over all possible initial and final states of the system, and evaluating these matrix elements is very difficult, if not impossible, even for a simple system. Zemach and Glauber managed to circumvent the need to sum explicitly over all possible states through the use of a clever operator formalism<sup>82</sup>. They solved the two relatively simple cases of the translating nucleus and the rigid rotor. The calculation was then extended, with difficulty, to the specific case of methane<sup>83</sup>. A great simplification of the formalism was made by Krieger and Nelkin, but at the expense of generality<sup>84</sup>. The simplification involved approximations which made easier the handling of translational, rotational and vibrational contributions to the cross-section of the molecule. These approximations restrict the use of the theory to temperatures larger than the rotational constant of the molecule, to incident neutron

energies much larger than the rotational level spacings, and to systems where the effects of nuclear spin are absent. The theory has the advantage, however, that it provides an easily calculable expression for the cross-section, especially for molecules of high symmetry such as methane. Details are given in Appendix 1. A characteristic of cross-sections calculated by this method is their linear decrease with temperature. The slope of the line is primarily a function of an effective mass parameter derived from the mass tensor concept of Sachs and Teller<sup>85</sup>, which combines the rotational and translational behaviour of the molecule into one scalar representation, the effective mass. The physical interpretation of the decrease of the cross-section with temperature is entirely associated with the possible inelastic processes because, as the temperature decreases, the population of excited states decreases and the probability of inelastic energy gain processes diminishes accordingly. The elastic cross-section is temperature independent. The Krieger-Nelkin method has been very successful in describing the behaviour of many hydrogenous molecular systems in the gas, liquid and solid state<sup>72,86,87</sup>.

#### III.4 Neutron Scattering from Molecular Spin States

The incoherent cross-section expression [14] assumes that the neutron spin and the nuclear spin are randomly oriented, which then allows the ready evaluation of several spin expectation values<sup>77</sup>. In molecules with several

identical nuclei with non-zero spin, this assumption is no longer valid because the Pauli Principle forces correlation between the nuclear spins. When this occurs, the phase relationship between the nuclear spins on the like-nuclei is no longer random, and interference between neutrons scattered from these nuclei can occur. The exact nature of the additional terms in the cross-section due to coherent spin dependent scattering within the molecule could, in principle, be calculated from equation [15], but now  $b_j$ , the scattering length, is a spin dependent operator. An indication of the complexity of the problem can be obtained from the consideration of a special case, the neutron cross-section at long wavelengths. If the neutron wavelength is very long and only elastic scattering is considered, equation [15] simplifies to the form

$$\sigma = \int d\Omega \frac{k}{k_0} \sum_i g_i \left| \langle i | \sum_{j=1}^N \hat{b}_j | i \rangle \right|^2, \quad [16]$$

where the exponential has been expanded and the first term retained. The important term is the square of the expectation value of the spin dependent scattering length. When equation [16] is evaluated (see Appendix 2), it is evident that  $\sigma$  is proportional to  $\langle I(I+1) \rangle$  for the molecule. The additional interference term in the cross-section caused by spin correlation is associated with scattering off the spin state of the molecule, rather than the individual nuclei. It is this result that allows neutron scattering to act as

a probe of the molecular nuclear spin states and the accompanying effects of spin conversion. Spin correlation does not occur between molecules, except at very low temperatures, and the neutron waves scattered from different molecules cannot interfere. Hence, the neutron scattering appears totally incoherent to the external observer.

If the long wavelength restriction is removed, the effect on the relationship between  $\sigma$  and  $\langle I(I+1) \rangle$  is not obvious. Zemach and Glauber attempted to explain the additional spin-dependent term in the cross-section when they applied their theory to  $\text{CH}_4$ <sup>83</sup>. The result was again a term proportional to  $\langle I(I+1) \rangle$ , but modified by a matrix element related to the rotational motion of the molecule. Several authors have since tried to evaluate these terms with varying degrees of success<sup>88,89,90</sup>. The equivalent term for the simpler case of hydrogen<sup>76</sup> shows that, at finite neutron wavelengths, the magnitude of the proportionality constant between  $\sigma$  and  $\langle I(I+1) \rangle$  is reduced, but the form of the dependence is not altered. The extent to which the effects of correlated spins are observable is a direct function of the ratio of the neutron wavelength to the proton separation. This conclusion is supported experimentally in that the two spin species of solid hydrogen have clearly different cross-sections at wavelengths only slightly longer than the proton separation<sup>72,73</sup>, as is shown in Figure 7. Methane has a proton separation of 1.8 Å and, therefore, a neutron

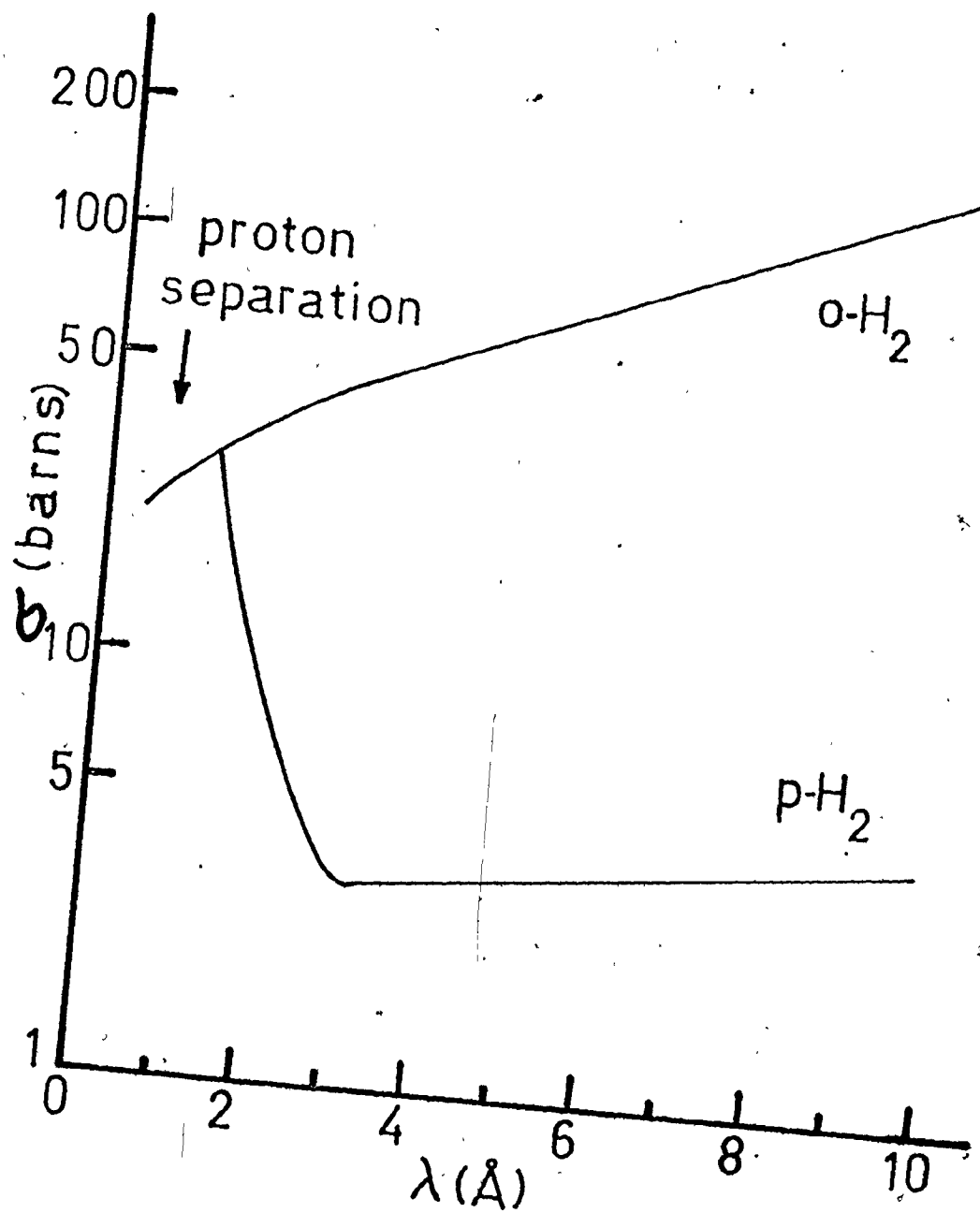


Figure 7. The total cross-section of liquid ortho- and para-hydrogen.

beam of at least that wavelength should be used if spin correlation effects are to be observed.

## CHAPTER IV EXPERIMENTAL

Accurate measurements of the total neutron cross-sections of the solid methanes required the development of a neutron spectrometer and a cryogenic apparatus to contain the methane samples at temperatures from as low as possible to the melting points. The samples also had to be analysed so that the data could be properly interpreted.

### IV.1 Sample Preparation

#### 1.1 Handling and Storage

Since a neutron beam with a large cross-sectional area was required to yield acceptable counting rates, the samples had to be rather large. For maximum sensitivity it was found necessary to use samples of about 0.1 moles of methane.

All samples were handled in a high vacuum system ( $P < 10^{-6}$  Torr), and manipulation of the samples within the system was accomplished with the use of liquid nitrogen and liquid helium. Once sample preparation was completed, the samples were transferred to lecture bottles which had been leak tested and baked out under high vacuum.



## 1.2 The Samples

(i)  $\text{CH}_4$ : Two samples were used. The first (Research Grade, Matheson) was condensed directly from the lecture bottle supplied by the manufacturer. Its purity was better than 99.99 per cent. Random batch analyses of this grade of methane by the manufacturer showed normal oxygen levels of 2 - 8 ppm.

The second sample was deliberately doped with oxygen. A small amount of oxygen (Research Grade, Merck, Sharpe and Dohme) was mixed with a large volume of Research Grade Methane at room temperature. The final mixture was estimated to be 0.66 mol per cent oxygen, which was subsequently verified by a gas chromatographic analysis of the sample.

(ii)  $\text{CH}_3\text{D}$ : Two samples of the monodeuterated methane were examined, but their preparation was more involved. Commercially available deuterated methanes are isotopically impure and usually contain an appreciable amount of air. It was not practicable to attempt to purify the samples isotopically using available gas chromatographic techniques<sup>91</sup>. The samples were, however, analysed mass spectrometrically to determine their isotopic compositions. The results are given in Table III. The composition determined for the  $\text{CH}_3\text{D}$  sample compares favourably with that for similar commercial samples used in other studies<sup>57,92</sup>.

Both  $\text{CH}_3\text{D}$  samples were drawn from the same manufacturer's lot and differed only in the effort applied to

remove other impurities. The first sample was used with no additional treatment, and from an analysis of the n.m.r. spin relaxation time ( $T_1$ ) in the liquid<sup>93</sup>, it was found to contain 1.2 mol per cent of oxygen. An effort was made to remove all traces of air from the second sample. It was exposed to a diffuse layer Misch metal (a cerium-lanthanum alloy) getter which has previously been shown to be very effective for the removal of air from methane samples<sup>94</sup>. For example, similar samples, used in n.m.r.  $T_1$  measurements, had no detectable levels of oxygen in them (less than 1 ppm.). In the limited handling of the sample after the gettering, some impurities were probably introduced, but the amount is estimated to be less than 10 ppm..

(iii)  $\text{CH}_2\text{D}_2$ : Only one sample of  $\text{CH}_2\text{D}_2$  was used. The sample was drawn directly from the material supplied by the manufacturer (Merck, Sharpe and Dohme). The air content was reduced somewhat by trap to trap distillation at  $T = 77 \text{ K}$ , which should have reduced the oxygen content to less than 500 ppm. No attempt was made to purify the samples isotopically, but a mass spectrometric analysis of the sample was made and the results are shown in Table III.

TABLE III

Isotopic Composition of Deuterated Methane Samples (mol %)

Sample	Composition:				
	CH <sub>4</sub>	CH <sub>3</sub> D	CH <sub>2</sub> D <sub>2</sub>	CD <sub>3</sub> H	CD <sub>4</sub>
CH <sub>3</sub> D	3.6±0.1	95.3±.1	0.9±0.2	0.2±0.1	-
CH <sub>2</sub> D <sub>2</sub>	-	2.2±0.2	97.8±0.2	-	-

#### IV.2 Cryogenics

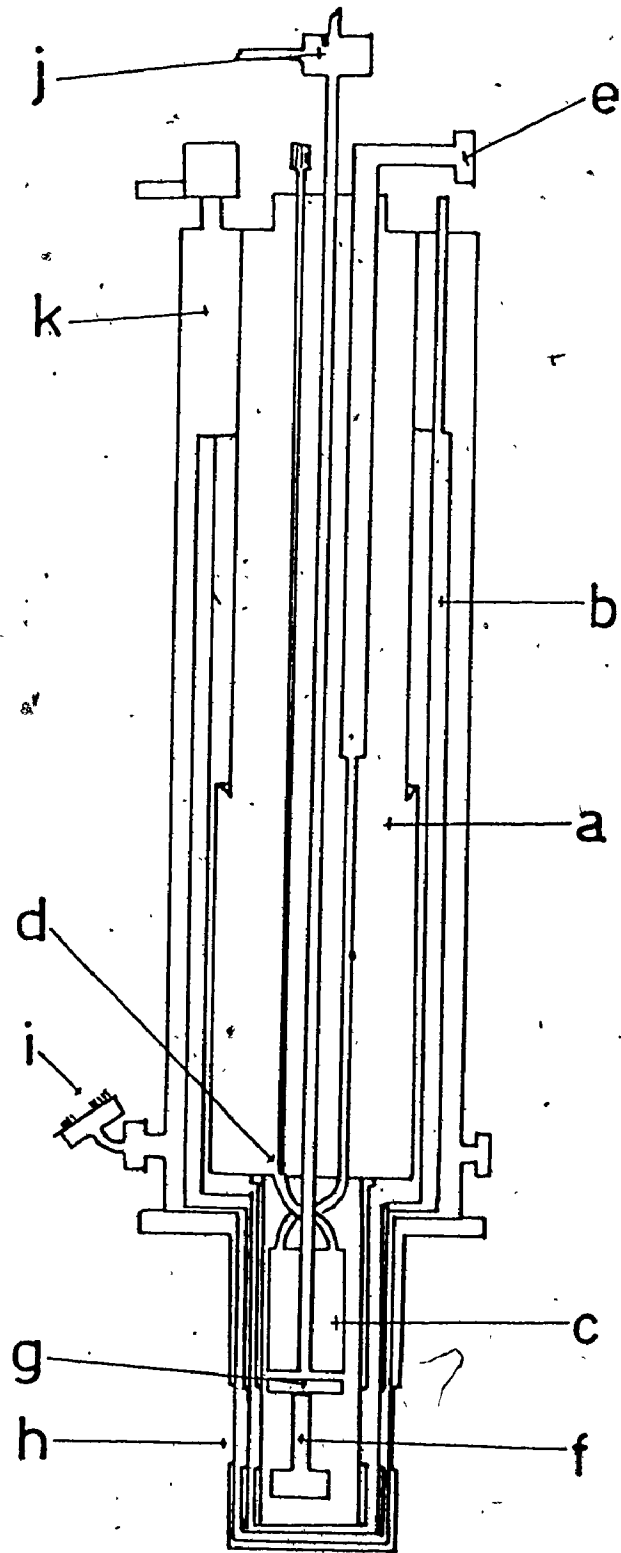
The cryogenic problems associated with the measurement of total neutron cross-sections at low temperatures were of three kinds: production and maintenance of low temperatures, the construction of a suitable sample cell, and the measurement and control of the temperature.

##### 2.1 Production and Maintenance of Low Temperatures

The main element of the cryogenic system was a commercial cryostat (Oxford Instruments, type MD4A) which included a special variable temperature insert that permitted studies over the temperature range from 1.3 K to 300 K. The insert consisted of a small vessel (125 cm<sup>3</sup>) suspended below the main helium-4 reservoir (see figure 8), and could be operated in two modes. To operate below T = 4.2 K, the insert was filled with liquid helium drawn from the main helium

Figure 8. The Cryostat

- a. liquid helium-4 reservoir
- b. liquid nitrogen reservoir
- c. variable temperature insert
- d. needle valve
- e. helium-4 pumping line
- f. sample cell
- g. liquid helium-3 reservoir
- h. neutron windows
- i. electrical lead ins
- j. helium-3 pumping line and sample inlet
- k. vacuum space



0 10cm.

reservoir through a needle valve. When the insert was full, the vapour pressure of the liquid was reduced by a high capacity rotary oil pump (190 l/min) thereby reducing the temperature to 1.3 K, a temperature that could be maintained for about four hours. If additional low temperature operation was required, the insert had to be refilled, a procedure that could be performed very quickly (1 to 2 minutes).

To operate above  $T = 4.2$  K, a different procedure was required. The insert was constructed of a low conductivity steel alloy, and a considerable temperature gradient could be imposed across it. By evacuating the insert vessel and then reintroducing controlled pressures of helium gas, the heat flow from the sample stage to the main liquid helium reservoir could be precisely controlled and the temperature of the sample varied continuously up to  $T = 100$  K.

The cryostat had two other special features: a central tube (5 mm in diameter) to the sample vacuum space which carried a filling tube to the cell, and a tail assembly constructed entirely of aluminum, which had thin sections to act as neutron windows. (Aluminium has a very low neutron cross-section.) The total thickness of aluminium in the window region was less than 1.5 mm. The neutron windows were large enough to ensure that the majority of the sample vacuum space was accessible to the neutron beam.

After several preliminary experiments, it was obvious that a great deal of interesting data might be obtained at

still lower temperatures and so the feasibility of constructing a helium-3 refrigerator within the existing cryostat was investigated. There were several spatial problems to be overcome because of the limited sizes of the central tube and the sample vacuum space in the tail assembly.

The helium-3 refrigerator was constructed in such a way as to make minimum alterations to the basic cryostat. A small copper chamber and a connected filling line for condensation of the helium-3 were added. The chamber was cylindrical with a volume of  $12.5 \text{ cm}^3$  (see figure 10). The dimensions of the pumping line, which also served as the filling line, determined the lowest accessible temperatures of the refrigerator. Two tubes had to pass through the central access tube without touching the cold walls ( $T = 4.2 \text{ K}$ ). The sample filling tube was made of stainless steel (1 mm O.D. and 0.1 mm wall thickness), and wound with an insulated manganin heater ( $300 \Omega$ ) which was used to prevent blockage of the tube during cooling of the sample. The heating wire also insulated the tube from the walls of the central tube and the helium-3 pumping line, which occupied the remainder of the space within the central shaft.

At the low temperature end of the pumping tube, near the helium-3 reservoir, the mean free path of helium (0.1 mm) was smaller than the diameter of most tubing and the gas flow through such tubing was viscous while, at the room temperature end, the mean free path was much larger (15 mm)

than the diameter of the central tube and the flow was molecular. A calculation of the flow impedance of the pumping line, using empirical formulae<sup>95</sup> derived for the various flow regimes, indicated that the short, small diameter section of the pumping line at the top of the central tube was the flow limiting section of the system. It is the pumping speed which, of course, determines the refrigeration capacity of the system. The final configuration of the pumping tube was a short section of 4 mm O.D. stainless steel tubing near the top of the shaft, where it could be allowed to touch the walls, followed by a longer section of 3 mm diameter tube down to the variable temperature insert. At this point, a short section of copper tubing was put into the line and thermally anchored to the variable temperature insert. During the operation of the helium-3 refrigerator, the insert was kept at  $T = 1.3$  K and the short section of copper tubing aided the condensation of the helium-3. Below the copper tubing, the line was reduced to a 2 mm diameter stainless steel tube which had two staggered  $90^\circ$  bends prior to entering the helium-3 condensation chamber. The bends acted as radiation baffles for the pumping line.

The helium-3 refrigerator had to be thermally isolated from the rest of the cryostat. The cryostat was always operated under high vacuum at pressures always lower than  $2 \times 10^{-6}$  Torr, and the effects of thermal radiation were reduced wherever possible by radiation shields anchored

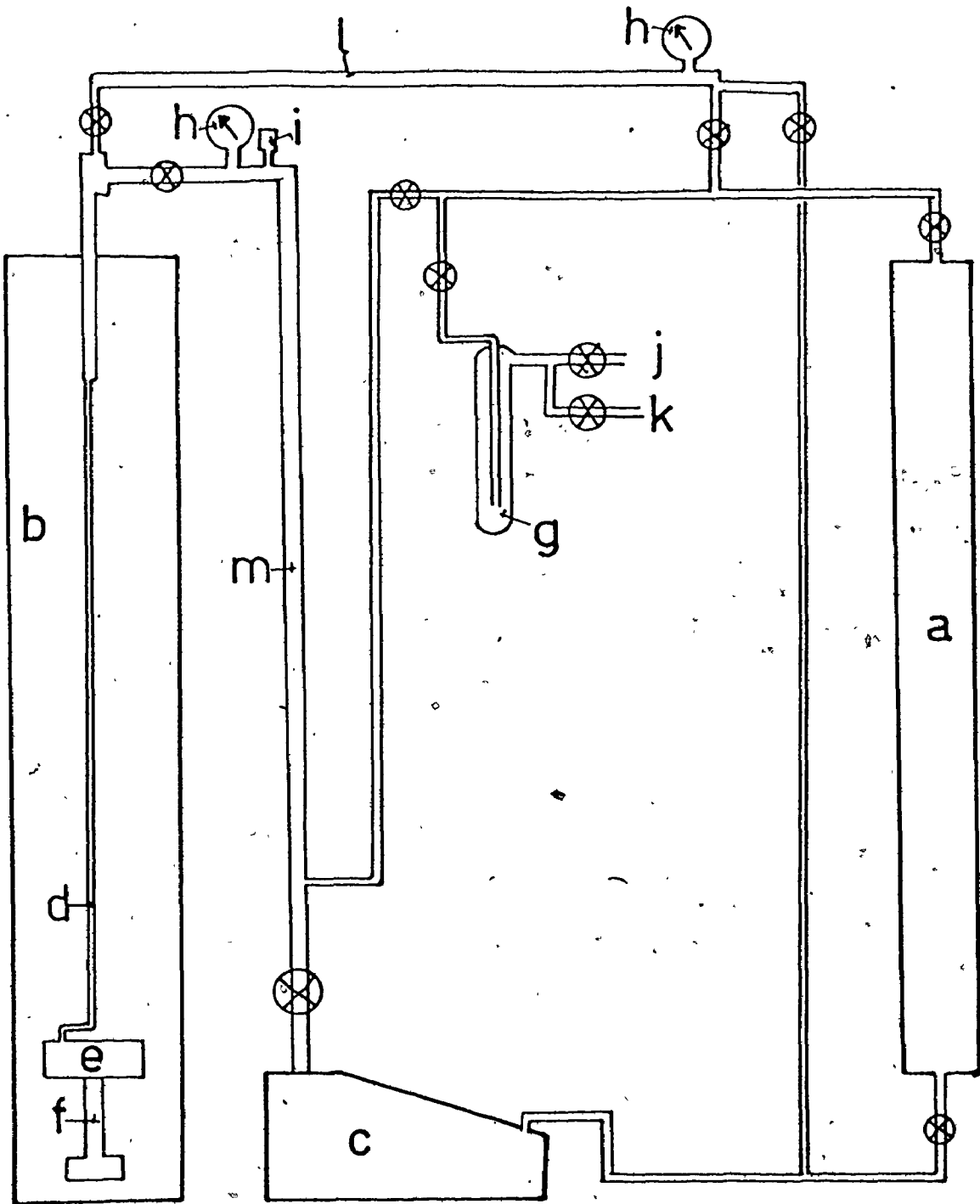


either to the liquid nitrogen or the liquid helium reservoir, With these two factors minimised, the major source of heat influx was conduction down the electrical leads. All wiring terminated at three ten-pin electrical connectors mounted near the base of the cryostat (see figure 8). The electrical leads into the cryostat were #40 copper for low current application and #36 copper for higher current use. Two metres of wire were used between the external connectors and the first thermal anchor on the liquid nitrogen reservoir and a further 1.5 metres, between the liquid nitrogen and the liquid helium reservoir. At the base of the liquid helium reservoir as many copper wires as possible were converted to constantan (#36) to reduce thermal conduction to the sample cell. At the juncture of the two dissimilar metals, great care was taken to ensure that all the joints would remain isothermal, thus reducing possible thermal emf. problems. Thin-walled (0.1 mm) stainless steel tubing was used for the filling and the helium-3 pumping lines to reduce thermal conduction down their lengths.

In order to operate the cryostat both above and below  $T = 4.2$  K, however, it was necessary to introduce a controlled heat leak between the sample chamber and the variable temperature insert. This was accomplished by a strip of ultra pure tin (99.9998 %) which acted as a superconducting heat switch<sup>96</sup>. Below the superconducting transition temperature (3.7 K), the thermal conductance of the

Figure 9. The Helium-3 Refrigerator (Schematic)

- a. Helium-3 gas reservoir (7 litres)
- b. cryostat
- c. sealed rotary oil pump
- d. condensation line
- e. helium-3 liquid reservoir
- f. sample cell
- g. charcoal trap
- h. pressure gauge
- i. pirani gauge
- j. gas inlet
- k. to high vacuum system
- l. filling line
- m. pumping line



switch decreased by almost two orders of magnitude and thermally isolated the cell. Above  $T = 3.7$  K, the switch became a controllable heat leak to the cell.

To operate the helium-3 refrigerator, the variable temperature insert was maintained at 1.3 K, and helium-3 gas was introduced into the helium-3 reservoir and pumping line. By maintaining an overpressure of helium-3 vapour a small quantity of helium-3 was condensed. The vapour pressure over the liquid was then reduced to approximately  $2 \times 10^{-1}$  Torr using a sealed rotary oil pump. In the usual experiment, the helium-3 refrigeration system and the sample attained a stable minimum temperature of 0.75 K which could be maintained for about four hours. The helium-3 handling system was entirely sealed, and the gas could be manipulated within the system with the use of the rotary pump. Periodically, the gas was purified by passing it through a cooled ( $T = 77$  K) charcoal adsorption trap. A schematic layout of the helium-3 refrigerator is shown in figure 9.

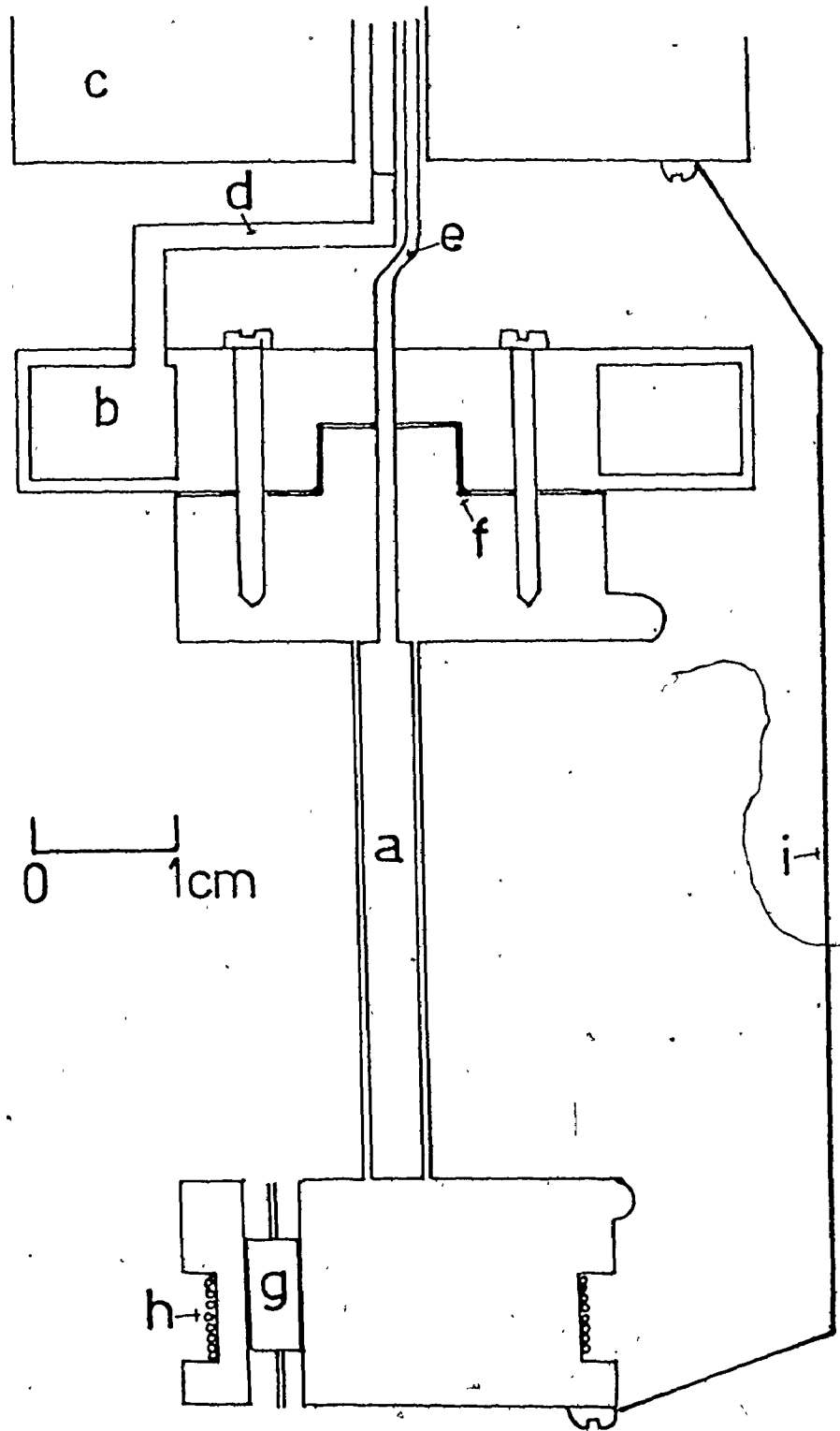
## 2.2 The Sample Cell

The sample cell was made an integral part of the helium-3 refrigerator for two reasons: to ensure that the cell and the helium-3 liquid reservoir maintained good thermal contact, and to overcome a constructional difficulty. The sample filling tube had to be made from stainless steel to minimise heat flow, while the sample cell needed to be of aluminium to maximise the neutron transmission. A reliable,

Figure 10. Cross-sectional View of Sample Cell and Helium-3 Reservoir

- a. sample volume
- b. liquid helium-3 volume
- c. variable temperature insert
- d. helium-3 condensation and pumping line
- e. sample introduction tube
- f. indium seal
- g. carbon resistance thermometer
- h.  $50\Omega$  heater
- i. tin heat switch





low temperature seal between the two metals proved to be almost impossible to prepare. Good thermal contact and a reliable seal were achieved, however, by joining the sample cell to the helium-3 reservoir through an indium seal. The filling tube was then soldered into the copper helium-3 reservoir through which a 1 mm. diameter hole had been bored to coincide with a similar hole in the aluminium cell. The final arrangement is shown in figure 10.

The rectangular sample cell was constructed with its two largest parallel faces machined to a thickness of 0.4 mm for high neutron transmission. The remainder of the cell was kept as massive as possible to minimise thermal gradients. The internal volume of the cell was  $2.20 \text{ cm}^3$ , and the cell thickness, a crucial parameter in the cross-section calculations, was determined to be  $0.355 \pm 0.002 \text{ cm}$ . The base of the cell was designed to accommodate the resistance thermometer, a resistive heater, and the tin superconducting heat switch. The neutron windows were defined with sheet cadmium, a material of very high neutron cross-section, to ensure that neutrons could only pass through the volume containing the methane sample.

### 2.3 Measurement and Control of the Temperature

The wide range of temperature over which the cryostat operated necessitated the use of two types of thermometer. At the lowest temperatures, below 4.2 K, a resistance thermometer was used to determine the sample temperature while,

above 4.2 K, a thermocouple was used. The resistance thermometer was a carbon composition resistor (Speer, 200  $\Omega$ ,  $\frac{1}{4}$  watt) mounted in the base of the cell (see figure 10) with a light coating of grease to improve thermal contact. The electrical leads were wrapped around and varnished to the base of the cell to enhance the thermal contact. The resistance was measured using a standard four-probe technique, with the current supplied by a very stable mercury battery (1.40 V) and a current limiting resistor. In normal operation, a current of 5-10  $\mu$ A was used, and the voltage across the resistance was measured with the current passing in both directions to eliminate thermal emf. effects. The resistance was determined by comparison with an accurate standard resistor (300  $\pm$  0.001  $\Omega$ ). Using this technique, the resistance could be reproduced to within 0.1  $\Omega$ , and seemed to be unaffected by thermal cycling.

The thermometer was calibrated by comparing its indication with those of a helium-3 vapour pressure thermometer and a calibrated germanium thermometer. The R-T relationship is displayed in figure 11 which also shows the relationship for a similar Speer resistor<sup>97</sup>.

Above  $T = 4.2$  K, several thermocouples were used to monitor the sample temperature and to measure temperature differences between various elements of the cryostat. The thermocouples are listed in Table IV. All of the thermocouples were insulated and stuck to metal surfaces with



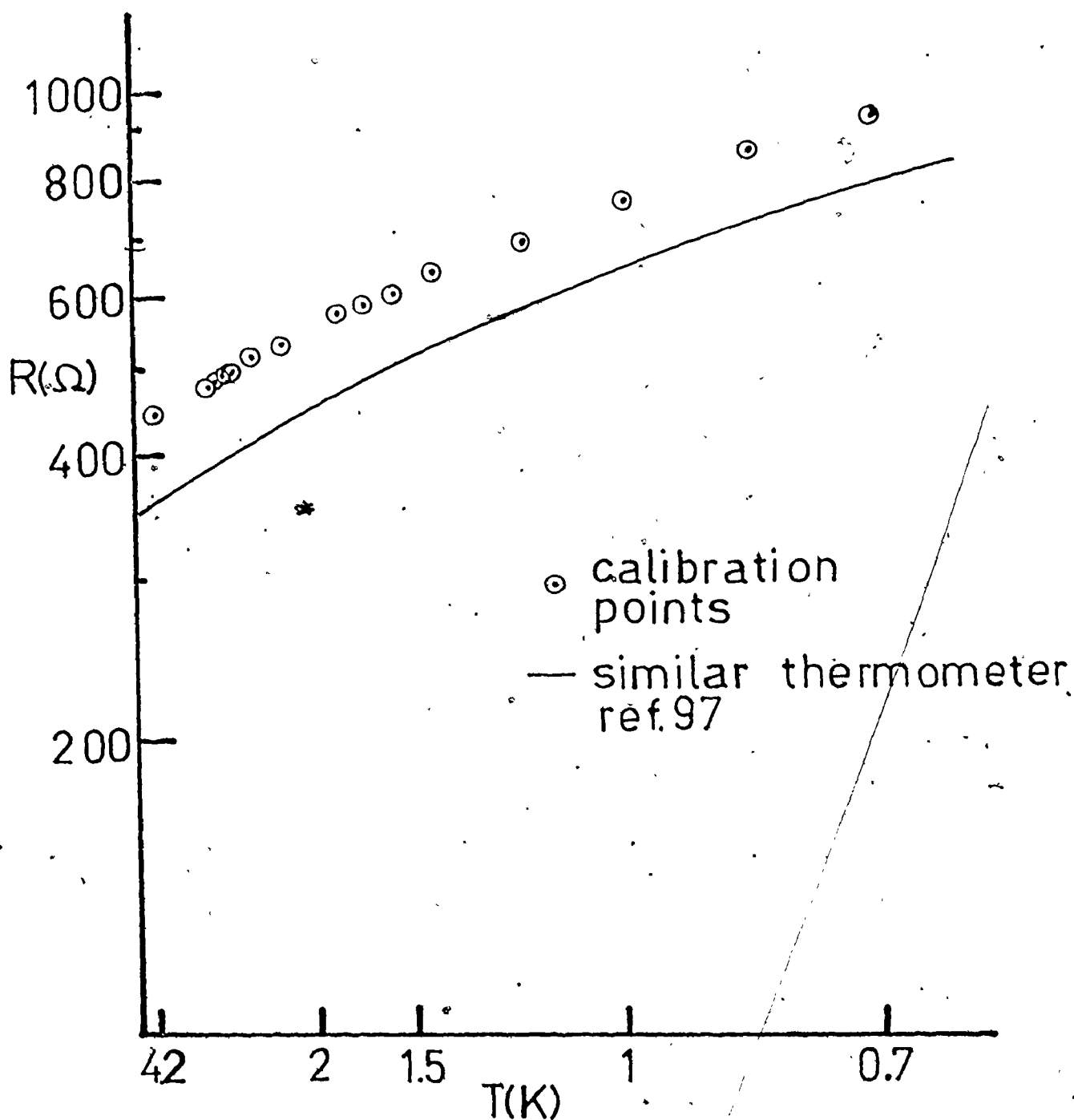


Figure 11. The resistance-temperature curve for the carbon thermometer.

Glyptal varnish to ensure good thermal contact. Thermocouples 1 and 2 provided an absolute measure of the temperature of the variable temperature insert and the sample cell respectively, because they were referenced to the stable temperature of the helium-4 reservoir. They could measure temperature differences of  $\pm 0.05$  K over the temperature range from 1.5 K to 100 K. Thermocouple 1 had been calibrated by the manufacturer of the cryostat, from  $T = 1.45$  K to  $T = 300$  K. Thermocouples 3, 4 and 5 were only used to measure temperature differences.

TABLE IV  
Thermocouples

<u>Reference Number</u>	<u>Material</u>	<u>Position</u>
1	gold-0.05 atm.% iron vs chromel-P	Helium-4 reservoir to variable temperature insert
2	gold-0.07 atm.% iron vs chromel-P	Helium-4 reservoir to sample cell bottom
3	chromel vs constantan	variable temperature insert to sample cell bottom
4	chromel vs constantan	sample cell bottom to sample cell top
5	copper vs constantan	variable temperature insert to gas inlet tube

Temperature control above 4.2 K was effected in two stages. The variable temperature insert was first set to a

temperature slightly below that of the sample, with a simple on-off controller (Shinko) which used a carbon resistor (Ohmite, 100  $\Omega$ ,  $\frac{1}{4}$  watt) mounted on the base of the insert as a temperature sensor. The controller regulated the passage of preset currents (0 - 100 mA) through the 100  $\Omega$  heater in the base of the insert. By this method, the temperature of the insert could be controlled to better than 0.1 K over most of the temperature range studied. The second stage of control used a fully proportional controller, designed for low temperature use<sup>98</sup>, with thermocouple 2 as the temperature sensor. The heating current could vary from 0 to 100 mA through the 50  $\Omega$  manganin coil wound on the base of the sample cell. The use of both controllers regulated the sample temperature, for periods of several hours, to better than  $\pm 0.01$  K, over the temperature range from 4.2 K to 100 K.

Sample temperatures between 1.4 K, the minimum sample temperature using the variable temperature insert, and 4.2 K were controlled by operating the insert at 1.3 K, and then passing a small constant current (0 to 5 mA) through the cell heaters. This method could control the cell temperature to within  $\pm 0.025$  K, for several hours.

### IV.3 The Neutron Scattering Experiment

#### 3.1 The Neutron Spectrometer

A long wavelength, moderate intensity neutron beam was required to measure precise neutron cross-sections, which would best show the effects of nuclear spin species conversion.

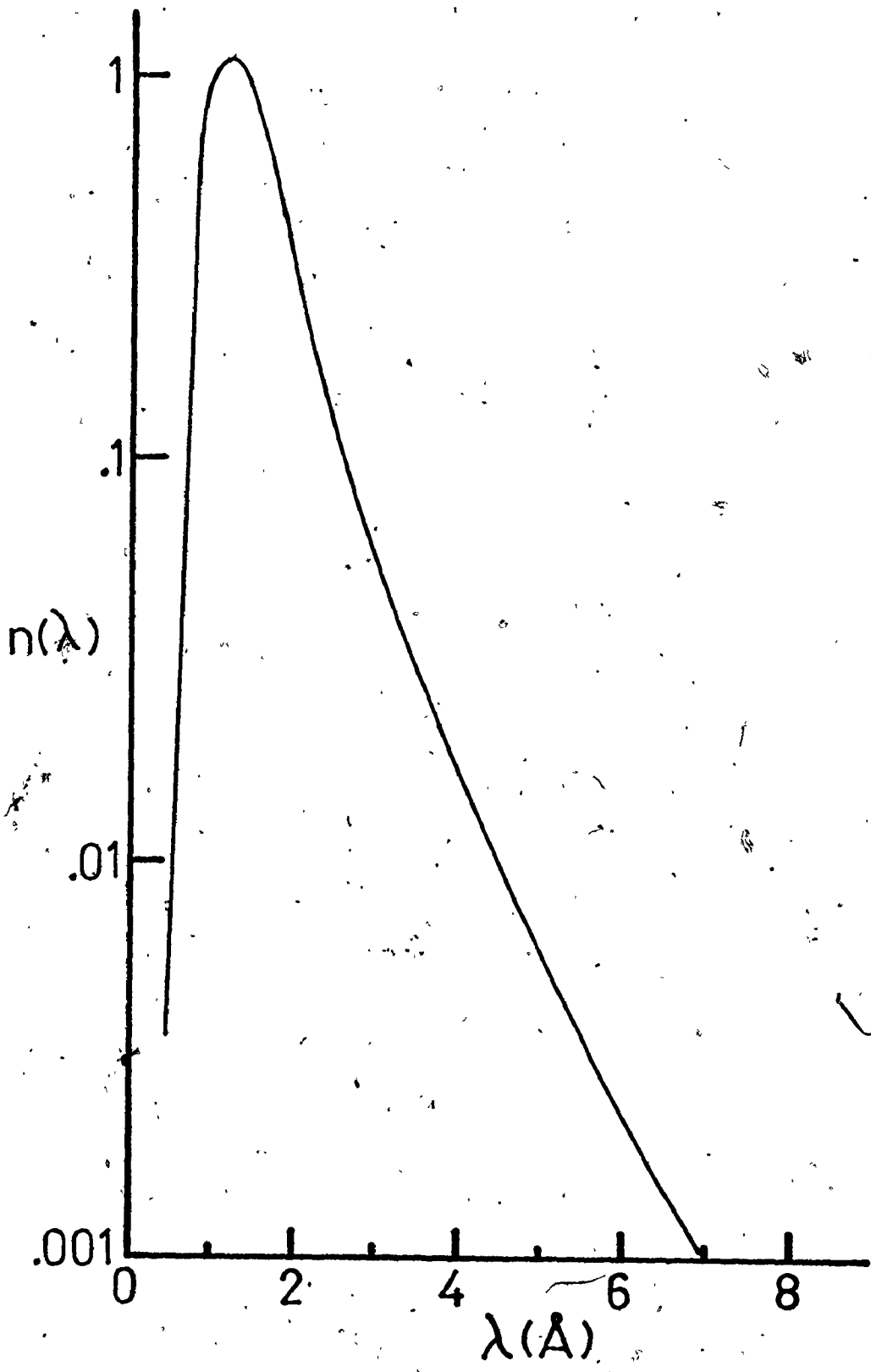


Figure 12. The neutron wavelength distribution from a thermal neutron reactor

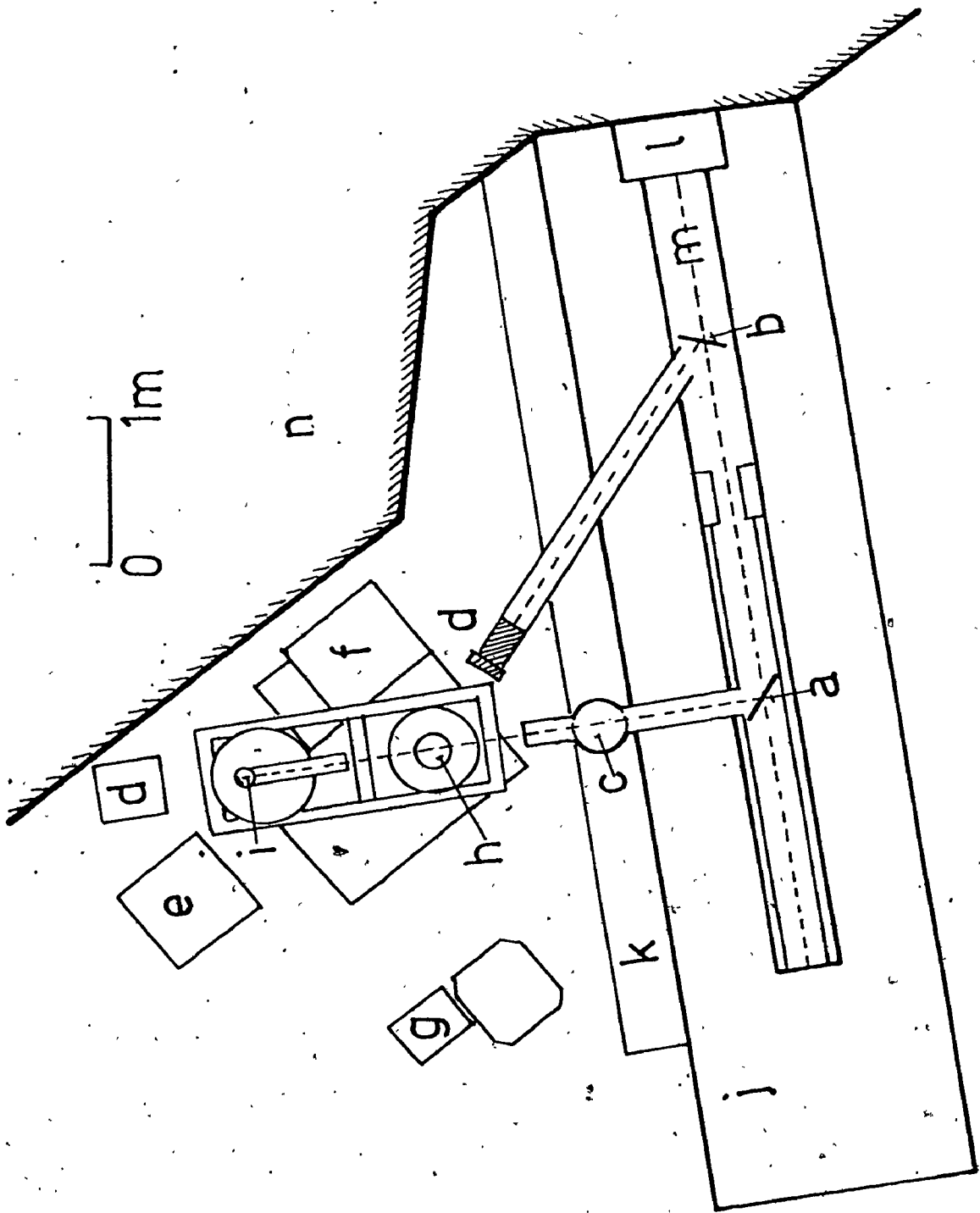
Unfortunately, these two requirements were diametrically opposed for a neutron beam from a thermal neutron nuclear reactor. The wavelength distribution from such a reactor, with a moderator temperature of 315 K (the operating condition of the McMaster Nuclear Reactor), is shown in Figure 12, - note the long tail extending to higher neutron wavelengths. As the wavelength increases, the neutron intensity drops sharply, - so much so that, at a wavelength of  $5\text{\AA}$ , the intensity is a factor of 200 less than that of the maximum. In any total cross-section experiment the final operating point would have to be a compromise between these two factors: wavelength and intensity.

While neither of the neutron spectrometers at the McMaster Nuclear Reactor was ideally suited for long wavelength total cross-section measurements, it was decided that the fixed wavelength ( $1.06\text{\AA}$ ) twin-axis neutron spectrometer was the better one to modify<sup>99</sup>. The long wavelength monochromatic neutron beam was produced by Bragg reflection from a single crystal of pyrolytic graphite, and the spectrometer modification involved the installation of a graphite monochromator and beam tube.

The physical arrangement of the existing twin-axis spectrometer is shown in Figure 13. The positioning of the graphite monochromator was determined by the largest interplanar spacing in graphite which is known to be  $6.7\text{\AA}$  and, to obtain neutrons with wavelengths near  $5\text{\AA}$  from such a

Figure 13. Twin-Axis Spectrometer

- a. graphite monochromator (4.7Å)
- b. aluminium monochromator (1.06Å)
- c. beryllium filter
- d. beam stop
- e. helium-3 circulation system
- f. vacuum system
- g. counting electronics
- h. specimen table
- i. helium-3 proportional counter
- j. water-filled shielding tanks
- k. paraffin
- l. main gate on neutron beam
- m. "white" neutron beam emerging from reactor
- n. reactor pool wall.



monochromator, the diffraction angle,  $2\theta$ , has to be near  $100^\circ$ . Access through the water-filled shielding tanks limited the available monochromator positions to a range of values for  $2\theta$  from  $60^\circ$  to  $95^\circ$ :

The monochromator base, rigidly mounted on a lathe bed, was connected to the centre of the spectrometer sample table by a telescoping aluminium beam tube, of 7x7 cm cross-section, which ensured the correct alignment of the neutron beam with respect to the sample mounting position.

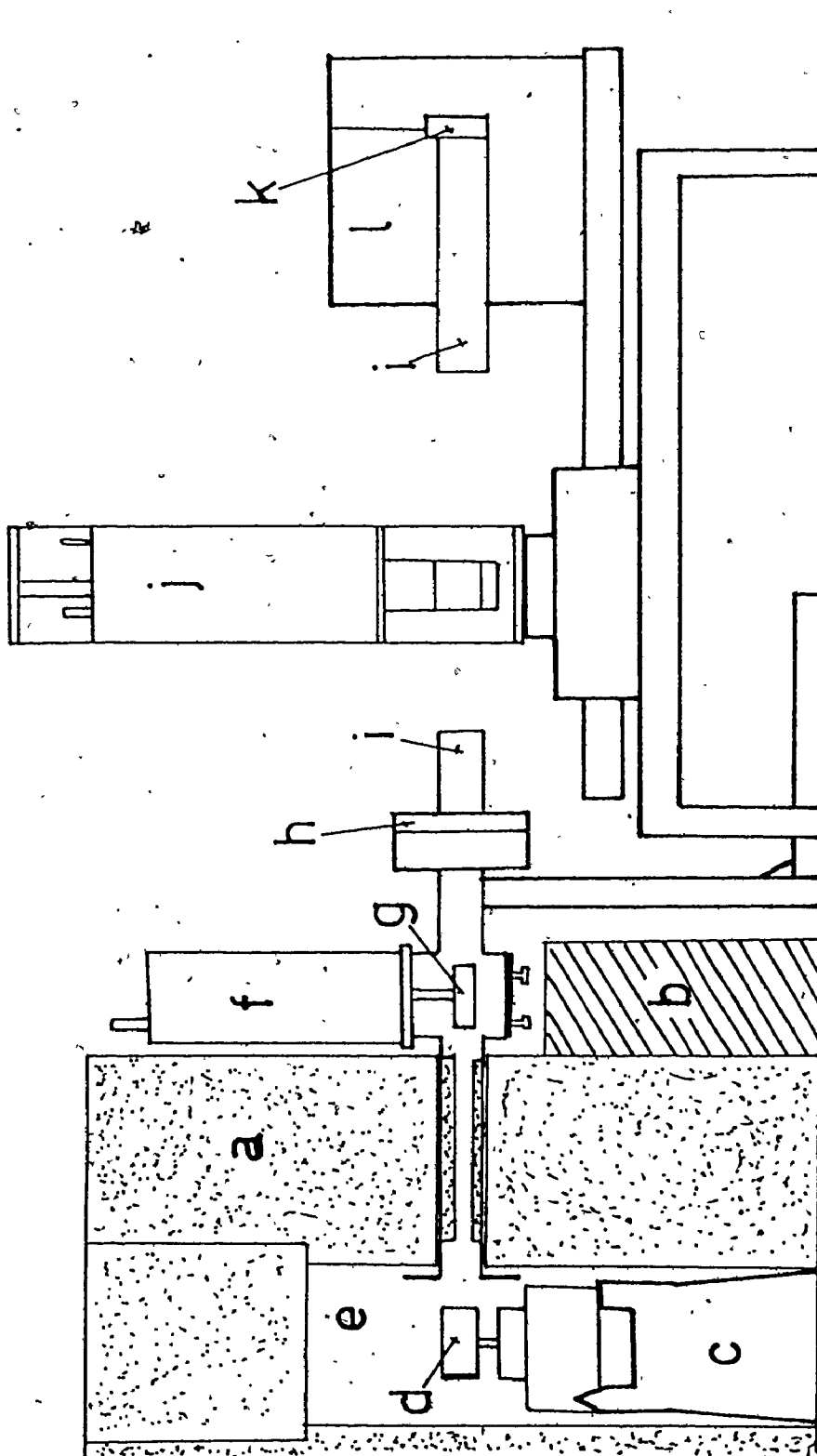
The monochromator was an oriented graphite single crystal (Union Carbide), 9.2 cm x 5.1 cm x 0.16 cm, with the c-axis of the crystal perpendicular to the largest crystal face, and a mosaic spread of  $0.8^\circ$ . The large mosaic spread increased the intensity of the beam significantly, and the loss of monochromaticity of the beam did not affect the neutron total cross-section experiment to any great extent.

In Figure 14, a cross-sectional view of the beam starting from the monochromator is shown. In the first section of the beam tube, the neutron beam was reduced in size and roughly collimated, to a divergence of  $1.5^\circ$ , by a long plug of polymethylmethacrylate and cadmium. At longer wavelengths, higher order Bragg reflections from the monochromator were troublesome, but the problem was alleviated by the use of a polycrystalline beryllium filter which selectively removed neutrons from the beam whose wavelength



Figure 14. Cross-sectional View of the Neutron Beam

- a. water-filled shielding tanks
- b. paraffin wax shielding
- c. lathe bed
- d. graphite monochromator and mount
- e. neutron beam channel
- f. beryllium filter cryostat
- g. beryllium filter
- h. monitor helium-3 proportional neutron counter
- i. soller slits
- j. cryostat
- k. main helium-3 proportional neutron counter
- l. paraffin wax shielding



was less than the Bragg cut off for beryllium<sup>100</sup> (3.96Å). The efficiency of the filter was further improved by cooling the cylindrical block of beryllium (5 cm dia x 10 cm) to liquid nitrogen temperatures, thus drastically reducing the number of inelastic processes which deplete the primary beam intensity. Cooling of the filter doubled the usable neutron flux.

The intensity of the neutron beam from the reactor was found to fluctuate quite seriously over periods of several hours, but the effect of these fluctuations on the cross-section measurements was overcome by introducing a split beam arrangement, where one portion of the beam was put into a reference counter, and the other through the sample. The reference helium-3 proportional counter was mounted just after the beryllium filter (see Figure 14) and could be adjusted to intercept any fraction of the beam desired. The counter was heavily shielded with polymethylmethacrylate, paraffin wax and cadmium to keep the background neutron count to a minimum.

The portion of the beam not intercepted by the reference counter was then collimated to 0.8° by a set of Soller slits, and the beam masked with cadmium so that it was rectangular (2.0 cm x 4.5 cm) and symmetric about the beam tube centre. The beam passed directly through the central axis of the specimen table, 15.3 cm above the surface of the table. Its intensity was measured with the main

twin-axis helium-3 proportional counter which was encased in a large drum of paraffin wax with cadmium sheet surrounding the portions of the counter not in the beam. To limit the detection of low angle scattered neutrons, a second set of Soller slits was placed in front of the counter.

### 3.2 Operating Conditions and Calibration

Initially, both helium-3 proportional counters were adjusted to their optimum operating conditions: the high voltage supplies were adjusted to put both counters in their plateau regions and the amplifiers were set to yield an average signal of 5 volts. The discriminators were adjusted to remove unwanted noise from the signal.

The beam position was established by rocking the main counter through the zero angle position to find the approximate location of the beam centre. With the counter in this position, the monochromator angle was varied in  $0.1^\circ$  steps until maximum intensity was achieved. The main counter was then rocked through the zero position to determine the exact beam position and profile. The beam was  $1.6^\circ$  FWHM. Once the zero position was known, the reference beam monitor was adjusted to have a similar counting rate to that of the main counter.

Wavelength calibration was accomplished by an examination of various powder diffraction patterns. The powder pattern of polycrystalline copper was examined with the beryllium filter out of position, and the various Bragg

reflections due to the  $\lambda/2$  and  $\lambda/3$  components of the beam were easily observed upon scanning the main counter through a range of 20 values from  $0^\circ$  to  $130^\circ$ . The first Bragg reflection (110) from the primary beam ( $2\theta = 135^\circ$ ) was beyond the range of the instrument. The powder pattern of polycrystalline lead was also examined. In this case, however, several reflections due to the primary beam were detected, as well as the reflections due to the  $\lambda/2$  and  $\lambda/3$  beam components. The lead powder pattern was measured with and without the beryllium filter in position to test the efficiency of the filter.

Analysis of the powder patterns indicated that the neutron wavelength was  $4.73 \pm 0.02 \text{ \AA}$ . The efficiency of the beryllium filter was difficult to estimate because all of the Bragg reflections due to the higher order beam components disappeared, relative to the background noise, when the filter was in position. This implied that the maximum fraction of the beam due to the higher order components was less than about 0.01, while, with the filter out, these components composed about 80 per cent of the beam.

### 3.3 The Experimental Configuration and Counting Methods

Once the initial operating conditions were established, the main counter was returned to the zero position and clamped in place. The entire spectrometer assembly was made as rigid as possible to minimize the effect of instrumental fluctuations on the cross-section measurements.

The cryostat, firmly mounted in an aluminium frame, was then accurately centred on the spectrometer specimen table by two locating pins and securely fastened in place. The cryostat height was adjusted, using bolts in the mounting frame, to make the centre of the sample cell coincide with the neutron beam centre. The orientation of the cryostat was checked to ensure that the sample cell was perpendicular to the beam direction. The cadmium mask on the cell was larger than the incident beam, thus further reducing the beam size before the beam passed through the sample.

A measurement of the total cross-section of a sample involved determining the neutron transmission of the sample, that is, determining the ratio of the beam intensity with and without the sample in the beam. The reproducibility of the transmission measurements was greatly increased by the split beam monitor system where the neutron count on the reference counter was used to determine the counting interval of the main counter. This arrangement compensated for the neutron flux variations which would have lowered the level of reproducibility if fixed time counts were used. In a normal experiment, the reference counter was used as a preset trigger for the main counter and, when the preset monitor count was reached, the count registered on the main neutron counter was stored on paper punched tape. The monitor was then automatically reset and the sequence repeated. To increase the precision of the data, large

preset values of the monitor count were used, typically 200,000, to achieve good counting statistics. Such preset levels allowed about forty count sequences per hour.

## CHAPTER V

### RESULTS

#### V.1 The Samples

All samples were condensed into the sample cell as liquids which were then cooled. The cooling process was, however, very slow due to the limited thermal contact between the cell and the variable temperature insert. Some control of the rate was exercised by varying the pressure of helium gas in the insert vessel. Most samples required three to four hours to cool from near  $T = 95$  K to just below the triple point at  $T = 90$  K.

The slow solidification was ideal for the growth of large solid methane crystals, a factor noted in other studies<sup>29,32,34</sup>. The ideal sample for neutron total cross-section experiments would be polycrystalline, but it was not attainable. Some attempts to locate Bragg reflections from several samples of both  $\text{CH}_4$  and  $\text{CH}_3\text{D}$ , using neutron diffraction, were not successful. These results indicated that the sample consisted of a few crystals with no major crystal axes coinciding with the cryostat axis. The cryostat design made reorientation of the sample impossible. In one instance, the sample was condensed directly as a



solid, at  $T = 85$  K, and for a brief period Bragg reflections, characteristic of an oriented polycrystal, were found. During the course of the diffraction experiment, however, the sample appeared to recrystallize and the reflections disappeared.

An advantage of slow cooling and solidification was that the solid specimen filled the cell completely just below the triple point. This was important for fixing the sample thickness, - a parameter that was essential for the computation of the total cross-section.

## V.2 Calculation of Neutron Total Cross-sections

The total cross-section of a molecule ( $\sigma$ ) is related to the experimentally observable neutron transmission of a sample  $\frac{T}{T_0}$  by a simple equation,

$$\frac{T}{T_0} = \exp(-Nt\sigma). \quad [17]$$

In order to evaluate the cross-section, the molecular density, the number of molecules per  $\text{cm}^3$  ( $N$ ), and the sample thickness ( $t$ ) must be known.

The molecular densities, as a function of temperature, were determined from a number of experimental sources. The data available for  $\text{CH}_4$  and  $\text{CD}_4$  were fairly comprehensive, but none existed for  $\text{CH}_3\text{D}$  or  $\text{CH}_2\text{D}_2$ . Accurate estimates of the temperature dependence of the molar volume of  $\text{CH}_4$  were obtained from an X-ray diffraction study of the lattice

parameter between  $T = 2.5$  K and the triple point<sup>32</sup>. They were checked with data from other experimental sources<sup>29,33,101,102,103</sup>. Molar volumes of  $\text{CH}_4$  in the liquid were obtained from a study employing a pycnometric method<sup>104</sup>. The discontinuity in the molar volume at the triple point, inferred from the juncture of the solid and liquid molar volume data, was checked through the use of the Clausius-Clapeyron equation. The limiting slope of the melting curve at zero pressure was obtained from the data of Prydz and Goodwin<sup>105</sup>, while the entropy of fusion was obtained from the work of Colwell et al<sup>48</sup>. The two independent estimates of the discontinuity yielded the same value;  $-2.7 \text{ cm}^3$ . A composite curve for the molar volume as a function of temperature is shown in Figure 15.

A similar procedure was followed for  $\text{CD}_4$ , although no single comprehensive study of the lattice parameter, or of the molar volume has been published. The results of two separate X-ray investigations, one over the temperature range of 4.2 K to 50 K<sup>106</sup> and the other from 10 K to 70 K<sup>107</sup>, were used. In addition to these data, molar volumes from other X-ray and neutron diffraction studies of  $\text{CD}_4$ , usually at a few isolated temperatures, were also used<sup>34,35,108</sup>. The magnitude of the discontinuity in the molar volume at the transition between phase II and phase III, obtained from the X-ray studies, was consistent with the estimate of the tetragonal lattice distortion made from some optical birefringence

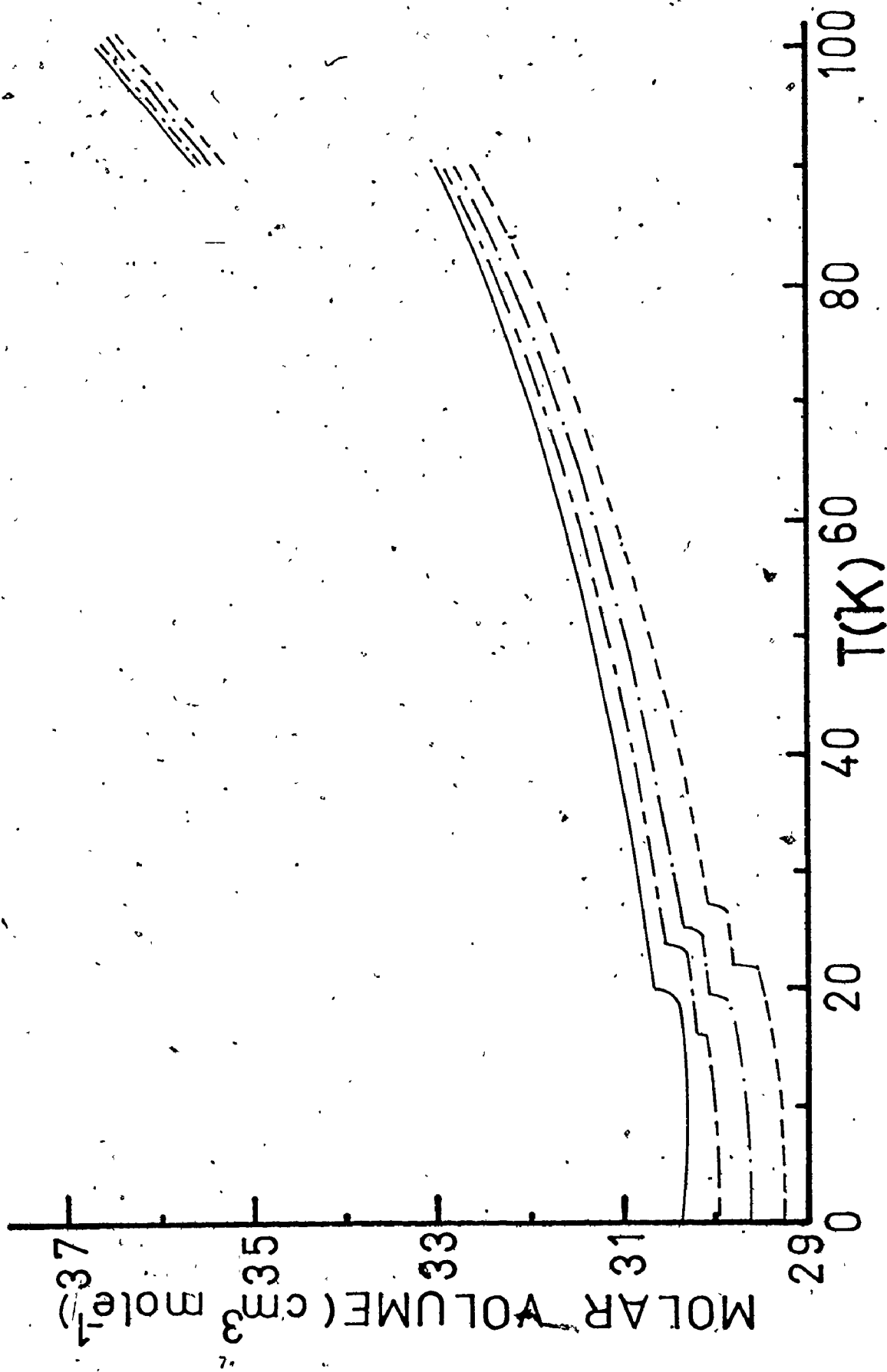
Figure 15. The Molar Volumes of the Methanes

— CH<sub>4</sub>

--- CH<sub>3</sub>D

— · — CH<sub>2</sub>D<sub>2</sub>

- · - · - CD<sub>4</sub>



measurements<sup>40</sup>.

The molar volume of liquid  $CD_4$  was estimated from the results of comparative studies of the molar volumes of  $CH_4$  and  $CD_4$ <sup>109,110</sup>. The molar volume of  $CD_4$  as a function of temperature is also shown in Figure 15. The curves for  $CH_4$  and  $CD_4$  are very similar, although  $CH_4$  does not transform into phase III. It is important to note that the  $CD_4$  curve lies below the  $CH_4$  curve.

Experimental<sup>109,110,111</sup> and theoretical studies<sup>112</sup> of condensed  $CH_4$  and  $CD_4$  have indicated that the change in molar volume upon deuteration is due primarily to a change in the intermolecular potential, coupled with a relatively minor translational quantum effect. The potential is altered because deuteration shortens the C-D bond length, making the molecule physically smaller. The molar volume of  $CH_3D$  should lie between those for  $CH_4$  and  $CD_4$ . This is supported by some early fragmentary data published by Clusius<sup>114</sup>. Some additional information was available. Optical birefringence data<sup>40</sup> indicated that the magnitude of the volume discontinuity at the phase II to III transition in  $CH_3D$  was about half that for  $CD_4$ . The volume change between phase I and II was very similar for both  $CH_4$  and  $CD_4$ , and the estimated entropies of the transition were also close<sup>48</sup>. From these data, the behaviour of  $CH_3D$  near the two solid-solid phase transitions was estimated.

The differences in the molar volumes for the isotopic methanes reflect the differences in intermolecular potential due to deuteration and to the differences in the mean squared displacement of the molecules from their equilibrium positions. Both of these factors bear, either directly or indirectly, some inverse relationship to the mass of the molecule. In lieu of a more concrete experimental or theoretical prediction for the behaviour of the molar volume of  $\text{CH}_3\text{D}$ , the curve was simply scaled, by an inverse mass relationship, between the two known curves. Any errors incurred in this procedure would primarily affect the absolute cross-section values of  $\text{CH}_3\text{D}$ , but, as the goal of the experiment was to examine relative changes, they were not important. In phase III, the region of greatest interest, the molar volume has little dependence on temperature, and thus has a negligible effect on the temperature dependence of the neutron cross-section values. A similar procedure was followed to establish the molar volume of  $\text{CH}_2\text{D}_2$ . The curves for  $\text{CH}_3\text{D}$  and  $\text{CH}_2\text{D}_2$  are shown in Figure 15.

Once the molar volumes for the various methanes were known, a temperature dependent correction for the sample thickness was derived. In the solid, the thickness was assumed to decrease as the cube root of the molar volume; the dimensionless factor  $\left(\frac{V_m(T)}{V_m(T.P.)}\right)^{1/3}$  was used as the scaling parameter, where the molar volume has been

normalised to the value at the triple point. Given the molecular density, readily derivable from the molar volumes, and the sample thickness, the conversion of the neutron transmission data to neutron total cross-sections was straightforward.

### V.3 Error Analysis

Random errors in the experiment arose from two sources: the neutron counting and the temperature control. Neutron counting errors were minimised by using large total counts (usually in excess of 100,000), and by repeating the count sequence many times at the same temperature. Averages were taken and the standard deviation of each set was used as an estimate of the error. The effects of fluctuations in the sample temperature during the experiments were more difficult to assess. The magnitude of the random error in any value of the cross-section was found by substituting the known count and the estimated temperature errors into an error equation derived by a Taylor series expansion of equation [17]. The temperature derivatives of the molecular density and the sample thickness were evaluated by taking the analytic derivative of the power series expansions of the two parameters.

The systematic errors can be divided into two groups depending upon whether or not they remained constant during the experiment. The constant terms affect only the absolute values of the cross-sections and not the relative values.

As a consequence, these sources of error were minimised where possible, but no effort was made to remove all of them. The results were not, for example, corrected for neutron absorption, nor for the finite solid angle subtended by the neutron counter, a factor which affects the sensitivity. The counter dead time was considered and shown to be insignificant at the low counting rates ( $\approx 2000 \text{ c.s.}^{-1}$ ) used: the pulse width was  $3.5 \mu\text{s}$ , and the probability of two counts occurring within this time interval was negligible. The cell thickness and empty cell transmission were both accurately measured to minimise possible errors from these two sources. There were, however, several sources of error that did not remain constant during the experiment. Their effects were reduced wherever possible. Fluctuations in the neutron flux were well compensated for by the in-beam monitor system. One other source of error, peculiar to the apparatus, arose because some rigidity in the cell mounting had to be sacrificed to improve thermal isolation; the cell was able to move small distances of the magnitude of 1 to 2 mm. The movement was, however, always discontinuous, occurring, for example, during the filling of the helium-4 reservoir, and could thus be recognised easily.

An effort was made to establish an accurate temperature scale over the entire temperature range examined experimentally. Below  $T = 4 \text{ K}$ , the carbon resistance thermometer was calibrated against a previously calibrated



germanium resistance thermometer<sup>53</sup> and the equilibrium vapour pressure of helium-3<sup>114</sup>. The reliability of the scale in this region was very high. Above  $T = 4$  K, the temperature scale was established by two gold-iron vs chromel thermocouples (1 and 2 in Table IV), one of which had been calibrated by Oxford Instruments. The second thermocouple, which was attached to the cell, was calibrated against the first. Both thermocouples were referenced to the stable helium-4 bath temperature. The maximum possible error in the temperature scale between 4 K and 77 K was estimated to be less than 0.1 K. When the cryostat was used above  $T = 77$  K, liquid nitrogen was placed in the helium-4 reservoir and the thermocouples were then referenced to the boiling point of nitrogen, - a less reliable standard. The error in the temperature scale for the region could have been as large as 1 K.

Two other factors affected the precision of the relative cross-section data. The first was the presence of isotopic impurities in the deuterated methanes. The substantial amount of  $\text{CH}_4$  present as an impurity in  $\text{CH}_3\text{D}$  required that a correction be made. The single particle nature of the incoherent neutron scattering made the correction quite easy: a scaled fraction of the neutron cross-section for pure  $\text{CH}_4$  could be subtracted from the  $\text{CH}_3\text{D}$  data. The second factor concerned the samples themselves. Some of the observed scatter could not be ascribed to instrumental defects, temperature stability or counting statistics. Thermal

history effects and long equilibration times in the solid methanes sometimes increased the apparent scatter of the data. Their exact nature will be described more fully in later sections.

#### V.4 CH<sub>4</sub>

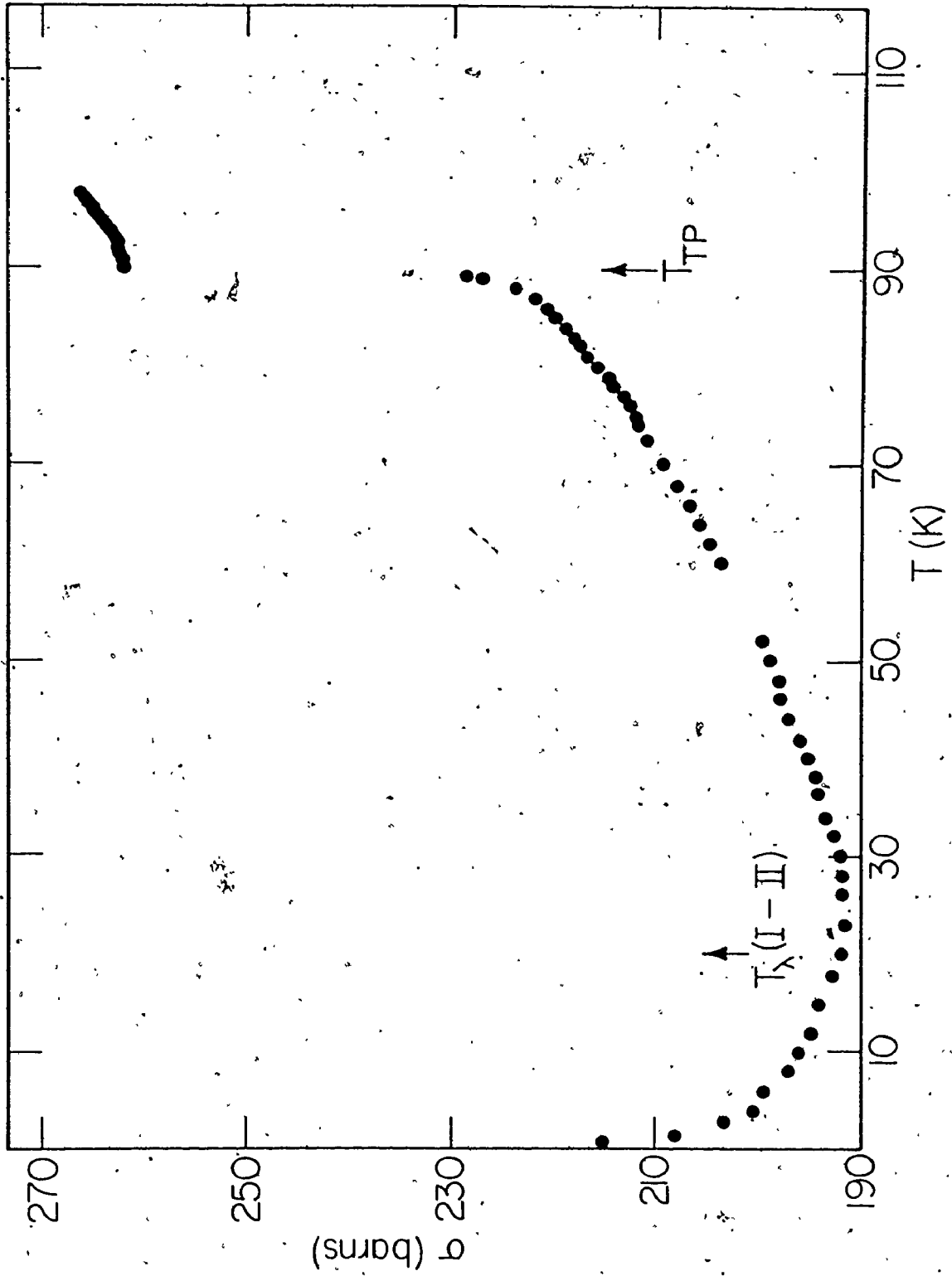
The data for both the pure methane and the oxygen-doped samples contain information about the equilibrium behaviour of the methane system in relation to the various spin species, and about the kinetics of the conversion process.

An unexpected benefit of the limited heat exchange between the sample and the variable temperature insert was that fairly accurate, total cross-section values could be measured as the sample cooled. These data were collected from two partially overlapping sets of data, one with liquid nitrogen in the reservoir ( $T = 100 \text{ K}$  to  $T = 85 \text{ K}$ ), and the second with liquid helium ( $T = 88 \text{ K}$  to  $T = 20 \text{ K}$ ). The neutron counting sequence was started once the sample was liquefied and the cooling had begun. A record of the time dependence of the sample temperature was kept to enable the series of neutron counts to be related to the sample temperatures; the cooling rate was slow enough so that a linear interpolation of the temperature between the reference points introduced no significant errors. Within each linear region, the neutron count data were subdivided into appropriate segments and averaged. The average values, along with the

interpolated temperature, were used to calculate total cross-section values as a function of temperature. The results for one continuous cooling experiment, between  $T = 100$  K and  $T = 25$  K, are shown in Figure 16. Below about  $T = 25$  K, neutron cross-sections had to be determined at constant temperatures. The results of these more precise measurements of the cross-section are also included in Figure 16 to give a complete overview of the temperature dependence of the equilibrium neutron total cross-section.

Above  $T \approx 25$  K, the results for the pure and oxygen-doped samples were very similar, but, below that temperature, differences appeared which can be ascribed to differences in the amount of spin conversion that occurred in the specimen. Recent n.m.r. measurements<sup>60</sup> and low temperature heat capacity data<sup>49</sup> had shown that substantial amounts of oxygen impurity in methane allowed spin species conversion to reach completion rapidly. Thus, the oxygen-doped sample was examined first to obtain the equilibrium behaviour of the cross-section. The sample was cooled slowly ( $1 \text{ K hr}^{-1}$ ) from near the triple point to just below the phase transition ( $T = 20.4$  K). At this point, the sample temperature was closely controlled for about one hour, while the neutron transmission of the sample was measured. The data were collected at one degree intervals down to  $T = 4.2$  K. Following this initial cooling, many other data points were determined, all within phase II, down to  $T = 0.75$  K which

Figure 16. The Total Neutron Cross-section of CH<sub>4</sub>



was reached with the helium-3 refrigeration stage. Finally, prior to being removed, the sample was warmed slowly through the transition region. The composite data are shown in Figure 17, which is a plot of neutron total cross-section against the logarithm of the temperature.

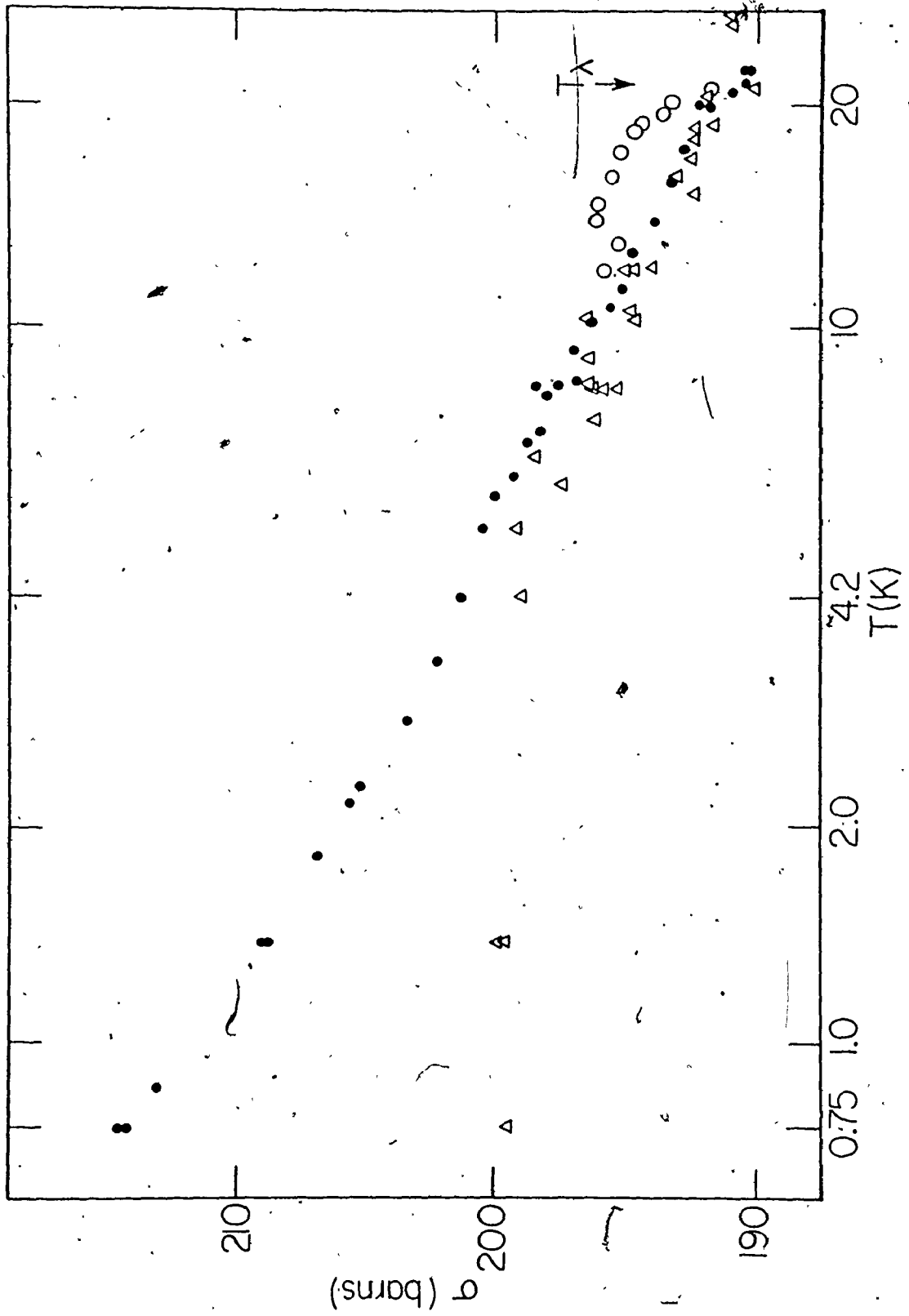
The data for pure methane were, as was expected,<sup>17,49,53</sup> complicated by time dependent effects associated with spin species conversion. The cross-sections for pure methane given in Figure 17 represent pseudo-equilibrium. At each temperature, the neutron transmission was followed until no further changes with time could be detected. Usually, this took three to four hours. When the system seemed to be at equilibrium, the neutron cross-section was determined. To compare the two methane samples, the cross-sections were normalised in phase I at  $T = 22.5$  K.

The kinetics of spin conversion were studied in the following manner. The sample was allowed to stand at a given temperature long enough so that the lattice was in thermal equilibrium. The cell temperature was then changed rapidly, either by heating or cooling, and the change in the sample's neutron transmission was followed for periods of as long as sixteen hours. The conversion process was assumed to follow first order kinetics, and the following integrated rate equation was used:

$$C(t) = C_{\infty} + (C_0 - C_{\infty}) \exp(-t/\tau) \quad [18]$$

Figure 17. The low temperature total neutron cross-sections for CH<sub>4</sub>

- oxygen-doped (0.66 mol%) sample
- Δ pure sample
- results from the initial cooling of the oxygen-doped sample





Here,  $C_0$  and  $C_\infty$  are respectively the initial and final values of the neutron count, and  $\tau$  is the characteristic lifetime of the process.

There were several experimental limitations in the kinetics measurements: (i) the change ( $C_\infty - C_0$ ) had to be several times larger than the statistical error in the neutron counting ( $N^{1/2}$ ); (ii) the time required to change the temperature had to be much less than  $\tau$ ; (iii)  $\tau$  had to be at least as large as the time taken for one counting interval.

Conversion in the oxygen-doped sample was found to be rapid. The majority of the experiments were, therefore, limited to the temperature region  $1.4 \text{ K} < T < 4.2 \text{ K}$  within which the temperature could be changed sufficiently rapidly. The data were fitted to equation [18] by a non-linear least squares method. Both a grid search and a gradient expansion method<sup>115</sup> were used to determine the unknown parameters. The conversion lifetimes derived from the curve fits are given in Table V. Where more than one experiment was performed, the standard deviation for the data is given.

Conversion kinetics in the pure methane sample turned out to be more complex. The data were also analysed by a non-linear least squares method according to equation [18], but only the grid search method was employed because it was computationally faster. The estimates of lifetimes for conversion for a variety of temperature changes are shown in Table VI. They are obviously temperature dependent,

TABLE V  
Conversion Kinetics in CH<sub>4</sub>-Oxygen Doped Sample

Temperature Change (K)	Number of Experiments	Estimated Lifetimes for Spin Conversion (sec)
1.4 to 4.2	5	120±40
4.2 to 1.4	4	250±60
2.0 to 0.76	2	310±30
4.2 to 2.6	1	90
6.5 to 4.2	1	190
8.0 to 4.2	1	240
19.0 to 4.2	1	330

TABLE VI

Conversion Kinetics in CH<sub>4</sub>-Pure Sample

Temperature Change (K)	Number of Experiments	Estimated Lifetimes for Spin Conversion (sec)
4.2 to 1.4	4	270,000 (±80,000)
6.0 to 4.2	1	3,100
8.2 to 4.2	4	6,900 (±2,000)
11.2 to 4.2	1	21,000
11.9 to 4.2	1	13,000
12.0 to 4.2	1	2,100
16.0 to 4.2	1	17,500
20.0 to 4.2	1	2,400
22.0 to 4.2	1	1,000
4.2 to 8.2	4	1,600 (±1,000)
8.2 to 10.2	1	600
4.2 to 16.3	1	1,000
4.2 to 20.0	1	100

which had some ramifications on the experimental method and analysis. For example, this introduced an asymmetry into the determination of  $\tau$  from heating and cooling experiments.

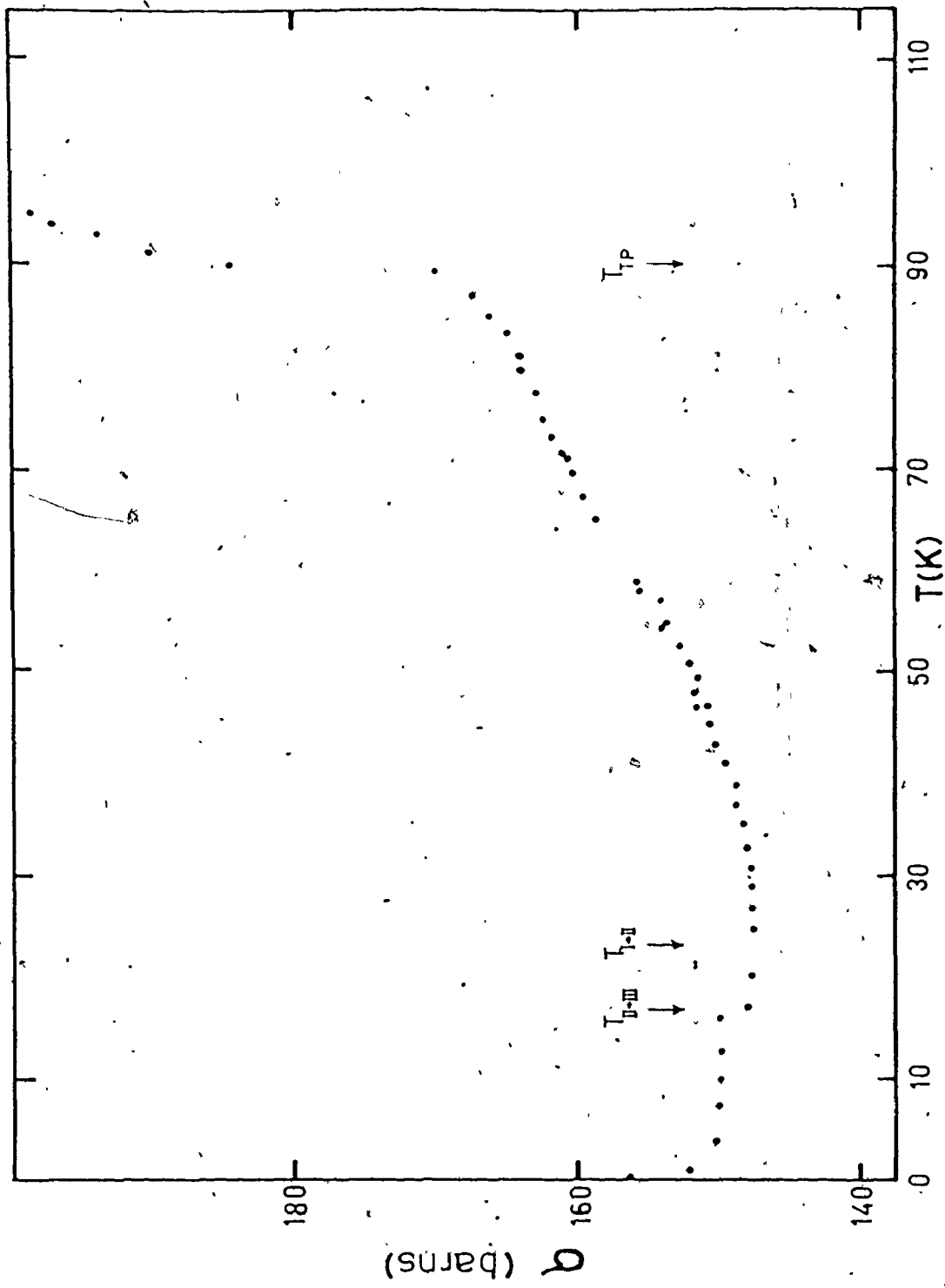
At temperatures below 4.2 K, no obvious time effects were observed for the pure methane over a period of several hours, yet the values of the cross-section were clearly well below those corresponding to equilibrium (see Figure 17). To obtain an estimate of the rate of conversion, the sample was equilibrated at  $T = 4.2$  K for a period of 12 to 20 hours, and then its temperature was reduced rapidly to 1.4 K and maintained there for up to 16 hours. The data were analysed with a gradient-expansion, non-linear, least squares method, and the best values for the parameters in equation [18] were found. The experiment was repeated four times and the results are given in Table VI.

#### V.5 $\text{CH}_3\text{D}$

The majority of the data for  $\text{CH}_3\text{D}$  were collected from experiments on a pure sample. A few experiments were performed on an oxygen-doped sample.

Figure 18 gives an overview of the temperature dependence of the cross-section for  $\text{CH}_3\text{D}$ . Results for the region  $T > 26$  K were obtained during continuous cooling, as in the example of  $\text{CH}_4$ . Below  $T = 26$  K, the sample temperature was reduced in one degree steps, and the neutron transmission data were collected at each temperature for at least a

Figure 18. The Total Neutron Cross-Section of CH<sub>3</sub>D



hour. Because some non-reproducible effects appeared in the regions of the transitions, the sample was kept at  $T=22$  K, just below the I to II phase transition, overnight to allow it to anneal. At the lower transition, the sample was cooled slowly and annealed for approximately twelve hours.

Extensive cross-section measurements were made between  $T = 0.75$  K and  $T = 16$  K for the solid in phase III. The data were collected over periods of one to three hours for each determination, with the sample temperature controlled to better than  $\pm 0.01$  K. Additional cross-section values for phase II of  $\text{CH}_3\text{D}$  were obtained as the sample was warmed up at the conclusion of the experiments.

In contrast to the example of  $\text{CH}_4$ , no dependence of the cross-section upon oxygen content was found for  $\text{CH}_3\text{D}$ . This is illustrated in Figure 19 where the results for the pure and oxygen-doped specimens are plotted. An effect of oxygen was, however, found on the rates of conversion, as is summarised in Table VII. Because of the experimental limitations mentioned earlier, it was only practicable to study the kinetics in the region  $1.4 \text{ K} < T < 4.2 \text{ K}$ . For the oxygen-doped sample, however, the measurements were only possible after the reactor flux was increased, by a factor of three, for the duration of the experiment.

#### V.6 $\text{CH}_2\text{D}_2$

It would have been desirable to use a larger cell for the experiments on  $\text{CH}_2\text{D}_2$  to compensate for the small

Figure 19. The low temperature total neutron cross-section of  $\text{CH}_3\text{D}$ .



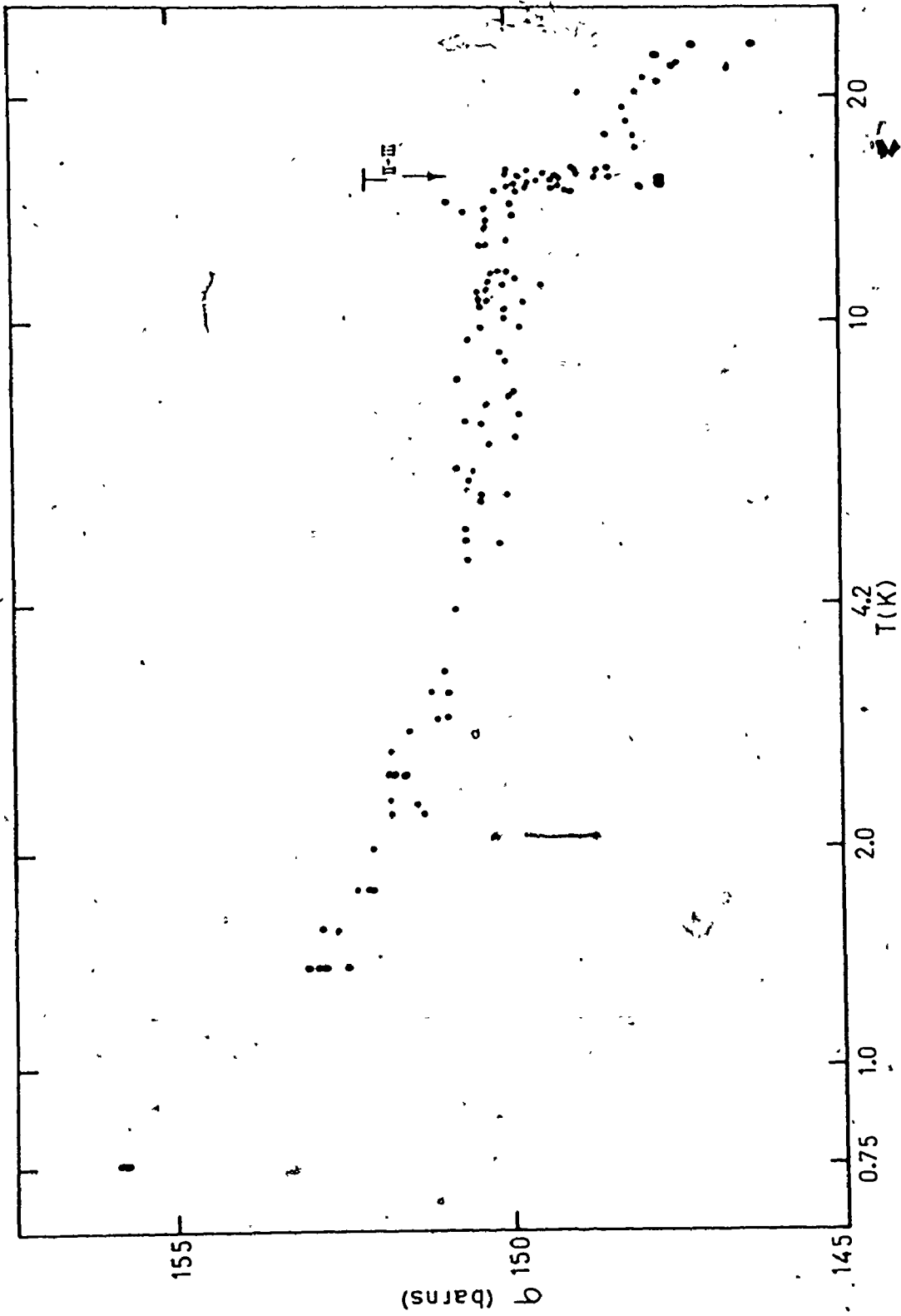


TABLE VII

Conversion Kinetics in CH<sub>3</sub>D

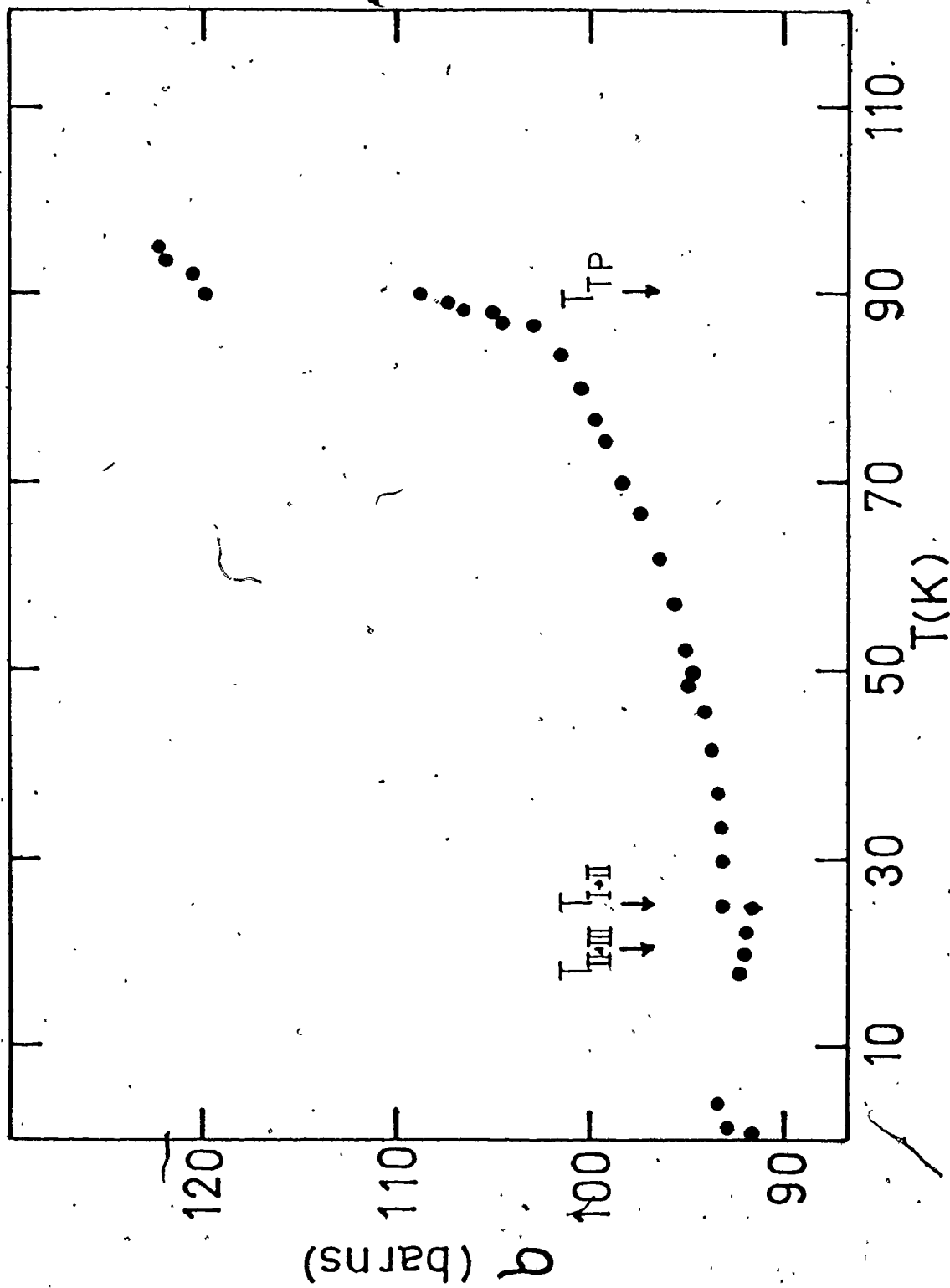
Sample	Temperature Change (K)	Number of Experiments	Estimated Lifetimes for Spin Conversion (sec)
CH <sub>3</sub> D/O <sub>2</sub>	1.4 to 4.2	4	30±15
CH <sub>3</sub> D	1.4 to 4.2	4	130±50
	4.2 to 1.4	5	180±35

number of protons per molecule. This would have entailed extensive reconstruction of the system, and it was thought not to be essential, even though the cross-section measurements would be somewhat restricted by the low level of neutron scattering from the CH<sub>2</sub>D<sub>2</sub> sample.

The same cooling procedure was used, - continuous cooling to the region of the upper transition and annealing in the regions just below the transition temperatures. The temperature dependence of the neutron cross-section is shown in Figures 20 and 21. The general trend is the same as that for CH<sub>4</sub> and CH<sub>3</sub>D except at the lowest temperatures (T < 4.2 K)

As will be discussed in the next chapter, the decrease in  $\sigma$  with decreasing temperature for T < 4.2 K is most probably associated with spin conversion. It was not practicable, however, to study the kinetics of the conversion process because the change in neutron transmission was so small.

Figure 20. The Total Neutron Cross-sections of  $\text{CH}_2\text{D}_2$



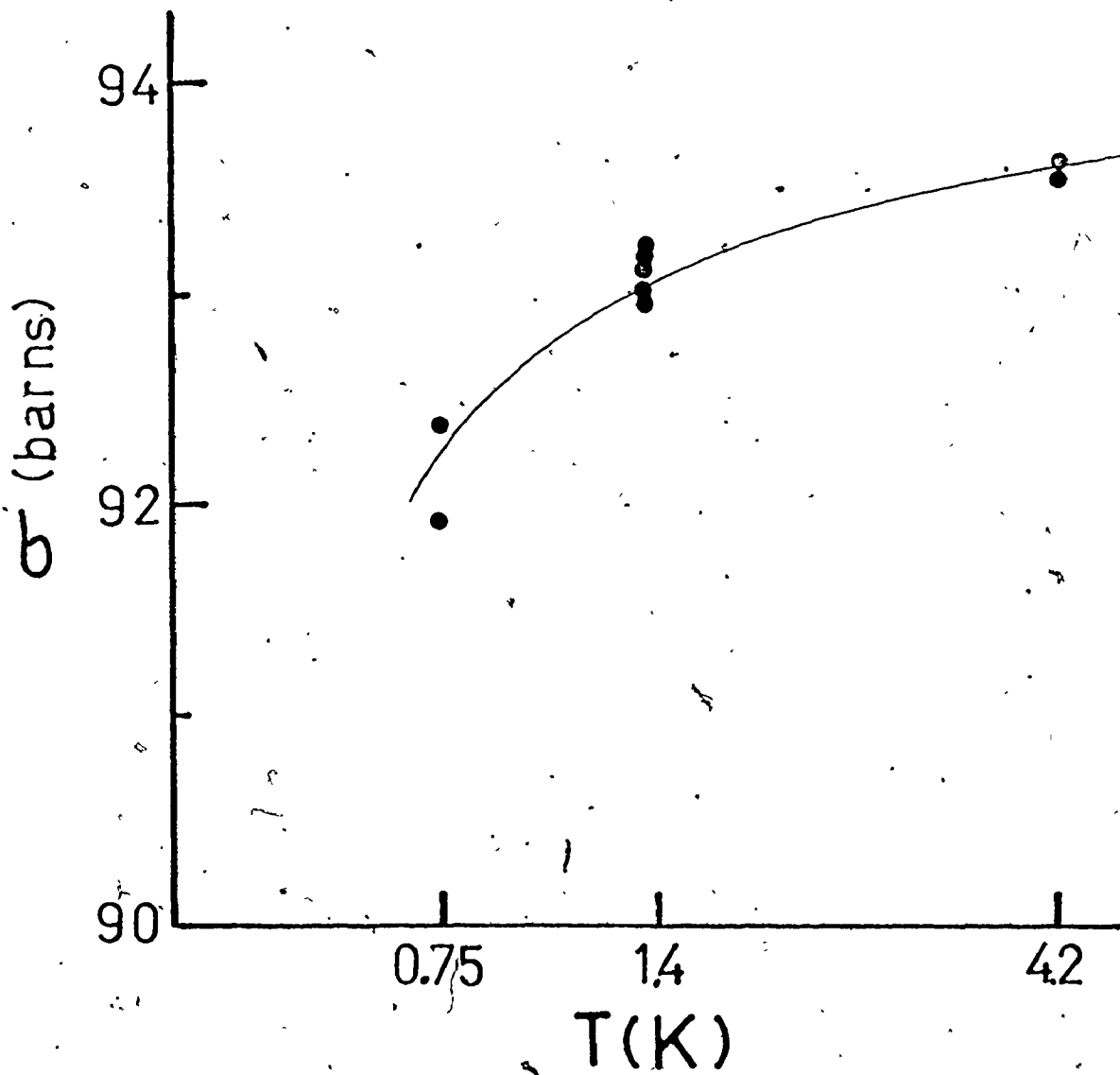


Figure 21. The Low Temperature Total Neutron Cross-section of  $\text{CH}_2\text{D}_2$

## CHAPTER VI

### DISCUSSION

The purpose of the experiments on  $\text{CH}_4$  was somewhat different from that for  $\text{CH}_3\text{D}$  or  $\text{CH}_2\text{D}_2$ . From the outset, the existence and extent of spin species conversion in  $\text{CH}_4$  was well documented. Nevertheless, the measurement of the neutron total cross-sections of  $\text{CH}_4$  could aim to accomplish several things. Although the n.m.r. study of Code and Higinbotham<sup>17</sup> concluded that spin conversion in phase II of  $\text{CH}_4$  proceeded differently on the ordered and disordered sublattices, no single experiment had examined solid  $\text{CH}_4$ , both pure and with a known large oxygen content. Thus, the neutron scattering experiment on two such samples was undertaken to confirm the effect of the sublattice structure on the spin conversion process. At the same time, the independent experiment would test for any systematic errors in the n.m.r. observations. In addition, the neutron experiment yields information about the kinetics of the conversion process that could not be obtained from n.m.r. experiments without excessive difficulty. The role of the neutron scattering experiments on  $\text{CH}_4$  was, therefore, to elaborate upon and to confirm existing concepts, while, for  $\text{CH}_3\text{D}$  and  $\text{CH}_2\text{D}_2$ , the experiments were of an exploratory nature.

to attempt to define the role of spin species conversion in the low temperature behaviour of these solids.

At higher temperatures, where the concentrations of the spin species become constant, the behaviour of the different solid isotopic methanes becomes rather similar and it is convenient, in this region, to discuss the data for all of the methanes together (section VI.2).

#### VI.1 Crystal Form and Impurity Content

The attempts to detect neutron diffraction from the samples (section V.1) indicated that the solidification procedure produced large grained crystals. This behaviour is similar to that noted elsewhere in several X-ray and neutron diffraction studies<sup>29,32,34</sup>. It is reasonable to assume that large grained samples have occurred in many other experiments where a slow solidification procedure was followed<sup>17</sup>. Polycrystalline samples have probably only been obtained when methane has been rapidly solidified at low temperatures ( $T < 40$  K) from the gas<sup>29</sup> or liquid. The presence of oriented crystals does not, however, affect the predominantly incoherent neutron scattering from a methane sample, because the scattering is of a single particle nature, and independent of sample orientation<sup>81</sup>. On the other hand, in n.m.r. experiments, oriented crystals, coupled with the defined magnetic field axis, could lead to unexpected results.

To examine the effects of strategic impurities, such as oxygen, it is obviously desirable to perform experiments

on samples of uniform composition. Such samples are unlikely to be attained except under specifically controlled experimental conditions. In the present experiments, the technique of sample handling and crystal growth was such that significant segregation of the oxygen was unlikely, except possibly during the slow freezing step. Since the solid was subsequently cooled very slowly, some homogenisation of the composition ought to have occurred by diffusion.

A greater amount of segregation would be expected in other experiments, for example, n.m.r.<sup>17</sup> and calorimetric<sup>52</sup>, in which the condensed specimen occupied only a small fraction of the total container volume. In such circumstances, it would be important to condense and to cool the sample extremely rapidly to prevent attainment of phase equilibrium.

## VI.2 Phase I

In phase I, the cross-section results for the three methane isotopes are very similar, which is not unexpected because, in this phase, the octahedral crystal field dominates the behaviour, and no effects directly associated with the spin species should be observable<sup>16</sup>. The results therefore contain information about the rotational and translational freedom of motion of the molecules. A plot of the total cross-section per proton against temperature for the three methane isotopes studied is shown in Figure 22. The data are normalised at  $T = 96$  K to facilitate comparison. The similarity of the three curves is striking. The large discontinuity



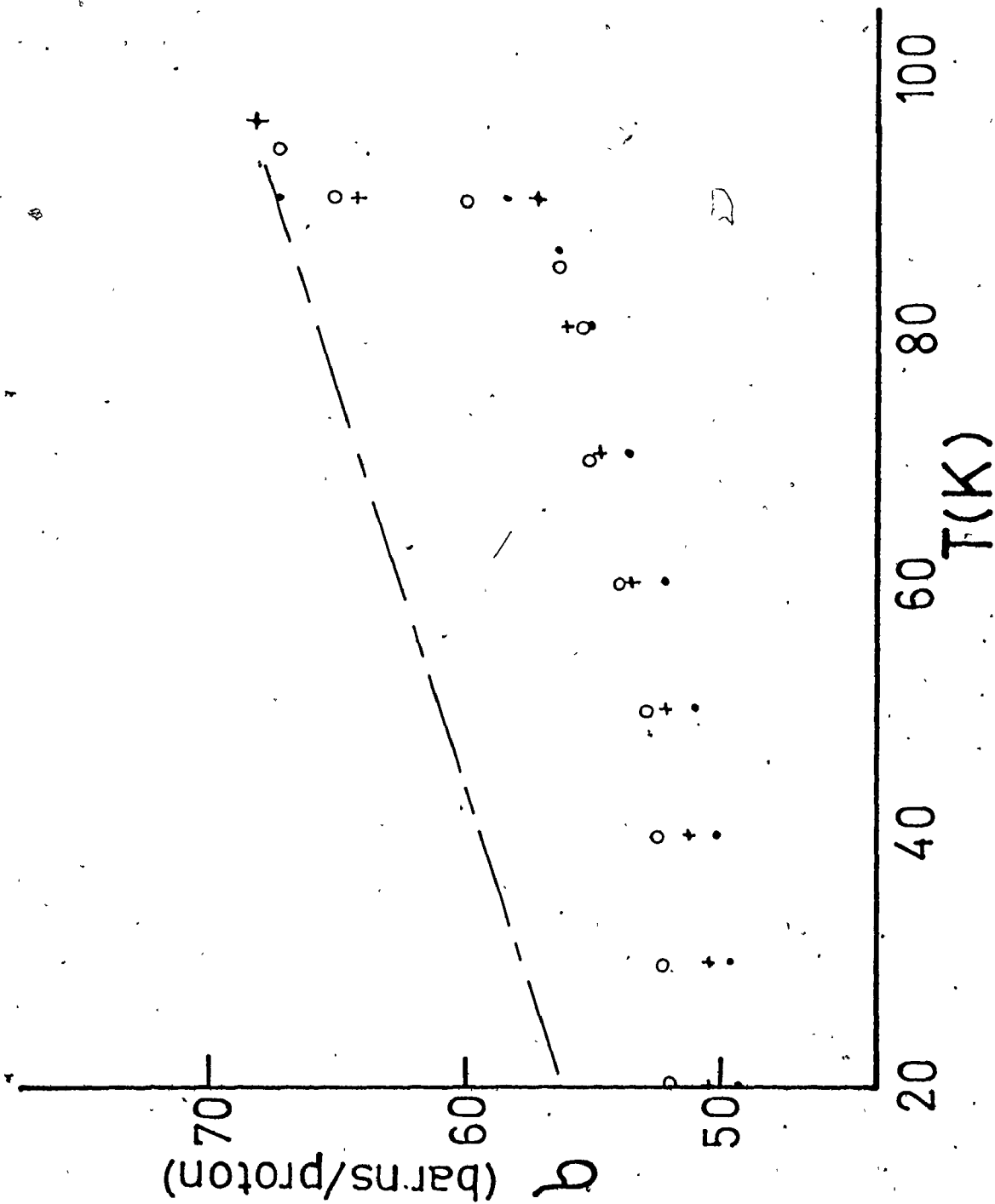
Figure 22. The cross-section per proton, for the three methanes studied in phase I.

● CH<sub>4</sub>

+ CH<sub>3</sub>D

○ CH<sub>2</sub>D<sub>2</sub>

— Krieger Nelkin calculation



at the triple point ( $T \approx 90$  K) reflects the decrease in the freedom of rotational and translational motions of the molecules on solidification. Evidence from other experimental studies indicates that there is only a relatively small change in rotational freedom at the melting point. The entropy of fusion is low<sup>48,92</sup>, and is characteristic of a plastic crystalline phase in which melting primarily involves the loss of the translational order of the crystal. Other techniques have indicated that, near the triple point, the rotational motion of the methane molecules is nearly free<sup>117</sup>. If the change in translational motion is the primary cause of the discontinuity in the cross-section, then the change in the cross-section is probably associated with a decreased density of low energy translational states in the solid, which in turn reduces the number of possible inelastic scattering processes. The magnitude of the decrease in cross-section at the triple point is the same, within experimental error, for all three methanes. Similar discontinuities in neutron total cross-section have been observed in other molecular solids at their triple points<sup>118,119</sup>, and in ammonium iodide at a first order phase transition ( $T=263$  K) in which the  $\text{NH}_4^+$  ion goes from a severely limited rotor to a nearly free rotor<sup>86</sup>.

Between the triple point and  $T=50$  K,  $\sigma$  decreases almost linearly with decreasing temperature. This behaviour is characteristic of the cross-section for a free rotor in

which the possible number of energy gain processes becomes increasingly restricted as excited states depopulate. This is illustrated by a free rotor calculation, due to Krieger and Nelkin<sup>84</sup>, of the cross-section for methane; it is also shown in Figure 22. Below  $T = 50$  K, the slope of  $\sigma$  versus  $T$  begins to decrease until, in the region just above the phase I to II transition, it becomes essentially zero. Such behaviour of the cross-section is consistent with increased restriction of rotational motion, perhaps associated with the strengthening of orientational correlations<sup>35</sup>, which ultimately leads to long range orientational order on the ordered sublattices in phase II.

Another interesting aspect of the data shown in Figure 22 is the trend with increasing deuterium substitution of the methane. At the triple point, all three methanes exhibit similar behaviour, but at lower temperatures the  $\sigma$  versus  $T$  curves for the three isotopes have quite different slopes, with the most heavily deuterated methane having the lowest one. The observed differences are far outside the possible error in either the experiment or in the estimated molar volumes. The probable origin of the trend is suggested by an argument, based upon a quantum theory of corresponding states, to explain the trend observed in the upper transition temperature upon deuteration<sup>120</sup>. The transition temperatures are found to scale to a rotational temperature that is directly related to the moments of inertia of the molecules.

As the moment of inertia increases, the energy level spacings decrease, and so the rate of depopulation of the levels with temperature must also decrease. On this basis, it could be expected that the slope of the  $\sigma$  versus  $T$  curves would be less for the more highly deuterated methanes, as is observed.

The initial cross-section experiments on both  $\text{CH}_4$  and  $\text{CH}_3\text{D}$  suggested that the transition from phase I to II was second order; the cross-section appeared to go smoothly through the transition region. Other experiments have indicated that the transition has many second order attributes, such as critical fluctuations<sup>35</sup> and a large  $\lambda$ -type anomaly in the heat capacity<sup>19</sup>. When the cross-section was measured over small intervals of temperature, in the immediate vicinity of the transition, the true discontinuous nature of the transition became apparent. A slight increase in cross-section occurred when the methane began to transform into phase II and some hysteresis was evident. These observations are in accord with a number of existing results, for example, n.m.r.  $T_1$ <sup>121</sup>, lattice parameter<sup>32</sup> and heat capacity measurements<sup>48</sup>, which show the transition to be first order.

### VI.3 $\text{CH}_4$

#### 3.1 Confirmation of Code and Higinbotham's deductions.

Below  $T = 20$  K, the cross-section data for  $\text{CH}_4$  are significantly different from those for the other methanes. There is an obvious parallel between the cross-section values

for both the pure and oxygen-doped methane samples (Figure 17) and the calculated values of  $\langle I(I+1) \rangle$  characteristic of spin species conversion on all eight sublattices of phase II and of conversion just on the disordered sublattices (Figure 5). In fact, the correspondence is excellent, thus confirming the suggestion made by Code and Higinbotham<sup>17</sup> on the basis of their n.m.r. study of a pure CH<sub>4</sub> sample, that conversion is observed on only the disordered sublattices in most experiments performed on pure methane. If the sample contains a catalyst such as oxygen, then conversion occurs on all eight sublattices.

### 3.2 The Direct proportionality between $\sigma$ and $\langle I(I+1) \rangle$ , - a test of the theory.

The cross-section data contain the information necessary to perform a more quantitative interpretation of the temperature dependence of  $\langle I(I+1) \rangle$ . There are, however, some other possible inelastic processes that need to be examined to ensure that their effects do not obscure deductions about spin conversion.

Inelastic processes associated with rotational excitations are limited by the phase II structure and the low energy of the neutron (43 K). On the ordered sublattices, all inelastic scattering is associated with the tunneling levels because the librational states are depopulated at low temperatures and cannot be excited by the neutrons. Considerations of detailed balance indicate that, by  $T=0.7$  K, the inelastic processes will be reduced by about 30 per cent,

if the scattering function stays approximately constant over the phase II region. Similar arguments can be made for the disordered molecules, except that the change in inelastic processes will occur predominantly above  $T = 20$  K. The rotational inelastic contributions to the cross-section would therefore be expected to remain very nearly constant below  $T = 20$  K, with a possible decrease below about  $T = 1$  K when the tunnelling levels begin to depopulate. Inelastic scattering from the lattice is also possible where the incoherent inelastic scattering is proportional to the density of phonon states. This contribution should be small because the measurements were made well below the Debye temperature of solid methane ( $\theta_D \sim 75$  K).

To summarize, the fraction of the total cross-section due to inelastic processes is small and any change with temperature will also be small. Hence, for the subsequent analysis of the cross-section data, it is assumed that the cross-section, in the absence of spin conversion, is temperature independent below  $T = 20$  K.

The cross-section data for the oxygen-doped  $\text{CH}_4$  sample represent an equilibrium distribution of the three spin species on both the ordered and disordered sublattices. They can thus be used to determine the temperature dependence of  $\langle I(I+1) \rangle$  and to check the theoretical predictions for  $\langle I(I+1) \rangle$  as a function of temperature. At any temperature,  $\langle I(I+1) \rangle$  is given by;

$$\langle I(I+1) \rangle = 6.0 P_A + 3.0 P_T + 0 P_E \quad [19]$$

where  $P_A$ ,  $P_T$  and  $P_E$  are the populations of the A, T, and E spin species respectively. In phase II of  $\text{CH}_4$ , these populations can be calculated easily from a rotational partition function, constructed from the energy level scheme of Yamamoto et al,<sup>16</sup> which includes the temperature dependence of the tunnelling levels. Values of  $\langle I(I+1) \rangle$  were calculated as a function of temperature, and used to establish the unknown proportionality between  $\sigma$  and  $\langle I(I+1) \rangle$ . The best equation representing the linear relationship was found to be:

$$\sigma = 167.1 + 8.34 \langle I(I+1) \rangle \quad [20]$$

The quality of the fit to equation [20] can be seen in Table VIII, where the calculated values of  $\sigma$  agree with experiment within the probable experimental error. This result has two direct consequences: it confirms that the linear relationship between  $\sigma$  and  $\langle I(I+1) \rangle$  is valid at finite neutron wavelengths, and it demonstrates, once again, that Yamamoto's theoretical model of  $\text{CH}_4$  is a satisfactory one. The sensitivity of  $\langle I(I+1) \rangle$  to the temperature dependence of the tunnelling levels, predicted by Yamamoto et al, is small and just barely detectable in the experimental results.

Similarly, the cross-section data are not accurate enough to distinguish between the values of  $\langle I(I+1) \rangle$  calculated from the experimental tunnelling level splittings of Press and Kollmar<sup>97</sup> and the theoretical values of Yamamoto et al.<sup>16</sup>



TABLE VIII

Comparison of observed equilibrium neutron cross sections with cross-sections calculated from the theoretically predicted values of  $\langle I(I+1) \rangle$  due to Yamamoto et al. (1977).

T(K)	$\sigma$ (barns)		$\langle I(I+1) \rangle$
	obs.	calc.	
0.75	214.3	214.5	5.686
0.86	213.0	213.4	5.548
0.97	211.8	212.2	5.405
1.43	208.6	208.3	4.943
2.00	206.0	205.5	4.599
3.33	202.4	202.2	4.207
4.07	201.5	201.1	4.077
5.26	200.2	199.7	3.910
6.00	199.3	199.0	3.823
8.00	197.8	197.4	3.636
10.00	196.2	196.3	3.496
12.00	195.0	195.4	3.392
14.00	193.9	194.7	3.310
18.00	192.7	193.0	3.105

An inelastic neutron scattering experiment at very low temperatures is required to establish unambiguously whether or not dilation of the tunnelling levels occurs as a consequence of spin conversion to the A species.

### 3.3 Spin Conversion on the Disordered Sublattices of Phase II

The n.m.r. and neutron results agree that, in pure  $\text{CH}_4$ , spin conversion occurs only on the disordered sublattices (section 3.1). A quantitative comparison of the results from the two types of measurement can, however, be made by using equation [20] to calculate the values of  $\langle I(I+1) \rangle$  from the measured cross-sections. These values are shown in Table IX. The apparent limiting value for  $\langle I(I+1) \rangle$  at low temperatures of  $3.92 \pm 0.05$  is larger than the expected one:

$$\begin{aligned} \langle I(I+1) \rangle_{\text{low temp.}} &= \frac{3}{4} * 3.00 + \frac{1}{4} * 6.00 & [21] \\ &= 3.75, \end{aligned}$$

by an amount greater than the expected error. There are two possible causes for the difference. Spin conversion on the ordered sublattices of phase II could have raised  $\langle I(I+1) \rangle$  by a small amount, but an examination of the thermal history of the sample virtually ruled out this possibility. It is more probable that the limit is questionable, because spin conversion will have occurred in phase I at  $T = 20.4 \text{ K}$  and the distribution of spin species will no longer be the high

TABLE IX

Conversion on disordered sublattices of  $\text{CH}_4$   
 based on observed neutron cross-sections

T(K)	$\sigma$ (barns) $\pm 0.05^b$	$\langle I(I+1) \rangle^a$ $\pm 0.05$
0.75	199.8	3.92
1.38	199.8	3.92
4.2	199.0	3.82
6.0	198.0	3.71
8.0	196.1	3.48
10.0	195.6	3.42
12.0	194.8	3.32
14.0	194.3	3.26
18.0	192.9	3.10
20.0	192.8	3.10

<sup>a</sup> calculated using equation [20]

<sup>b</sup> error limits express the limits on the accuracy of the value due to normalization procedures

temperature one. Thus, at the phase transition, three quarters of the molecules become orientationally ordered and conversion times for these molecules become very long<sup>64</sup>. The corresponding value of  $\langle I(I+1) \rangle$  for these molecules must, however, be greater than 3.00. Its magnitude can be estimated. Although the energy levels have altered for the ordered molecules in phase II, their symmetry has not, and an upper limit of  $\langle I(I+1) \rangle = 3.5$  for these molecules is obtained by assuming that the spin species composition is frozen at the levels present in phase I just above the transition. A lower limit of  $\langle I(I+1) \rangle = 3.1$  is obtained if spin conversion in the transition region occurs and the newly formed ordered molecules reach true thermal equilibrium. The two estimates lead to

$$3.82 < \langle I(I+1) \rangle < 4.13.$$

low  
temp

The neutron result is comfortably between these limits.

Code and Higinbotham<sup>17</sup> give  $\langle I(I+1) \rangle = 3.67$  which is  
T=4.3K

based on  $\langle I(I+1) \rangle = 3.00$  at T = 45 K. In phase I, however,  $\langle I(I+1) \rangle$  is not at its high temperature limit even at T = 45 K and if an allowance is made for this, the neutron and n.m.r. experiments yield the same limiting value for  $\langle I(I+1) \rangle$

within their respective uncertainties.

low  
temp.

### 3.4 Anomalous cross-section results near the phase I to II transition.

When the oxygen-doped  $\text{CH}_4$  sample was first cooled into phase II, the neutron cross-section was found to be anomalously large (see Figure 17). An explanation is to be found in the results of the refined measurements of the lattice parameter in  $\text{CH}_4$  in the region of the I to II phase transition<sup>32</sup>. In particular, it was found that Bragg reflections characteristic of both phase I and phase II occurred simultaneously over quite a wide temperature range near the transition. This suggests that the transition occurs by a domain growth mechanism and so, if the sample were cooled rapidly through the transition, it is possible that a large fraction of the crystal could remain in a meta stable phase I-type structure well below the transition temperature. In this event, significant additional conversion would be expected to occur thus leading to values of  $\sigma$  larger than those corresponding to equilibrium. The anomalous cross-section results were reanalysed assuming that some fraction,  $\chi_I$ , of the crystal had remained in a phase I structure below the transition. The value of  $\chi_I$  at  $T = 14.8$  K was estimated through equation [20], and the theoretical values of  $\langle I(I+1) \rangle$  for phase I and phase II type structures, and found to be 0.41. This composition was then assumed to remain constant and the cross-section that would correspond to such a mixture, for  $14\text{K} < T < 20\text{K}$  were calculated. The results are displayed in Figure 23. The calculated

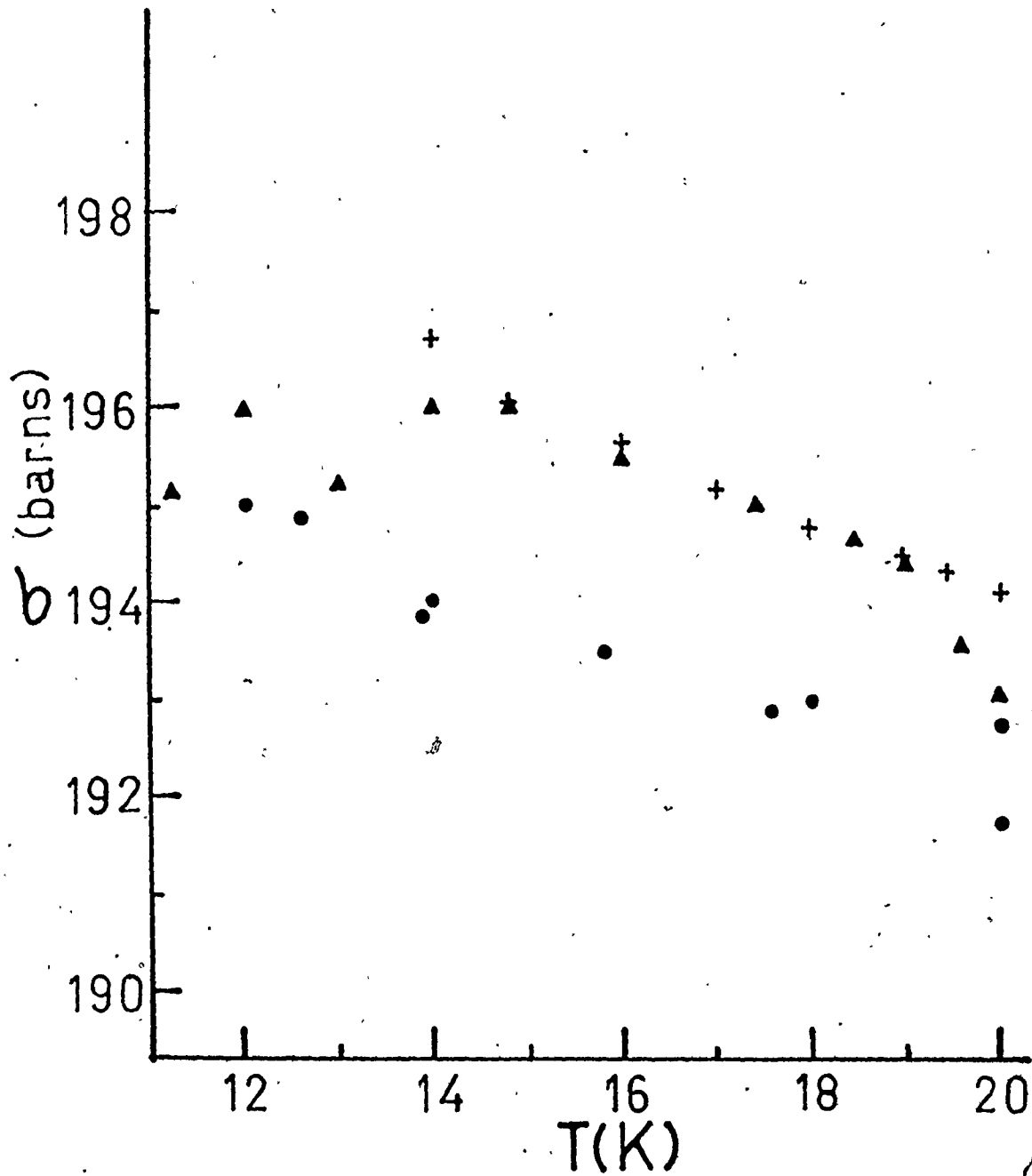


Figure 23. The anomalous cross-section results in  $\text{CH}_4$

- equilibrium cross-section
- ▲ anomalous results
- + calculated cross-sections

values of  $\sigma$  duplicate the observed ones well.

### 3.5 Kinetics of Conversion

The sensitivity of the neutron cross-sections to changes in  $\langle I(I+1) \rangle$ , clearly demonstrated by the equilibrium measurements, suggested that the kinetics of spin conversion could be studied with some precision. In all studies of the conversion process, the rate was assumed to obey first order kinetics, as there were no experimental or theoretical reasons for using a more complex rate equation.

The kinetics of spin conversion in oxygen-doped  $\text{CH}_4$  were examined first, primarily to ensure that equilibrium had been achieved in the experiments determining "equilibrium" cross-sections for  $\text{CH}_4$ . The conversion lifetimes found (Table V) agreed well with the more qualitative estimates, based on thermal relaxation rates, of Vogt and Pitzer<sup>49</sup> for a sample of similar composition. Spin conversion in the oxygen catalysed system is rapid, with the spin species concentrations coming to equilibrium within ten minutes, over most of the temperature range studied. Below  $T = 1.5$  K, thermal equilibrium of the sample appeared to require about thirty minutes to be attained, - an effect also noted by Vogt and Pitzer<sup>49</sup>. The conversion rate found above  $T = 1.5$  K is also consistent with the existing n.m.r.<sup>59</sup> and i.r.<sup>56</sup> evidence on the rate of spin conversion in oxygen-doped samples. The spread in the lifetimes given in Table V is probably the result of variations in the rate at which the sample tempera-

ture could be changed. The best results were obtained by warming the sample from  $T = 1.4$  K to 4.2 K, where the cell temperature could be changed within a few seconds.

The interpretation of the kinetics of conversion on the ordered sublattices of phase II in a "pure"  $\text{CH}_4$  sample is more complex because of the possible intrusion of the effects of traces of oxygen in the pure samples. The rate of conversion on the ordered sublattices was known to be very slow. In a n.m.r. study, Hopkins et al.<sup>59</sup> estimated the conversion time for their sample to be in excess of twenty four hours, while Code and Higginbotham<sup>17</sup> suggested their sample should reach equilibrium in about ten hours. The pure sample used in these cross-section experiments had a probable oxygen concentration of about 10 ppm.

The results of the long term experiments at  $T = 1.4$  K shown in Table VI, display large scatter because the conversion process could only be followed for a time that was only a fraction of a lifetime. The inaccuracies were minimised, however, because the limiting value of  $\sigma$ , at infinite time, was known from the experiments on oxygen-doped  $\text{CH}_4$ . The average lifetime found for conversion of the molecules on the ordered sublattices was 75 hours. Recent n.m.r. measurements on a similar methane sample have found the value for  $\tau$  of about 150 hours<sup>66</sup>. Lifetimes of this magnitude mean that it would take about a month for  $\text{CH}_4$  to reach spin species equilibrium. These estimates are much less than the theoret-

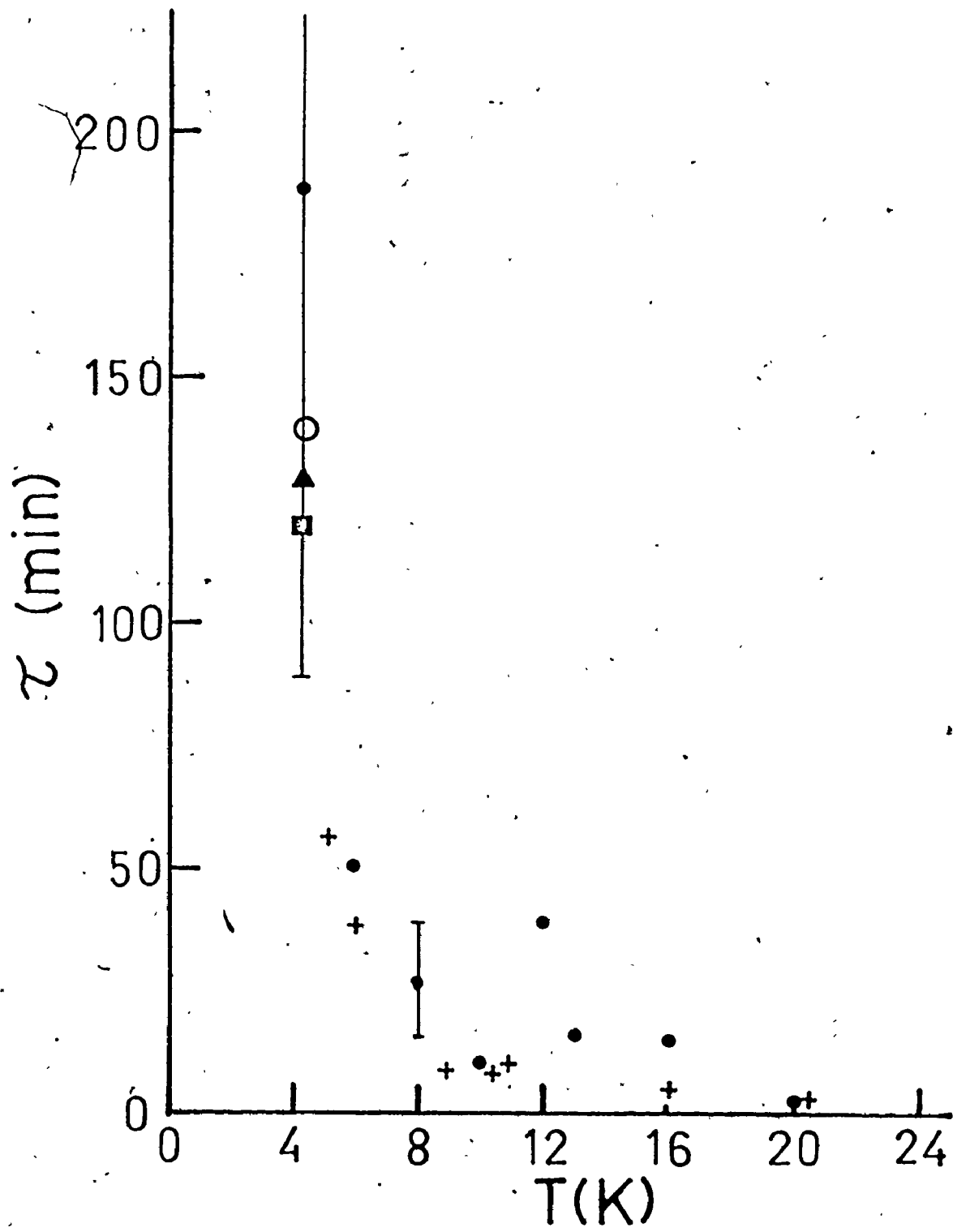


tical estimate<sup>64</sup> for  $\tau$  of about one year. The difference may be the result of the small oxygen concentrations in the experimental samples<sup>122</sup>. If that is true, the conversion should not follow strict first order kinetics, because the  $\text{CH}_4$  molecules in the immediate neighbourhood of the impurity would be expected to convert more rapidly. The conversion rate at longer times would then depend on whether or not spin diffusion could occur.

Above  $T = 4$  K, the conversion rate was found to be faster, and can be associated with the molecules on the disordered sublattices. The rate is temperature dependent (Table VI), as had been suggested by earlier n.m.r. data<sup>62</sup> and also by the heat capacity measurements of Vogt and Pitzer<sup>49</sup>. Before the results of the cross-section measurements are discussed in more detail, however, mention should be made of the temperature of the specimen, because the system could be heated much more rapidly than it could be cooled. For the kinetics experiments in which the sample was heated, the temperature at which the conversion process occurred was unambiguous. This was also the case for  $T < 16$  K where the sample could be cooled rapidly. At higher temperatures, however, the sample cooling was much slower, and the mean of the initial and final temperatures was a more appropriate estimate of the temperature at which conversion occurred. The conversion lifetimes, as a function of the most appropriate sample temperatures, are shown in Figure 24.

Figure 24. The conversion lifetimes in CH<sub>4</sub>

- neutron cross-section data - error bars express one standard deviation where more than one experiment was performed
- + thermal relaxation data
- n.m.r. ref. 60
- ▲ i.r. ref. 56
- theory ref. 64



The general shape of the temperature dependence is similar to that found for thermal relaxation in  $\text{CH}_4$ <sup>123</sup>. That similarity indicates that the thermal inertia observed in early calorimetric measurements can be associated with the conversion process, and not with a phase III-II transition as was first supposed<sup>67</sup>. The lifetimes derived from these thermal relaxation data are also shown in Figure 25, along with several estimates of  $\tau$  at  $T = 4.2$  K. The thermal measurements are the most precise, but it is satisfying that the general agreement is so good. The important result is not, however, the exact magnitude of  $\tau$ , but rather that several entirely different experiments exhibit the same trend and approximate magnitude.

There are at least two possible causes for the temperature dependence of the lifetimes on the disordered sublattices. In their theoretical calculation of the conversion rate, Nijman and Berlinsky<sup>64</sup> restricted the calculation to the lowest A and T energy levels for the disordered molecules. Their calculated rate would necessarily be temperature dependent because the increased population of the phonon states at higher temperatures would facilitate conversion. A broadening of the rotational energy levels at higher temperatures as was observed in the inelastic neutron study of Press and Kollmar<sup>47</sup>, would also lead to an enhancement of the conversion rate. It is also possible that, at higher temperatures, increased population of the excited rotational

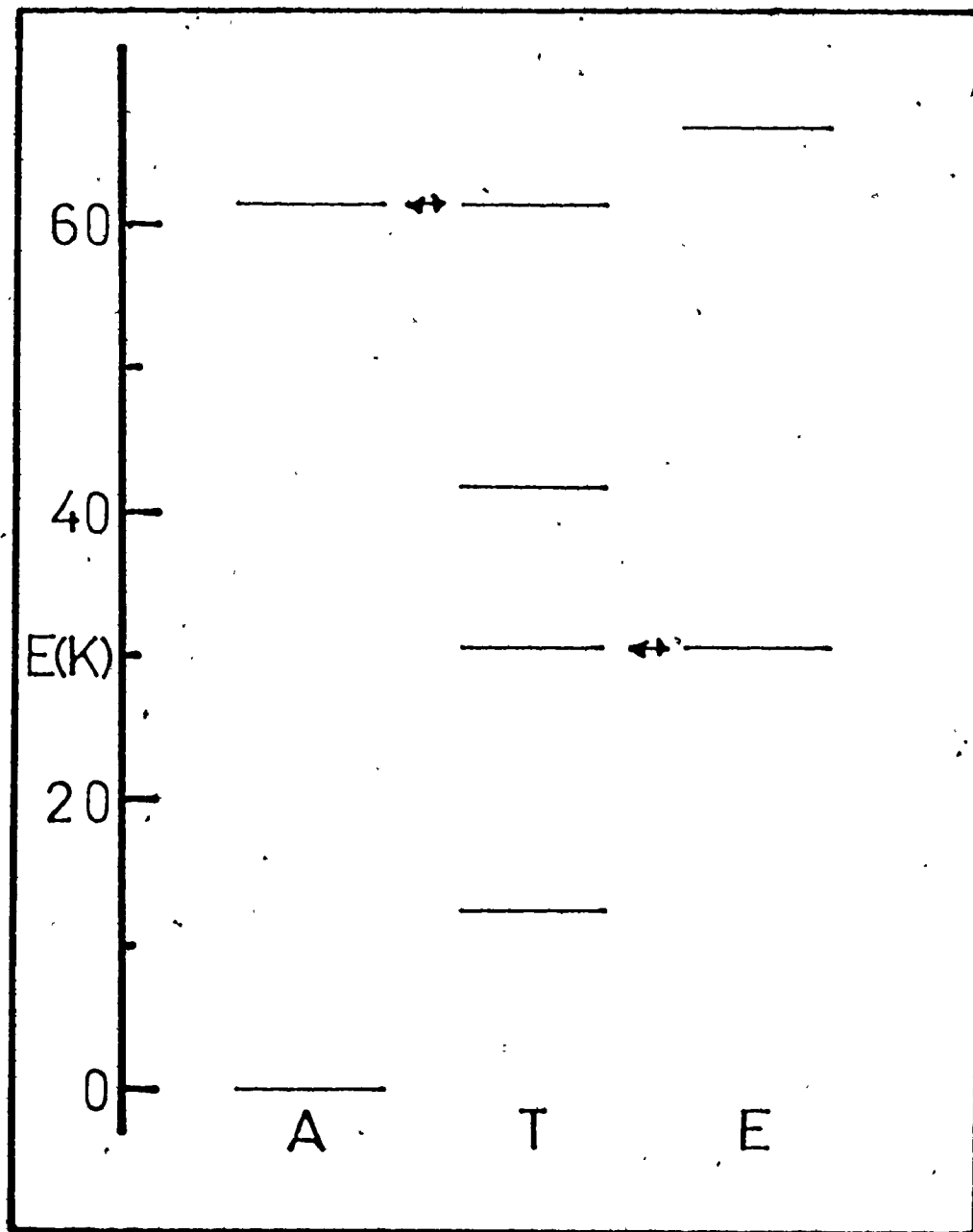


Figure 25. A truncated portion of the disordered sublattice energy level scheme for  $\text{CH}_4$

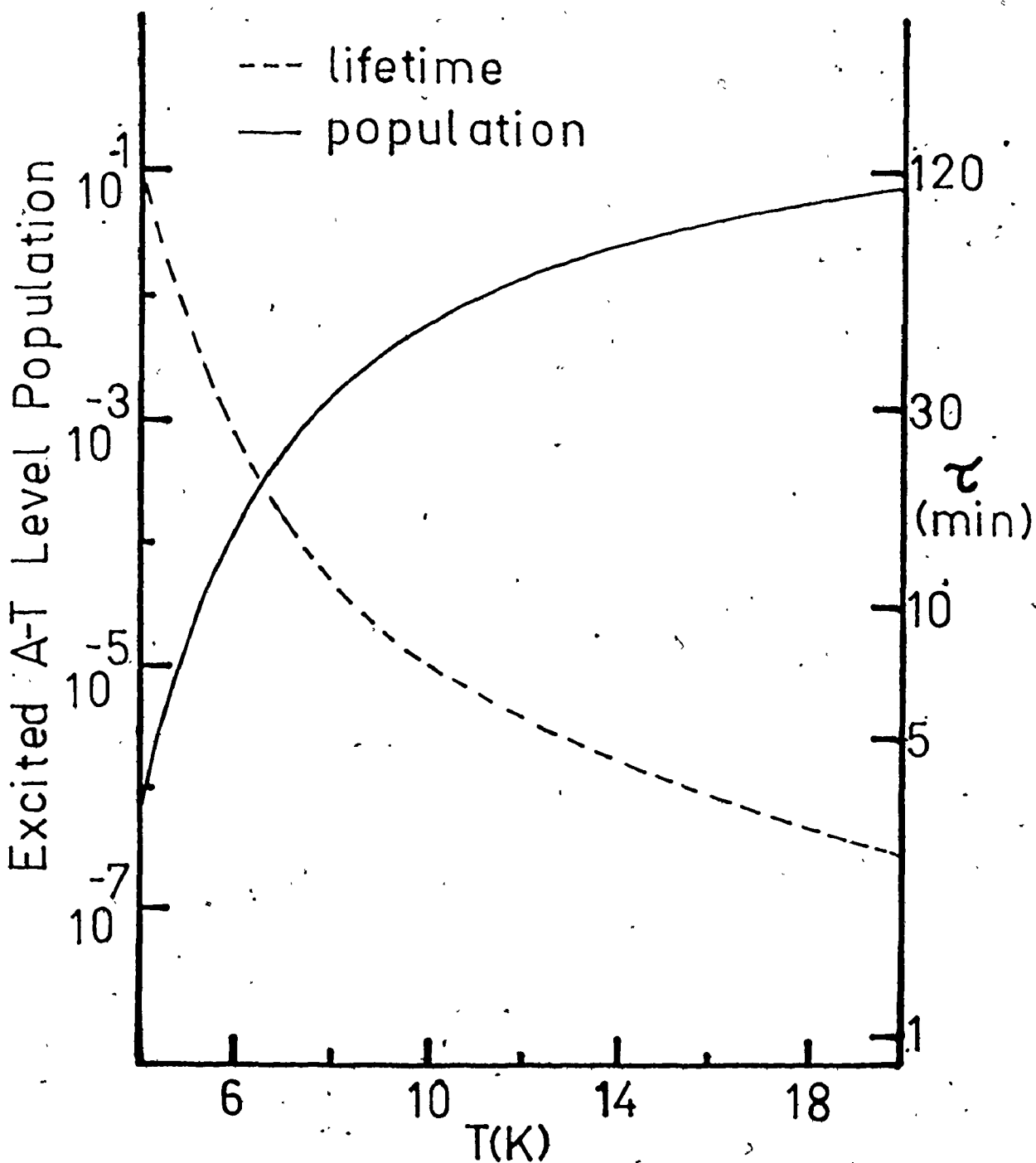


Figure 26. The population of the degenerate A-T level plotted with the conversion lifetimes in  $\text{CH}_4$

states provides an alternate pathway for conversion. If one of the excited levels should contain a degenerate A-T pair, conversion within the level would be rapid, and the overall rate would be enhanced. A truncated portion of the energy level array for the molecules is shown in Figure 25, where the three spin species have been separated for clarity. The lowest E level is degenerate with a T level, which would allow the E and T spin species to interconvert. The slow conversion process observed for the disordered molecules at low temperatures must, therefore, involve the T to A spin species conversion, as Nijman and Berlinsky assumed<sup>64</sup>. The first excited A level (60.5K) is, however, degenerate with one of the excited T levels, and the degeneracy, shown in Figure 25, could provide an alternate spin conversion pathway. If this is true, the observed conversion lifetimes should be inversely proportional to the population of these degenerate states at any temperature. The populations and the conversion lifetimes are shown, as a function of temperature, in Figure 26. The correlation between the two parameters is striking.

#### VI.4 CH<sub>3</sub>D

Much less information was available for CH<sub>3</sub>D than for CH<sub>4</sub>. While the existence of some spin conversion was surmised from an interpretation of thermal data<sup>52</sup>, and later established by n.m.r. experiments<sup>69</sup>, its full extent was unknown.

Moreover, CH<sub>3</sub>D transforms into phase III, a structure that

is not yet characterized. The consequence of that is a matter to be explored.

#### 4.1 The Cross-Section and Spin Conversion

Phase II of  $\text{CH}_3\text{D}$  is only stable over a narrow temperature range ( $16.1 \text{ K} < T < 23.1 \text{ K}$ ). Only a limited amount of cross-section data were obtained in this phase, but they showed a slight increase in  $\sigma$  as the temperature was decreased through the phase II region, - a trend that is consistent with spin conversion between the two possible spin species in  $\text{CH}_3\text{D}$  (A and E), probably on the disordered sublattices. At  $T = 16.1 \text{ K}$ , the phase transition to phase III occurs.

The cross-section data show that the transition is first order, and a slight hysteresis in the transition region was again observed. Annealing below the transition was found to be essential because, if the sample were cooled quickly from phase II,  $\sigma$  drifted with time for a period of hours. Similar behaviour had also been observed in the heat capacity<sup>53</sup> and n.m.r. studies<sup>69</sup> of  $\text{CH}_3\text{D}$ , but its origin was not established. The thermal measurements indicated that a significant amount of energy ( $9 \text{ J/mole}$ )<sup>53</sup> was released during these drifts of long duration, while both the n.m.r.<sup>69</sup> and the cross-section results showed that spin conversion was also involved. The effects were not, however, reproducible. It is possible that their origin is a domain type transformation, such as has been hypothesised to occur during the rapid transformation from phase I to II in  $\text{CH}_4$ , (section VI,



3.4). The long time effects would then be associated with the gradual growth of the phase III structure, and the spin conversion occurs as a consequence of the necessary changes in the rotational energy levels. The non-equilibrium nature of the phenomenon makes it difficult to study more quantitatively.

In phase III, the value of  $\sigma$  increases steadily as the temperature is decreased, which indicates that spin species conversion to the high nuclear spin ( $I = 3/2$ ) A species is occurring. The magnitude of the change is diminished in comparison to that for  $\text{CH}_4$  for two reasons. There are fewer protons, and the total cross-section is correspondingly reduced. In addition, the maximum expected change in  $\langle I(I+1) \rangle$  for complete spin conversion is much less than for  $\text{CH}_4$ , being only 1.5 compared to 3.0. It should also be noted that the bulk of the change in  $\sigma$ , and hence in  $\langle I(I+1) \rangle$ , occurs below  $T = 4$  K in  $\text{CH}_3\text{D}$ . This means that the lowest-lying energy levels in  $\text{CH}_3\text{D}$  must be considerably different from those in  $\text{CH}_4$ . Neither the structure nor the energy level scheme for phase III of  $\text{CH}_3\text{D}$  is known a priori, and to make some deductions about them may be taken to be one object of the neutron experiments. Even the qualitative analysis of the results has proven to be of great value because it has established, unambiguously, the temperature range over which spin conversion occurs, something that could not be done from thermal measurements.

The recent n.m.r. susceptibility measurements for  $\text{CH}_3\text{D}$ <sup>69</sup> indicate that  $\langle I(I+1) \rangle = 2.71 \pm 0.07$  at  $T = 1.8 \pm 0.3$  K. It would be valuable to confirm that but, before attempting it through a quantitative interpretation of the cross-section data, it is pertinent to examine the kinetics of conversion as well as the information to be gleaned from the thermodynamic data that are available.

#### 4.2 Kinetics of Spin Conversion

Throughout the experiments, no time dependence of  $\sigma$ , other than in the transition region, was observed. Moreover, oxygen doping was found to have no effect on the "equilibrium" value of  $\sigma$ , a behaviour in contrast to that of  $\text{CH}_4$ . The rate of conversion was always fast, but it was detectably different for the pure and oxygen-doped samples. For  $1.4 < T < 4.2$  K, the spin conversion lifetime of the oxygen-doped sample was approximately 30 seconds, an appreciable fraction of which could be due to thermal equilibration of the sample system. For the pure sample,  $\tau$  was about 130 seconds. Again, there turns out to be a parallel between neutron cross-section and calorimetric studies. In two separate thermal investigations of  $\text{CH}_3\text{D}$ <sup>52,70</sup>, the thermal relaxation lifetime, shown in Figure 27, was found to be unexpectedly long, and essentially independent of sample size and composition. The thermal data between  $T = 1.4$  K and 4.2 K yield a relaxation lifetime of about  $50 \pm 10$  seconds. Thus, the thermal

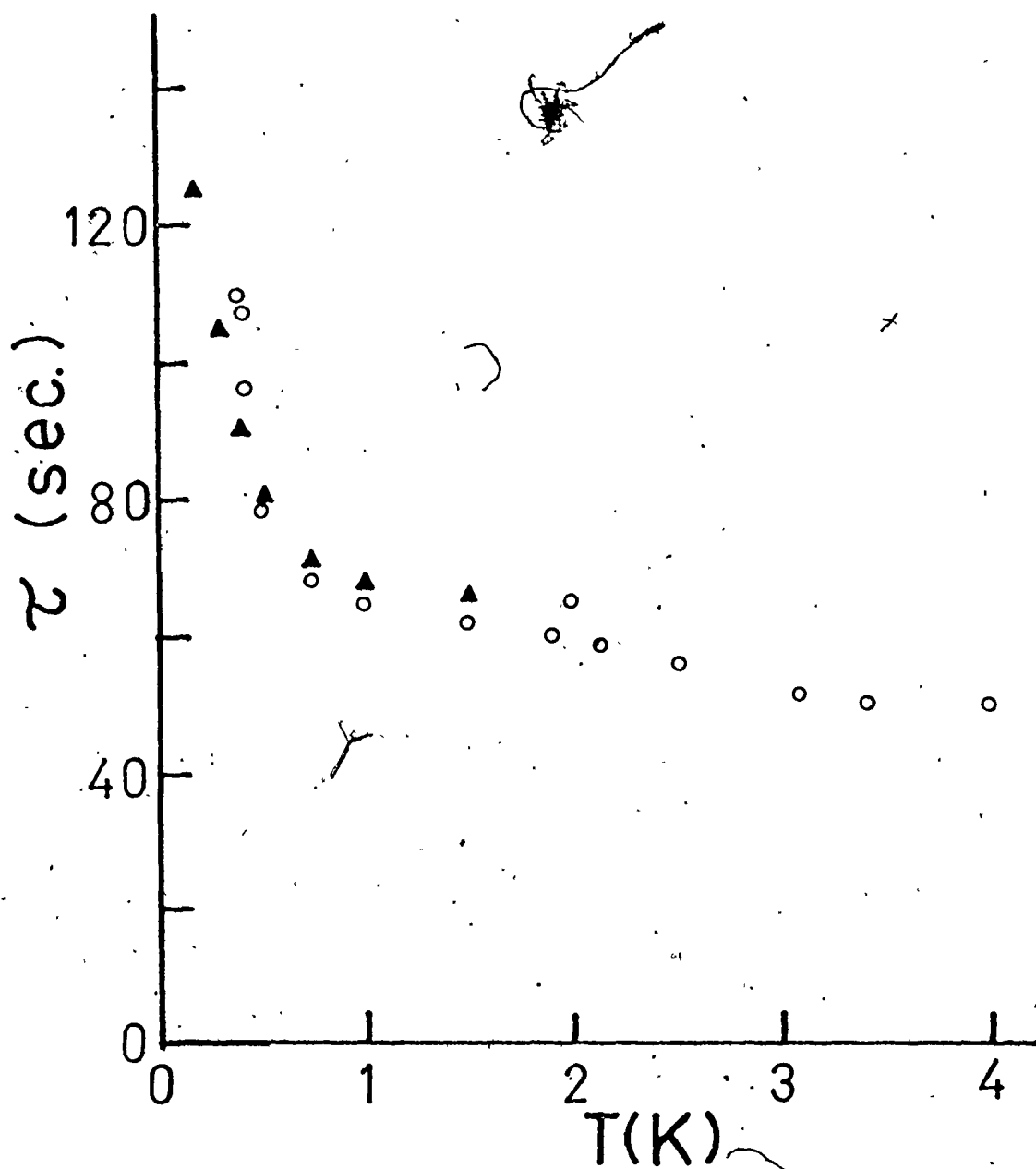


Figure 27. Thermal relaxation data for  $\text{CH}_3\text{D}$

○ ref. 52

▲ ref. 70

relaxation effects must be ascribed to spin conversion, as was first suggested by Colwell<sup>52</sup>. No obvious catalytic effects due to oxygen were evident in the thermal relaxation results, even though the two samples studied varied considerably in the level of oxygen impurity (10 ppm. and 0.24%). The apparent catalytic effect of oxygen observed in the cross-section results is possibly due to the much greater difference in oxygen impurity levels (1 ppm. and 1.2%). Below  $T = 0.8$  K, the thermal relaxation times become noticeably longer, which suggests that the spin conversion process is becoming more inhibited at the lower temperatures or that the mechanism is changing.

The interesting feature of conversion in  $\text{CH}_3\text{D}$  is that the molecules in phase III, presumably in an environment very similar to that of the ordered molecules in phase II of  $\text{CH}_4$ , convert at a rate about 2,000 times faster. The theory developed by Nijman and Berlinsky<sup>64</sup> for conversion in  $\text{CH}_4$  should apply equally well, in principle, to the  $\text{CH}_3\text{D}$  system and, on this basis, one would expect the conversion to be very slow in phase III. The fact that it is not suggests that at least two of the tunnelling levels, of different symmetry, are accidentally degenerate, thus removing the rate limiting step deduced from theory, - the emission of a phonon.

### 4.3 The Entropy of $\text{CH}_3\text{D}$

To elucidate a possible structure for the tunnelling levels in  $\text{CH}_3\text{D}$ , or a calibration procedure for the interrelation of  $\sigma$  to  $\langle I(I+1) \rangle$ , a model for the structure of phase III needs to be formulated. The results of such a procedure should be treated with caution, and only be taken as possible indications of the nature of solid  $\text{CH}_3\text{D}$  in phase III. The constraints on any model imposed by the existing data for  $\text{CH}_3\text{D}$  are, however, appreciable.

The entropy of  $\text{CH}_3\text{D}$  provides several unambiguous facts that are pertinent. The residual entropy at  $T = 0$  K, estimated in the usual way by comparing the statistical entropy (without nuclear spins) with the entropy based on calorimetric data, excluding the heat capacity anomaly in the region  $T < 8$  K, was found to be  $11.9 \pm 0.4$  J/mole K which, within the limit given, is  $R \ln 4^{92}$ . The natural explanation for that result is that the C-D bond direction of the  $\text{CH}_3\text{D}$  molecules remains randomly oriented with respect to the crystal axes at the low temperatures.

Since the Schottky-type anomaly is observed in the heat capacity at low temperatures, and since spin conversion is known to occur, it is preferable to include nuclear spins in the calculation of the statistical entropy (by adding  $R \ln \prod_i \rho_i$ , where  $\rho =$  the spin weight). When this is done, the residual entropy at  $T = 0$  K, on the basis just given, becomes  $38.3 \pm 0.4$  J/mole K which, within the limit shown is equal to  $R \ln 96$ .

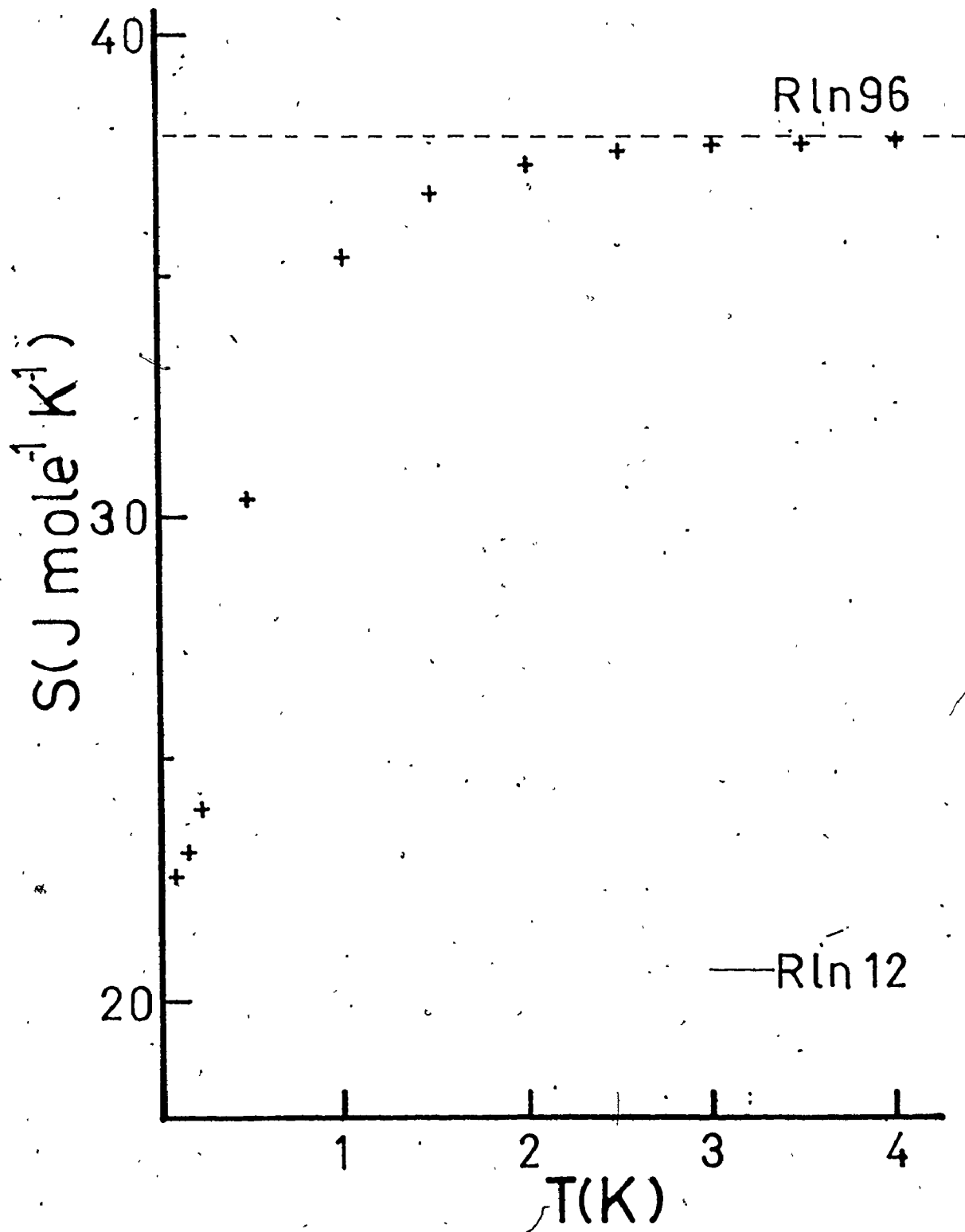


Figure 28. The entropy of  $\text{CH}_3\text{D}$  below  $T = 4$  K.

If account is then taken of the low temperature anomaly in the heat capacity to calculate the calorimetric entropy, using the most recent thermodynamic data<sup>53</sup>, the residual entropy at  $T = 0$  K becomes  $22.1 \pm 0.07$  J/mole K. (See Figure 28 for a representation of the temperature dependence of the entropy.) The lowest energy state of  $\text{CH}_3\text{D}$  has A symmetry and a nuclear spin degeneracy of 12 associated with it. The degeneracy could be expected to remain at the lowest experimental temperature reached,  $T = 0.15$  K. On this basis, the calculated minimum residual entropy would be  $R \ln 12$  (20.7 J/mole K) which is less than the value found experimentally by an amount that is twice the estimated uncertainty. A reduction in entropy from  $R \ln 96$  to  $R \ln 12$  is easily accounted for physically by spin conversion ( $R \ln 2$ ), and ordering of the orientations of the C - D bonds. The fact that the difference in residual entropies calculated from the data at higher and at lower temperatures is less than  $(R \ln 96 - R \ln 12)$  is possibly significant, but a unique interpretation cannot be offered.

#### 4.4 A Model for Phase III of $\text{CH}_3\text{D}$

The simplest premise on which to base the phase III structure is that all of the molecules become orientationally ordered, and equivalent to the ordered molecules of phase II. The resulting structure could still have many orientationally distinct sublattices, but the symmetry and the strength of

the potential at each lattice site would have to be essentially the same, - probably close to the tetragonal site symmetry which seems to describe adequately the ordered molecules in phase II of the  $\text{CH}_4$ . If such a model were correct, then the rotational energy levels of the molecules would be grouped into a low-lying set of tunnelling levels and a series of higher energy librational levels. Such a scheme could qualitatively explain the existence of the low temperature Schottky-type anomaly in the heat capacity, the behaviour of the entropy and the neutron cross-section results. While the model has these obvious advantages, it may not be an accurate representation of the phase III structure. Recent theoretical calculations<sup>124</sup> for the phase III structure have suggested that, while the disordered molecules of phase II become orientationally ordered in phase III, their symmetry is not equivalent to that of the ordered molecules in phase II. This is reasonable because the phase II+III transition would not be expected to produce a total reorganization of the lattice. At the present time, there are insufficient experimental results to allow a distinction to be made between the two models for phase III. The model with non-equivalent  $\text{CH}_3\text{D}$  molecules is the more complex, and the accuracy and quantity of existing data are not adequate to evaluate its parameters. Therefore, the simpler model with equivalent methane molecules will be used for the subsequent discussion of the neutron scattering results.



TABLE X

The Energy Level Scheme derived from the  
Equivalent Molecule Model.

---

Symmetry	Degeneracy	Energy (K)
E	12	2.6
E	4	1.4
A	12	1.1
A	4	0

---

For  $\text{CH}_3\text{D}$  molecules in a tetragonal crystal field, there will be four tunnelling levels, two of A symmetry and two of E. The degeneracies of the various levels are known from group theory<sup>125</sup>, and are given in Table X. The rotational partition function that corresponds to this model is simple because the higher energy librational excitations do not contribute significantly at low temperatures, and the heat capacity and  $\langle I(I+1) \rangle$  are, therefore, easily calculated. Actually, it is the reverse procedure that is appropriate, that is, to use the experimental results to obtain estimates of the energy level spacings. The heat capacity depends on both the degeneracies and the spacings, while the neutron cross-section data reflects the relative populations of the two spin species. Thus, the two sets of results are complementary.

A non-linear least squares method was used to derive estimates of the energy level spacings from the experimental heat capacities<sup>53</sup>. Spin conversion was assumed to occur readily, as the neutron cross-section results showed. It should be noted, however, that it was not possible to derive a set of energy levels that reproduced the heat capacities within their probable experimental error over the entire temperature range  $0.15 \text{ K} < T < 4. \text{ K}$ . The values of the energies given in Table X represent a compromise for both the high and low temperature regions.

The fact that a single set of levels was not consistent with the heat capacities suggests that the simple model chosen for phase III is inadequate. The same conclusion is reached from an analysis of the cross-section results. The values of  $\langle I(I+1) \rangle$ , corresponding to the energy levels in Table X were calculated and then used to determine the parameters in the linear relationship between  $\sigma$  and  $\langle I(I+1) \rangle$

$$\sigma = 140.9 + 3.89 \langle I(I+1) \rangle \quad [22]$$

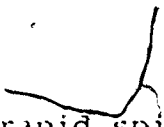
Equation [22] reproduced the experimental values of  $\sigma$ , except at  $T = 0.75 \text{ K}$  as is illustrated in Table XI.

The value of  $\langle I(I+1) \rangle$  calculated for  $T = 1.8 \text{ K}$  (2.83) agrees within the error limits, with that found from the n.m.r. determinations<sup>69</sup>. Moreover, it is satisfying that the array of levels in Table X places two levels of different spin symmetry in close proximity. This is consistent with

TABLE XI

Comparison between observed and calculated  
cross sections in CH<sub>3</sub>D

T(K)	$\sigma$ (barns)		$\langle I(I+1) \rangle$
	obs.	calc.	
0.75	155.3	154.0	3.37
1.4	152.6	152.4	2.97
1.6	152.2	152.2	2.91
1.8	151.8	151.9	2.83
2.0	151.6	151.7	2.78
2.5	151.3	151.3	2.68
3.0	151.0	151.0	2.61
3.5	150.9	150.9	2.56
4.0	150.7	150.7	2.56
4.5	150.6	150.6	2.49
5.0	150.5	150.5	2.70
6.0	150.3	150.3	2.43
10.0	150.1	150.1	2.36



the rapid spin species conversion that is observed experimentally.

To summarize: the simple model for phase III serves to correlate the results of different kinds of experiments on  $\text{CH}_3\text{D}$ . While the general agreement is satisfactory, there are obvious indications that the actual situation is more complicated than that envisaged by the model. There appears to be a distinct change in the behaviour of the system between  $T = 0.7$  K and 1.4 K, the region where the temperature dependence of the thermal relaxation times change (Figure 27). This suggests two possible modifications of the model.

The first is that the molecules are not all on equivalent sites; the simplest alternative being the recently proposed structure where one-quarter of the molecules are still in a less hindering potential than the remaining three-quarters. On this basis, there would be two different contributions to the heat capacity, the thermal relaxation and the neutron cross-sections. Qualitatively, the deviations from the simple model are consistent with a two sub-lattice model, but that is as far as the matter can be taken at present. A second possible explanation for the breakdown of the simple model is that the energy level spacings are temperature dependent, as has been found theoretically for  $\text{CH}_4$ <sup>16</sup>. Dilation of the levels would cause  $\langle I(I+1) \rangle$  to be larger than expected at low temperatures. Similarly, the calculated heat capacity would be affected, as well as the

conversion lifetime. The thermal relaxation time could be drastically altered if the level dilation were to remove the accidental degeneracy between the two levels through which spin conversion is accelerated.

#### VI.5 $\text{CH}_2\text{D}_2$

The total cross-section results for  $\text{CH}_2\text{D}_2$  were obtained to ascertain if spin conversion was occurring, especially in the region of the low temperature Schottky-type anomaly ( $T < 1.5$  K) which had been observed in the heat capacity<sup>52</sup>. The results show a small but significant decrease in  $\sigma$  below  $T = 4.2$  K (shown in Figure 21). Its cause is not immediately obvious, but it will be argued that it could result from spin conversion. A decrease in  $\sigma$  could be caused by two effects: a change in the inelastic scattering as the tunnelling levels depopulate at lower temperatures, or spin conversion. A group theoretical analysis of  $\text{CH}_2\text{D}_2$  in a tetragonal field<sup>5</sup>, the most probable symmetry for the phase III structure, indicate that five tunnelling levels occur with two possible spin species (A and B). Of the five levels, three have symmetry  $A(I_H = 12/7)$  and two,  $B(I_H = 6/5)$ . It is possible to construct an acceptable arrangement of these levels that leads to a decrease in  $\langle I(I+1) \rangle$  below  $T = 4.2$  K. Such a configuration is shown in Figure 29, along with the temperature dependence of  $\langle I(I+1) \rangle$  for such a scheme. The level scheme chosen is very similar to one proposed by Colwell<sup>52</sup> to fit the low

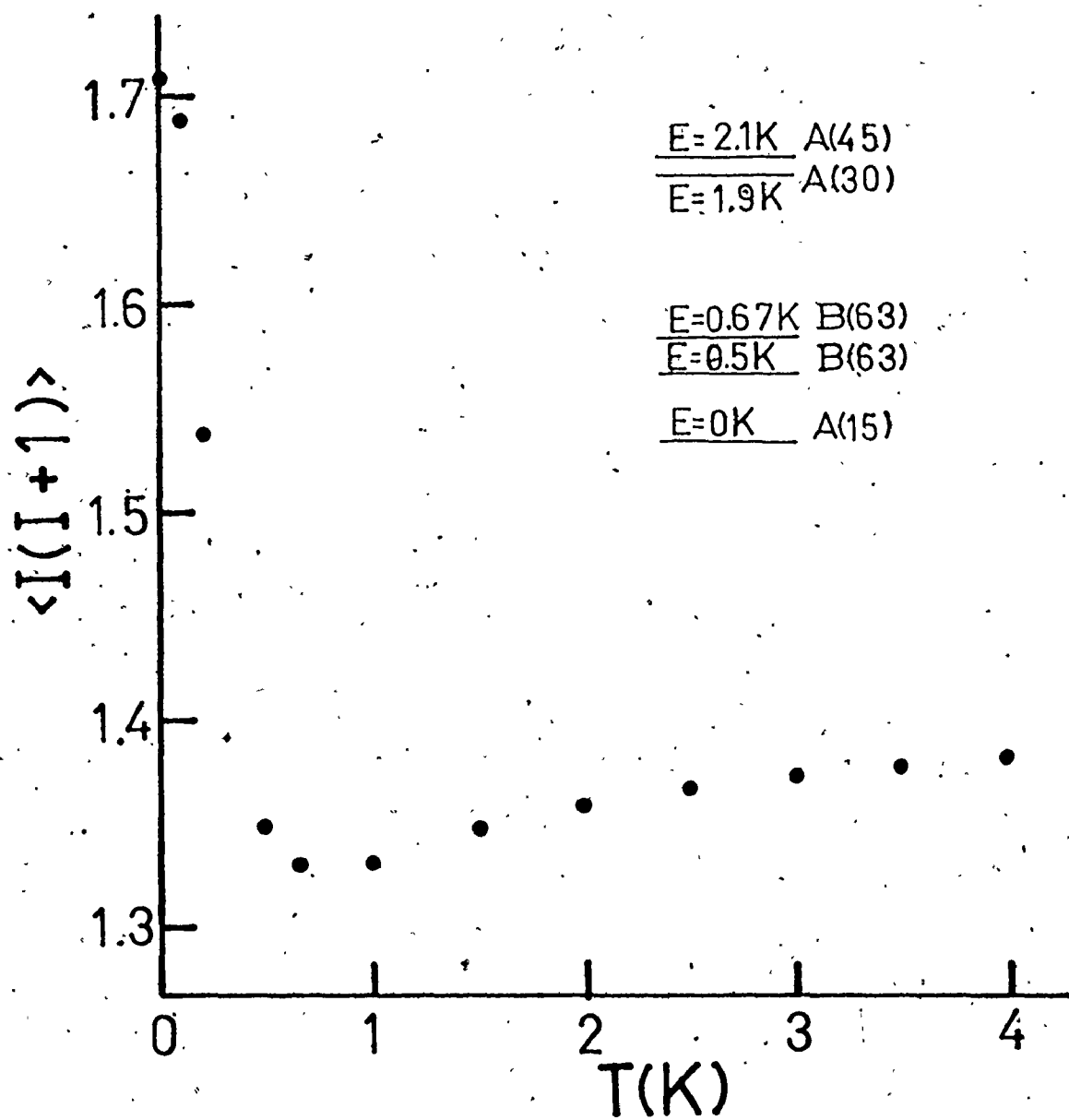


Figure 29. An hypothetical energy level scheme and the corresponding values of  $\langle I(I+1) \rangle$  for  $\text{CH}_2\text{D}_2$

temperature heat capacity data of  $\text{CH}_2\text{D}_2$ , except that the order of the levels has been changed slightly. The calculated values of  $\langle I(I+1) \rangle$  show a small decrease from  $T = 4.2$  K down to 0.75 K, below which a large increase in  $\langle I(I+1) \rangle$  occurs. The energy level scheme chosen qualitatively explains the observed neutron cross-section results and so the model ought to be considered when further data on  $\text{CH}_2\text{D}_2$  become available.

Little can be said about the rate of spin conversion in  $\text{CH}_2\text{D}_2$  other than that the lifetime of the process was probably less than the counting interval (3 minutes). It should be noted, however, that the experimental sample of  $\text{CH}_2\text{D}_2$  contained an appreciable amount of oxygen ( $\sim 500$  ppm.)

n

## CHAPTER VII

### CONCLUSIONS

The use of total neutron cross-sections as a measure of the composition of nuclear spin symmetry species in a molecular solid has been developed and refined to the point where it yields quantitative information about the spin conversion process. At higher temperatures, where changes in the concentrations of spin species are small, the total cross-section is sensitive to subtle changes in molecular rotation and translation. That aspect is not treated extensively in this thesis.

The principal experiments were performed on the solid isotopic methanes  $\text{CH}_4$ ,  $\text{CH}_3\text{D}$  and  $\text{CH}_2\text{D}_2$ . For  $\text{CH}_4$ , the results of the cross-section measurements confirm deductions from n.m.r. studies which had indicated that spin conversion proceeds differently on the ordered and disordered sublattices of phase II. The equilibrium values of the cross-section obtained with oxygen-doped sample of  $\text{CH}_4$ , have been used to test the predicted theoretical temperature dependence of  $\langle I(I+1) \rangle$ , the mean squared proton nuclear angular momentum per molecule. Quantitative agreement is found. The kinetics of the spin conversion process was studied in both pure and oxygen-doped  $\text{CH}_4$  samples. Conversion on the ordered sub-



lattices was found to be very slow, although not as slow as predicted by theory. The difference may be accounted for by the presence of trace amounts of oxygen in the experimental sample. Conversion on the disordered sublattices was found to be much faster, and strongly temperature dependent. The conversion lifetimes are consistent with those observed for thermal relaxation in  $\text{CH}_4$ .

Spin conversion is shown to occur in  $\text{CH}_3\text{D}$  in the region  $T < 4$  K, and to be close to completion by  $T = 0.75$  K. This result is correlated with changes in the entropy of  $\text{CH}_3\text{D}$  at low temperatures. There is, however, the complication that ordering of the C-D bond directions occurs over the same temperature region. Since the structure of the low temperature equilibrium solid phase (phase III) is not known, a full interpretation of the experimental results is not possible, but estimates of the low lying energy levels of  $\text{CH}_3\text{D}$  can be made. The rapid spin conversion that is observed is attributed to an accidental degeneracy of levels of the A and E spin symmetry species. No firm conclusion can be drawn about the possible dilation of the low lying energy levels as the spin conversion process occurs.

A less extensive study was made of  $\text{CH}_2\text{D}_2$  because relatively few results are available for that methane from other kinds of experiments. Moreover, the neutron cross-section measurements were necessarily less sensitive because of the low proton concentration in the molecule. In contrast

to the observations made with  $\text{CH}_4$  and  $\text{CH}_3\text{D}$  the total neutron cross-section was found to decrease with decreasing temperature in the region  $T < 4$  K. An argument is developed to show that this result can be consistent with spin conversion.

## APPENDIX 1

### Calculation of Neutron Cross-sections - The Krieger-Nelkin Method

There are many methods which have been used to calculate the neutron cross-sections of free molecules<sup>186</sup>, but the Krieger-Nelkin method<sup>84</sup> is, perhaps, the most straightforward. The method is based on the more sophisticated, and very difficult to use, Zemach and Glauber<sup>82</sup> formalism which accounts for the quantum mechanical nature of the scatterer. The Krieger-Nelkin method is a quasi-classical approach in that restrictions are placed on the theory in such a way that the quantum nature of the rotations is neglected. The energy of the neutron,  $E_0$ , must be larger than the rotational energy level spacing, and the temperature of the sample,  $T$ , must be high enough to populate many rotational levels. Within this range of applicability, the rotational and translational motion of the molecules are incorporated into an effective mass,  $\bar{m}$ , derived from the Sachs-Teller mass tensor concept<sup>85</sup>. The Krieger-Nelkin calculation thus cannot deal with the problems arising from nuclear spin correlations, or those from the quantum nature of the rotations, but it does provide a good indication of how the cross-section for methane behaves, as a function of tempera-

ture, in the gas and liquid phases<sup>86,87</sup>.

The cross-section per nucleus,  $\sigma_N$ , for each nucleus in the molecule, is given by the following expression

$$\sigma_N = \sigma_N^F \frac{2\bar{\omega}}{E_0} \left\{ \operatorname{erf}(C^{1/2}) - (1-p)^{1/2} e^{-Cp} \operatorname{erf}(C^{1/2}(1-p^{1/2})^{1/2}) \right\}$$

[A1.1]

where:

$\sigma_N^F$  is the free nucleus cross-section.

$\bar{\omega}$  is the energy (in eV) of the lowest internal mode of vibration.

$$C = \frac{E_0 \bar{m}}{kT}$$

$$p = (1 - \alpha^2/\beta)^{-1}$$

$$\alpha = (1 + \bar{m})/kT$$

$$\beta = \bar{m}/(2\bar{\omega}kT)$$

Equation [A1.1] can be evaluated for each different nucleus in the molecule, where the effects of chemical binding are encompassed in  $\bar{m}$ , and the results summed to obtain the total cross-section of the molecule. A comprehensive analysis of the Krieger-Nelkin method has been given by McMurray et al.<sup>127</sup>.

A list of the two parameters, which contain the molecular information, is given below for the isotopic methanes studied. The values of  $\bar{\omega}$  were obtained for spectroscopic data<sup>128</sup>. With these values for the methanes

TABLE A1.I

Isotope	$\bar{m}$	$\bar{\omega}$ (eV)
CH <sub>4</sub>	0.2944	0.1656
CH <sub>3</sub> D	0.2621 (protons) 0.2403 (deuteron)	0.1433
CH <sub>2</sub> D <sub>2</sub>	0.2145 (protons) 0.2353 (deuteron)	0.1282

and for  $T = 95$  K and a neutron wavelength of  $4.72 \text{ \AA}$ , the total cross-section and the slope of the cross-section per proton with temperature (the Krieger-Nelkin formula gives a linear dependence with temperature) were calculated with the following results.

TABLE A1.II

Methane	$\sigma$ (T=95 K) (barns)	slope (barns K <sup>-1</sup> proton <sup>-1</sup> )
CH <sub>4</sub>	253.8	.147
CH <sub>3</sub> D	206.2	.144
CH <sub>2</sub> D <sub>2</sub>	157.8	.141

Increased deuteration of the methane molecule does not drastically affect the slope of the cross-section-temperature line.

## APPENDIX 2

### The Long Wavelength Limit for the Neutron Cross-section

The correspondence between the total neutron cross-section and  $\langle I(I+1) \rangle$  is most clearly evident if one examines the elastic scattering of very long wavelength neutrons. The long wavelength expansion for  $\text{CH}_4$  has been performed by Johnston<sup>129</sup> and so only an outline is given here.

The starting point is the rigorous expression for the elastic total cross-section,

$$\sigma = 4\pi \sum_i g_i \langle i | \sum_{\text{atoms}=1}^5 \hat{b}_N e^{i\vec{Q}\cdot\vec{r}} | i \rangle \rangle^2 \quad [\text{A2.1}]$$

where  $g_i$  is the population factor for the  $i^{\text{th}}$  state and  $\hat{b}_N$  is the spin dependent scattering length of the  $N^{\text{th}}$  atom in the molecule.

If the neutron wavelength is very long such that  $\vec{Q}\cdot\vec{r} \ll 1$ , the exponential can be expanded and only the first term retained. Equation [A2.1] then becomes just the square of the expectation value of the scattering length:

$$\sigma = 4\pi \sum_i g_i \langle i | \sum_{\text{atoms}} \hat{b}_N | i \rangle \rangle^2 \quad [\text{A2.2}]$$

The spin dependent form of the scattering length is given

in many texts<sup>80,76</sup> and is,

$$b_N = \frac{(I_N + 1 + 2(\vec{I}_N \cdot \vec{s}))}{2I_N + 1} b_+ + \frac{(I_N - 2(\vec{I}_N \cdot \vec{s}))}{2I_N + 1} b_- \quad [A2.3]$$

When equation [A2.3] is substituted into [A2.2], there are several terms which can be more easily condensed if two additional quantities are defined: the coherent scattering length

$$b_{\text{coh}} = \frac{I+1}{2I+1} b_+ + \frac{I}{2I+1} b_- \quad [A2.4]$$

and the incoherent scattering length

$$b_{\text{inc}} = \frac{[I(I+1)]^{1/2}}{2I+1} (b_+ - b_-) \quad [A2.5]$$

where  $I$  is the nuclear spin of the scatterer. In the expansion of [A2.2], there are several spin dependent terms of the form  $\langle (\vec{s} \cdot \vec{I}_N) \rangle$  which must be zero if the neutron beam is unpolarised. Other terms of the form  $\langle (\vec{s} \cdot \vec{I}_i) (\vec{s} \cdot \vec{I}_j) \rangle$  can be combined and shown to be proportional to  $\langle I(I+1) \rangle$  for the molecule, which is the desired result. The final expression for the total cross section of  $\text{CH}_4$  is

$$\sigma = 4\pi \sum_{\substack{I=\text{spin} \\ \text{species}}} g_I [16 b_{\text{coh}}^2 + \frac{1}{4} (b_{\text{H}^+} - b_{\text{H}^-})^2 I(I+1) + 8 b_{\text{coh}} b_{\text{carbon}} + b_{\text{carbon}}^2] \quad [A2.6]$$

With this expression, the total cross-section for  $\text{CH}_4$  at high temperatures,  $\langle I(I+1) \rangle = 3.00$ , is 290 barns, while the cross-section for a molecule in the ground A state is 537 barns.



## BIBLIOGRAPHY

1. J. Van Kranendonk and G. Karl, Rev.Mod. Phys. 40, 531 (1968).
2. A. F. Schuch, R. L. Mills and D. A. Depatie, Phys. Rev. 165, 1032 (1968).
3. K. Motizuki and T. Nagamiya, J. Phys. Soc. Jap. 11, 93 (1956).
4. D. A. Depatie and R.L. Mills, Rev. Sci. Instr. 39, 105 (1967):
5. M. Bloom and J. A. Morrison, in Surface and Defect Properties of Solids, Specialist Periodical Reports of the Chemical Society, vol. 2, 140 (1973).
6. A. B. Harris, J. Appl. Phys. 42, 1574 (1971):
7. I. F. Silvera, W. N. Hardy and J. P. McTague, Discussions of the Faraday Society No. 48, 54 (1969).
8. M. J. Clouter, H. P. Gush and H. L. Welsh, Can. J. Phys. 48, 237 (1970).
9. W. N. Hardy, I. F. Silvera and J. P. McTague, Phys. Rev. B12, 753 (1975).
10. J. C. Raich and R. D. Ethers, Phys. Rev. 168, 425 (1968).
11. F. G. Mertens, W. Biem and H. Hahn, Zeit. Phys. 213, 33 (1968).

12. C. F. Coll III and A. B. Harris, Can. J. Phys. 55, 1180 (1977).
13. C. C. Sung, Phys. Rev. 167, 271 (1968).
14. W. N. Hardy, A. J. Berlinsky and A. B. Harris, Can. J. Phys. 55, 1150 (1977).
15. A. B. Harris, A. J. Berlinsky and W. N. Hardy, Can. J. Phys. 55, 1180 (1977).
16. T. Yamamoto, Y. Kataoka and K. Okada, J. Chem. Phys. 66, 2701 (1977).
17. R. F. Code and J. Higinbotham, Can. J. Phys. 54, 1248 (1976).
18. K. J. Lushington and J. A. Morrison, Can. J. Phys. 55, 1580 (1977).
19. K. Clusius, Zeit. Phys. Chem. 3, 41 (1929).
20. W. F. Giaugue, R. W. Blue and R. Overstreet, Phys. Rev. 38, 196 (1931).
21. A. Frank and K. Clusius, Zeit. Phys. Chem. B36, 291 (1937).
22. K. Clusius, L. Popp and A. Frank, Physica, 4, 1105 (1937).
23. E. Bartholomé, G. Drikos and A. Eucken, Zeit. Phys. Chem. B39, 371 (1938).
24. O. Trapeznikowa and G. Milgutin, Nature, 144, 632 (1939).
25. N. Stevenson, J. Chem. Phys. 27, 656 (1957).
26. J. W. Stewart, J. Phys. Chem. Solids, 12, 122 (1959).
27. L. Nijman, Ph.D. Thesis, University of Amsterdam, Amsterdam (1977).
28. A. Schallamach, Proc. Roy. Soc. A171, 509 (1939).

29. S. G. Greer and L. Meyer, *Zeit. Angew. Phys.* 27, 198 (1971).
30. S. C. Greer, L. Meyer and C. S. Barrett, *J. Chem. Phys.* 50, 4299 (1969).
31. J. Herczeg and R. E. Stoner, *J. Chem. Phys.* 54, 2284 (1971).
32. D. R. Aadsen, Ph.D. Thesis, University of Illinois, Urbana, IL (1975).
33. D. N. Bol'shutkin, V. M. Gasan, A. I. Prokhvatilov and A. I. Erenbarg, *J. Struct. Chem.* 12, 313 (1971).
34. W. Press, *J. Chem. Phys.* 56, 2597 (1972).
35. W. Press and A. Hüller, in T. Riste ed., Anharmonic Lattices, Structural Transitions and Melting, Noordhoof, Leiden (1974) pp. 185-212.
36. J. O. Hirschfelder, C. F. Curtiss and R. B. Bird, Molecular Theory of Gases and Liquids, John Wiley and Sons, Inc., New York (1954).
37. J. N. Murrell, in N. H. March, ed., Orbital Theories of Molecules and Solids, Clarendon Press, Oxford (1974).
38. M. L. Klein and J. A. Venables, Rare Gas Solids, Academic Press, London (1976).
39. H. M. James and T. A. Keenan, *J. Chem. Phys.* 31, 12 (1959).
40. E. A. Ballik, D. J. Gannon, and J. A. Morrison, *J. Chem. Phys.* 58, 5639 (1973).
41. H. Yasuda, *Prog. Theor. Phys.* 45, 1361 (1971).
42. H. Kapulla and W. Gläser, *Phys. Lett.* A31, 158 (1970).

43. B. Dorner and H. Stiller, Proceedings of Symposium on Neutron Inelastic Scattering, IAEA, Bombay (1965), vol. 2, p.291.
44. Y. D. Harker and R. M. Brugger, J. Chem. Phys. 46, 2201 (1967).
45. Y. Kataoka, K. Okada and T. Yamamoto, Chem. Phys. Lett. 19, 365 (1973).
46. H. Glättli and A. Sentz, Phys. Rev. Lett. 28, 871 (1972).
47. W. Press and A. Kollmar, Solid State Commun. 17, 405 (1975).
48. J. H. Colwell, E. K. Gill and J. A. Morrison, J. Chem. Phys. 39, 635 (1963).
49. G. J. Vogt and K. S. Pitzer, J. Chem. Thermodyn. 8, 1011 (1976).
50. D. C. Heberlein and E. D. Adams, J. Low Temp. Phys. 3, 115 (1970).
51. A. N. Aleksandrouskii, V. I. Kuchnev, V. G. Manzhelii and A. M. Tokachev, Phys. Stat. Solidi, B73, K111 (1976).
52. J. H. Colwell, J. Chem. Phys. 51, 3820 (1969).
53. J. A. Morrison, E. P. Jones and E. L. Richards, Can. J. Phys. 53, 2546 (1975).
54. E. B. Wilson, Jr., J. Chem. Phys. 3, 276 (1935).
55. R. F. Curl, Jr., J. V. V. Kasper and K. S. Pitzer, J. Chem. Phys. 46, 3220 (1967).
56. F. H. Frayer and G. E. Ewing, J. Chem. Phys. 48, 781 (1968).

57. K. P. Wong, J. D. Noble, M. Bloom and S. Alexander, J. Magn. Res. 1, 55 (1969).
58. R. P. Wolf and W. M. Whitney, Proceedings of the Ninth Low Temperature Conference, Plenum Press, New York. (1965) p. 1118.
59. H. P. Hopkins, P. L. Donoho and K. S. Pitzer, J. Chem. Phys. 47, 864 (1967).
60. L. Van Greven and P. van Hecke, Proceedings of the First Specialized "Colloque Ampere", Institute of Nuclear Physics, Krakow (1973) vol. 1, p.244.
61. O. Runolfsson, S. Mango and M. Borghini, Physica, 44, 494 (1969).
62. J. E. Piott and W. D. McCormick, Can. J. Phys. 54, 1784 (1976).
63. N. T. Johnston and M. F. Collins, J. Chem. Phys. 57, 5007 (1972).
64. A. J. Nijman and A. J. Berlinsky, Phys. Rev. Lett. 38, 408 (1977).
65. J. J. Kim and K. S. Pitzer, J. Chem. Phys. 66, 2400 (1977).
66. R. F. Code, Private Communication.
67. J. H. Colwell, E. K. Gill and J. A. Morrison, J. Chem. Phys. 36, 2223 (1962).
68. E. A. Ballik, D. J. Gannon and J. A. Morrison, J. Chem. Phys. 57, 1793 (1972).
69. R. F. Code, J. Higinbotham and B. M. Wood, Phys. Rev. B 14, 4773 (1976).

70. J. A. Morrison, K. J. Lushington, E. L. Richards. To be published.
71. R. F. Code and J. D. Noble, *J. Chem. Phys.* 57, 2160 (1972).
72. W. L. Whitlemore, *Nucl. Sci. Eng.* 18, 182 (1964).
73. G. L. Squires and A. T. Stewart, *Proc. R. Soc. London Ser. A230*, 19 (1953).
74. L. B. Borst, S. L. Borst, L. Koysooko, H. Patel and E. Stusnick, *Phys. Rev. Lett.* 7, 343 (1961).
75. L. B. Borst, Fundamental Liquids, Twin Bridge Press, Williamsville, New York (1970).
76. D. E. Parks, M. S. Nelkin, J. R. Beyster and N. F. Wikner, Slow Neutron Scattering and Thermalisation, W. A. Benjamin, Inc., New York (1970) pp. 1-40.
77. B. N. Brockhouse, S. Hautecler and H. Stiller, in R. Strunone, J. Nihoul, R. Gevers and S. Amelinckx, ed., The Interaction of Radiation with Solids, North Holland, Amsterdam (1964) p.580.
78. G. E. Bacon, Neutron Scattering in Chemistry, Butterworths, London (1977).
79. B. T. M. Willis, ed., Chemical Applications of Thermal Scattering, Oxford University Press, London (1973) p.296.
80. I. I. Gurevich and L. V. Tarasov, Low Energy Neutron Physics, American Elsevier, New York, NY (1968).
81. C. G. Windsor, in B. T. M. Willis, ed. Chemical Applications, p.1.

82. A. C. Zemach and R. J. Glauber, Phys. Rev. 101, 118 (1956).
83. Ibid, p. 129.
84. T. J. Krieger and M. S. Nelkin, Phys. Rev. 106, 290 (1957).
85. R. G. Sachs and E. Teller, Phys. Rev. 60, 18 (1940).
86. J. J. Rush, G. J. Safford, T. I. Taylor and W. W. Havens, Jr., Nucl. Sci. Eng. 14, 339 (1962).
87. Z. Rogalaska, Acta Phys. Polonica 27, 581 (1965).
88. P. Michael, Phys. Rev. 138A, 692 (1965).
89. S. K. Sinha and G. Venkataraman, Phys. Rev. 149, 1 (1966).
90. J. Hama and H. Miyagi, Prog. Theor. Phys. 50, 1142 (1973).
91. P. R. Norton, J. Chromat. Sci. 8, 411 (1970).
92. J. H. Colwell, E. K. Gill and J.A. Morrison, J. Chem. Phys. 42, 3144 (1965).
93. H. S. Sandhu, J. Chem. Phys. 44, 2320 (1966).
94. H. S. Sandhu, J. Lees and M. Bloom, Can. J. Chem. 38, 493 (1966).
95. S. Dushman, Scientific Foundations of Vacuum Technique, John Wiley and Sons, New York (1962) pp.80-111.
96. V. P. Peshkov and A. Y. Parshin, Proceedings of the Ninth Low Temperature Conf. Plenum Press, New York (1965) p.517.
97. W. G. Black, Jr., W. R. Roach and J. C. Wheatley, Rev. Sci. Instr. 35, 587 (1964).
98. R. Fletcher, J. Phys. E. 4, 470 (1971).
99. B. N. Brockhouse, G. A. deWitt, E. D. Hollman and J. M. Rowe, Proceedings of the Symposium on Neutron

- Inelastic Scattering, V.2, IAEA, Vienna (1968) p.259.
100. P. K. Iyengar, in P. A. Egelstaff, ed., Thermal Neutron Scattering, Academic Press, New York (1965) pp. 129-130.
  101. V. G. Manzhelii and A. M. Tol'kachev, Sov. Phys. Solid State 5, 2506 (1964).
  102. V. G. Manzhelii and A. M. Tol'kachev, Sov. Phys. Solid State 7, 1711 (1966).
  103. V. M. Cheng, W. B. Daniels and R. K. Crawford, Phys. Rev. B 11, 3972 (1975).
  104. M. J. Terry, J. T. Lynch, M. Bunclark, K. R. Mansell and L.A.K. Staveley, J. Chem. Thermodynamics 1, 413 (1969).
  105. R. Prydz and R. D. Goodwin, J. Chem. Thermodynamics 4, 127 (1972).
  106. R. O. Simmons, Private Communication.
  107. D. N. Bol'shutkin, V. M. Gason, A. I. Prokhvatilov and L. D. Yantsevich, J. Struct. Chem. 12, 1036 (1971).
  108. S. C. Greer and L. Meyer, J. Chem. Phys. 52, 468 (1970).
  109. S. Fuks, J. C. Legros and A. Bellemans, Physica 31, 606 (1965).
  110. A. F. Grigor and W. A. Steele, J. Chem. Phys. 48, 1032 (1968).
  111. G. Thomaes and R. van Steenwinkel, Mol. Phys. 5, 307 (1962).
  112. A. F. Grigor and W. A. Steele, J. Chem. Phys. 48, 1038 (1968).
  113. K. Clusius, Zeit. Phys. Chem. B46, 1 (1940).



114. J. Wilks; The Properties of Liquid and Solid Helium, Clarendon Press, Oxford (1967) p.666.
115. P. R. Bevington, Data Reduction and Error Analysis for the Physical Sciences, McGraw-Hill, New York (1969) pp.204-242.
116. S. C. Greer, Phys. Lett. 43A, 73 (1973).
117. Y. D. Harker and R. M. Brugger, J. Chem. Phys. 42, 275 (1964).
118. L. Q. Amaral, R. Fulfara and L. A. Vinhas, J. Chem. Phys. 63, 1312 (1975).
119. V. Tarina, Proceedings Symposium on Neutron Inelastic Scattering, V.2, IAEA, Vienna (1968) p.501.
120. T. Nakamura and H. Miyagi, J. Chem. Phys. 54, 5276 (1964).
121. M. Bloom and G. A. deWit, Can. J. Phys. 47, 1195 (1969).
122. L. Nijman, Private Communication.
123. J. H. Colwell, E. K. Gill and J. A. Morrison, Private Communication.
124. A. Hüller, Private Communication.
125. T. Nagamiya, Prog. Theor. Phys. 6, 702 (1951).
126. J. A. Janik and A. Kowalska, in P. A. Egelstaff, ed. Thermal Neutron Scattering, Academic Press, New York (1965) pp.142-192.
127. H. L. McMurray, L. J. Gannon and W. A. Hestir, Nucl. Sci. Eng. 15, 438 (1963).
128. G. Herzberg, Molecular Spectra and Molecular Structure, Vol. II, Van Nostrand, Princeton (1945) p.309.

129. N. T. Johnston, M.Sc. Thesis, McMaster University (1972).